Clustering Phenomena from Two-particle Angular Correlations in Proton-Proton and Heavy Ion Collisions

by

Wei Li

B.S., University of Science and Technology of China (2004)

Submitted to the Department of Physics
in partial fulfillment of the requirements for the degree of

Doctor of Philosophy

at the

MASSACHUSETTS INSTITUTE OF TECHNOLOGY

January 2009

Author ....
Department of Physics
January 30th, 2009

Certified by ....
Gunther Roland
Associate Professor of Physics
Thesis Supervisor

Accepted by ....
Thomas J. Greytak
Associate Department Head for Education

Clustering Phenomena from Two-particle Angular Correlations in Proton-Proton and Heavy Ion Collisions

by

Wei Li

Submitted to the Department of Physics
on January 30th, 2009, in partial fulfillment of the
requirements for the degree of
Doctor of Philosophy

Abstract

Results on two-particle angular correlations in proton-proton ($\sqrt{s} = 200$ and 410 GeV), Cu+Cu and Au+Au collisions ($\sqrt{s_{\text{NN}}} = 200$ GeV) are presented over a broad range of pseudorapidity (η) and azimuthal angle (ϕ). The PHOBOS experiment at the Relativistic Heavy Ion Collider (RHIC) has a uniquely large coverage for inclusive charged particles, giving the opportunity to explore the correlations at both short- and long-range scales.

In proton-proton collisions, a complex two-dimensional correlation structure in $\Delta\eta$ and $\Delta\phi$ emerges, which is interpreted in the context of an independent cluster model. The effective cluster size and its decay width are extracted from the two-particle pseudorapidity correlation function at various collision energies and multiplicities.

Similar cluster like short-range structure is also observed in Cu+Cu and Au+Au collisions. The effective cluster size found in semi-central Cu+Cu and Au+Au collisions is comparable to that found in proton-proton collisions but a non-trivial decrease of the size with increasing centrality is observed. Moreover, a comparison between results from Cu+Cu and Au+Au collisions shows an interesting scaling of the effective cluster size with the measured fraction of total cross section (which is related to the ratio of the impact parameter to the nuclear radius, $b/2R$), suggesting a geometric origin.

Further analysis for pairs from restricted azimuthal regions shows that the effective cluster size at $\Delta\phi \sim 180°$ drops more rapidly toward central collisions than the size at $\Delta\phi \sim 0°$. The effect of limited η acceptance on the cluster parameters is also addressed, and a correction is applied to present cluster parameters for full η coverage, leading to much larger effective cluster sizes and widths than previously noted in the literature. Finally, modeling studies are performed toward gaining more physics implications from these observed clustering phenomena.

Thesis Supervisor: Gunther Roland

Title: Associate Professor of Physics

This work is dedicated to my beloved wife, Jie Meng.

Contents

1 Introduction

1.1 Fundamental Forces and Particles

"What is the world made of?" and "What holds it together?"

To explore the most elementary building blocks of matter as well as the common laws governing the interactions between them has been the major goal of physics all along the human history. To date, all known interactions in nature have been categorized into four fundamental types of forces: gravity, electromagnetic interaction, strong force and weak force.

Gravity, which causes apples to fall from trees, was first formulated by Newton's law of universal gravitation in the 1680s, building on the work of Galileo and Kepler. It has then been revolutionized at the turn of 20th century when Einstein introduced the theory of general relativity, and fundamentally reformed the spacetime concept of our world. Being the weakest among the fundamental forces, Gravity's purely attractive, long-range feature, however, makes it dominate the motions of almost all the objects at the astronomical scale. These include the formation of galaxies and stars, orbits of planets, and the evolution of the universe.

The electromagnetic force generates electric and magnetic effects such as the repulsion between like-sign electric charges or the interaction of bar magnets. It is the one responsible for practically all the phenomena one encounters in our daily life. Generally speaking, all interactions at the atomic level trace back to the electromagnetic forces acting on the electrically charged protons and electrons inside the atoms. Periodicity of chemical elements, molecular bindings and chemical reactions are all consequences of electromagnetic interactions. The unification of electricity and magnetism was realized by Faraday and Maxwell in the 1800s.

The second least powerful force after gravity is known as the weak force. As opposed to gravity, the weak force is very short ranged, on the order of 10^{-18} m (about 1000 times smaller than the diameter of an atomic nucleus), and does not act as the binding force of any objects. It was first discovered in the phenomena of nuclear radioactive decay, which typically involves the process in which an unstable atomic nucleus loses energy by emitting ionizing particles and radiations. It has the unique ability of inducing a change in the type, or "flavor" of the initial particle during the interaction. It is also responsible for the breaking of some fundamental symmetries in nature.

The strong interaction, as its name indicates, is the most powerful force in the universe. It was known that proton carries a positive electrical charge, which made them repel from each other under the electric repulsion. However, the fact that multiple protons along with neutrons were still bound together in the atomic nucleus posed the quest of another stronger, attractive force at short distance, overwhelming the electromagnetic repulsion. It was discovered later that the binding force of protons and neutrons in a nucleus is just a residual effect of the interactions between more basic constituents of the nucleons (proton or neutron), namely *quarks* and *gluons*. The strong interaction is described in the Standard Model by the relativistic quantum field theory known as Quantum Chromodynamics (QCD).

The idea that all matter is composed of more basic particles dates back to at least the 6th century BC, when the philosophical doctrine of atomism were studied by ancient Greek philosophers such as Leucippus, Democritus and Epicurus. Up to now, it is widely believed that the standard model of particles contains 12 flavors of elementary fermions (half-integer spin), called quarks and leptons that are divided into three *generations*, and also elementary bosons (integer spin) that mediate the four types of forces including the undiscovered "Higgs" boson. For instance, an object such as a piece of paper consists of innumerable atoms, each of which has a tiny nucleus in the center surrounded by a cloud of electrons, the most common leptons. A proton or neutron inside a nucleus consists of three quarks, which are held together by exchanging strong interacting mediators, gluons. See Table 1.1 and Table 1.2 for a summary of all fundamental particles and forces as well as their properties. A comprehensive review on particle physics can be found in Ref. [1].

1.2 The Quark Model of Hadrons

In the 1950s, with the advent of new experimental techniques as well as cosmic ray studies, a wide variety of massive resonance particles (e.g. $K^{+/-}$, K^0, $\pi^{+/-}$, π^0, Λ, Δ, Σ) have been discovered, namely *hadrons*. There are two subsets of hadrons: *baryons* and *mesons*. Baryons are fermions with half-integer spins, while mesons are bosons with integer spins. The rapid explosion of "particle zoo" made it evident that they could

Generation		First		Second		Third	
Quarks	Name	up	down	strange	charm	down	top
	Symbol	u	d	s	c	b	t
	Charge	+2/3	-1/3	-1/3	+2/3	-1/3	+2/3
	Mass [2]	1.5 – 4.5 MeV	5 – 8.5 MeV	80 – 155 MeV	1.0 – 1.4 GeV	4.0 – 4.5 GeV	174.3 ± 5.1 GeV
Leptons	Name	Electron	Electron Neutrino	Muon	Muon Neutrino	Tau	Tau Neutrino
	Symbol	e^-	ν_e	μ^-	ν_μ	τ^-	ν_τ
	Charge	-1	0	-1	0	-1	0
	Mass [2]	0.511 MeV	$< 2 \times 10^{-6}$ MeV	105.7 MeV	< 0.19 MeV	1777 MeV	< 18.2 MeV

Table 1.1: The properties of the six quarks and leptons. Values of the masses are taken from the best estimates quoted in the Particle Data Book [3]

	Gravitational	Electromagnetic	Weak	Strong
Mediator	graviton	photon	$W^{\pm}$, Z	gluon
Spin-Parity	2^+	1^-	$1^-, 1^+$	1^-
Mass [GeV/c^2]	0	0	80.2, 91.2	0
Range [m]	∞	∞	10^{-18}	$\leq 10^{-15}$
Relative Strength	10^{-38}	10^{-2}	10^{-13}	1

Table 1.2: The fundamental interactions and some of their properties taken from [4].

not all be elementary, but composed of more basic elements. These discoveries led Wolfgang Pauli to exclaim "Had I foreseen that, I would have gone into botany" [1].

The quark model of hadrons was first postulated by physicists Murray Gell-Mann [5] and George Zweig [6] independently in 1964. The Gell-Mann-Zweig model predicted that hadrons are actually composed of particles called *quarks* [2]. There were initially three "flavors" of quarks proposed: "up" (u), "down" (d) and "strange" (s) quark, which were considered structureless at the time. They carry spin-1/2 and fractional unit of charges as listed in Table 1.1. Each hadron consists of essentially three quarks; for example, proton has two u and one d quarks ($p = uud$) and neutron has two d and one u quarks ($n = udd$). On the other hand, each meson is a bound state of a quark with an antiquark (e.g. $\pi^+ = u\bar{d}$).

Gell-Mann [7] and Ne'eman [8] proposed that quarks and antiquarks can be grouped into various baryons and mesons according to the "Eightfold Way" (the term alluding to the Noble Eightfold Path of Buddhism). Mathematically, the arrangement of hadrons can be described by the $SU(3)$ symmetry group. The u, d, s quarks together form a triplet state, corresponding to the fundamental representation of the $SU(3)$ group (see Fig. 1.1). The triplet state is characterized by two quantities:"strangeness" (number of s quarks) and the charge. The combination of a $q\bar{q}$ pair resulted in nine possible states of mesons:

$$3 \otimes \bar{3} = 8 \oplus 1, \qquad (1.1)$$

---

[1] sometimes quoted as saying to Leon Lederman: "Young man, if I could remember the names of these particles, I would have been a botanist"

[2] The name quark originated from James Joyce's famous novel Finnegans Wake: Three quarks for Muster Mark. Zweig originally referred to them as "aces"

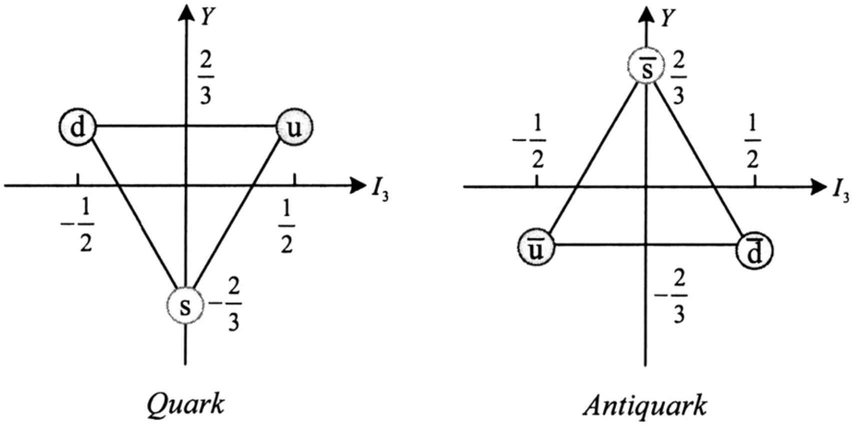

Figure 1.1: Arrangement of u, d, s quarks and antiquarks in triplet states.

including an *SU(3)* octet and an *SU(3)* singlet, illustrated in Fig. 1.2. For the case of baryons, three quark triplet states (*qqq*) are added together, giving a total of 27 possible combinations:

$$3 \otimes 3 \otimes 3 = 10 \oplus 8 \oplus 8 \oplus 1, \tag{1.2}$$

that fit neatly into the spin-3/2 decuplet and the spin-1/2 octet, displayed in Fig. 1.2. The baryon singlet state was eliminated due to the fact that all hadrons are "colorless" (see discussion in Sect. 1.3). This *SU(3)* description of the quark model successfully predicted the unknown Ω^- baryon at that time, which was discovered later at Brookhaven National Laboratory (BNL) [9]. Gell-Mann was awarded the Nobel prize for his pioneering work on the quark model.

There was little further evidence for the existence of quarks until 1968, when the experiment of Deep-Inelastic Scattering (DIS) was deployed at the Stanford Linear Accelerator Center (SLAC) [10]. Energetic electrons were fired as tiny bullets to probe the insides of proton and neutron targets. For electrons scattered off with a large momentum transfer, scattering cross section exhibited a so-call "Bjorken Scaling" behavior [11], which indicated the existence of point-like, charged, spin-1/2 fermion constituents inside the nucleons. It provided the first convincing evidence of the reality of the quark model.

A compelling theoretical argument for the undiscovered charm (c) quark (fourth flavor) was proposed by Glashow, John Iliopoulos, and Luciano Maiani in a paper of 1970s [12]. It was then created and observed simultaneously by two teams under

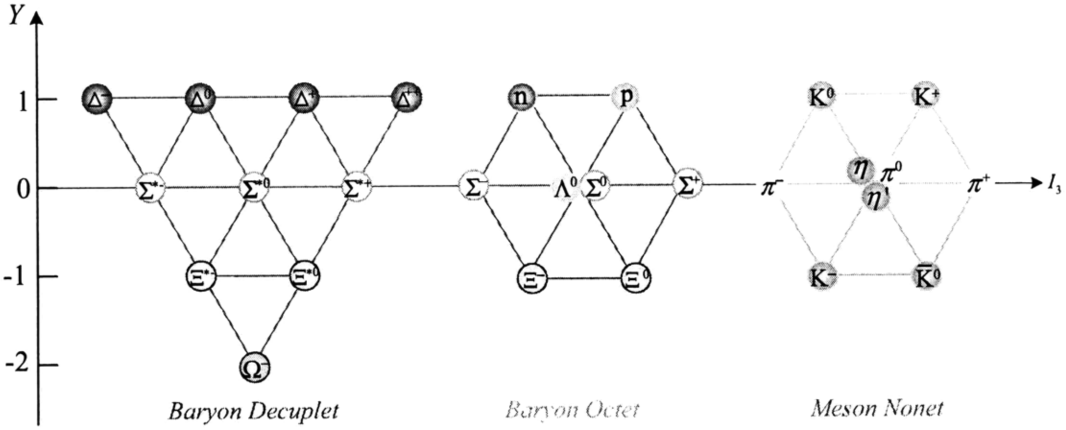

Figure 1.2: Arrangement of various hadrons in the Eightfold Way for baryon decuplet with spin-3/2, baryon octet with the spin-1/2, and meson nonet with spin-0.

Samuel Ting [13] and Burton Richter [14] in November 1974, known as the J/Ψ meson, which was considered a bound state of $c\bar{c}$ pair. In 1977, the bottom quark was observed by Leon Lederman and a team at Fermilab [15]. However, it was not until eighteen years later, in 1995, that the top quark, as a partner of the bottom quark, was finally observed with extremely large mass ($\sim$172.4 GeV) [16, 17].

1.3 Quantum Chromodynamics

Quantum Chromodynamics (QCD) is the relativistic quantum field theory of the strong interactions. It describes the interactions between quarks and gluons, and how they bind together to form various kinds of hadrons.

1.3.1 Color

The naive quark model, described in Sect. 1.2, is clearly unsatisfactory in many ways [18]. According to Pauli's Exclusion principle, the wave function of a baryon has to be antisymmetric when exchanging any of its two identical quarks with each other. The doubly charged Δ^{++} baryon (the $\pi^+ p$ resonance observed in 1951) has a quark configuration of (uuu), which is apparently exchange-symmetric. Furthermore, its spin, $J = 3/2$, requires that three identical u quarks are in the same spin state of $J = 1/2$ $(\uparrow\uparrow\uparrow)$. In order to accommodate the observed properties of Δ^{++}, a completely symmetric ground state of three identical u quarks is inevitable, which is basically forbidden.

The fiasco can be resolved by introducing a new degree of freedom for quarks (a new quantum number): *color.* In analogy with visual perception of white color, a "colorless" baryon is constructed by a combination of red (R), green (G) and blue (B) quarks. If the wavefunction of Δ^{++} particle is rewritten as $(u_R u_G u_B)$, the three u quarks are now distinguishable by their color sectors. Each color has a corresponding anti-color, so a meson might consist of a $\mathrm{R\bar{R}}$, $\mathrm{G\bar{G}}$, or $\mathrm{B\bar{B}}$ pair, which is also colorless.

Experimentally, the existence of color was supported from the measurements of cross-section in e^+e^- collisions. At collision energies above the mass threshold of the $q\bar{q}$ pair and away from resonance states, the ratio in observed cross-sections between the process $e^+e^- \rightarrow q\bar{q} \rightarrow hadrons$ and $e^+e^- \rightarrow \mu^+\mu^-$ suggested that there is still a factor of three discrepancy between the predicted and measured values of the ratio:

$$\frac{\sigma(e^+e^- \rightarrow q\bar{q} \rightarrow hadrons)}{\sigma(e^+e^- \rightarrow \mu^+\mu^-)} \tag{1.3}$$

until the introduction of color [19]. This demonstrated that color is indeed an internal degree freedom of quarks.

1.3.2 Gluons

Each interaction is mediated by a vector boson. Like the photon being the mediator of Quantum Electrodynamics (QED), the interactions between quarks in QCD are propagated by exchanging eight massless gluon fields. However, unlike the neutral photon, the gluons themselves carry color ("charge" of QCD). As a consequence, more complexity is introduced into the theory of QCD. According to the *SU*(3) symmetry of colors, each of the eight gluons carries a color charge and an anticolor charge, which can be represented as:

$$r\bar{b}, r\bar{g}, b\bar{g}, b\bar{r}, g\bar{b}, g\bar{r}, \frac{r\bar{r}-b\bar{b}}{\sqrt{2}}, \frac{r\bar{r}+b\bar{b}-2g\bar{g}}{\sqrt{6}}. \tag{1.4}$$

This configuration arises in exactly the same fashion as the meson octet from the *SU*(3) flavor symmetry (see Sect. 1.2). However, the ninth colorless singlet gluon state:

$$\frac{r\bar{r}+b\bar{b}+g\bar{g}}{\sqrt{3}} \tag{1.5}$$

does not exist in nature. For such a gluon that carries no net color, it would be able to facilitate the strong interactions over macroscopic distances like a photon between colorless hadrons, which apparently never happens. The exchange of a $g\bar{b}$ gluon between

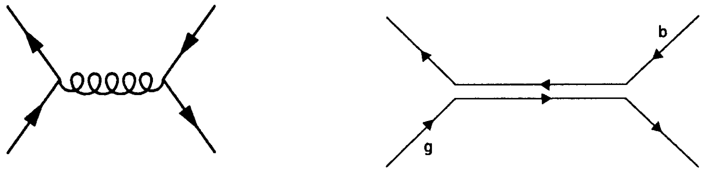

(a) (b)

Figure 1.3: (a) The interaction of two quarks in exchange of a gluon carrying colors [20]. (b) Direction of color flows in the same interaction [20].

a quark and antiquark is shown in Fig. 1.3 as an example.

Experimentally, quantitative studies of DIS results had indirectly inferred the existence of gluons, because quarks only carry about 50% of the total fraction of the proton momentum and 30% of the proton spin. The breaking of Bjorken scaling at small x [3] region also suggested constituents other than three quarks inside the proton [4, 18]. The best evidence for the existence of gluons first came from the observation of three-jet events in e^+e^- at PETRA in 1979, where the third jet was considered to be a high-energy gluon radiated from a quark of the $q\bar{q}$ pair [21]. Further analyses on the properties of this third jet (e.g. angular distribution) also confirmed the postulate of gluons.

1.3.3 The QCD Lagrangian

The Lagrangian, $\mathscr{L}$, is a function that summarizes the dynamics of a system. It was originally introduced in a reformulation of classical mechanics known as Lagrangian mechanics, where the Lagrangian is defined as the kinetic energy, T, of the system minus its potential energy, V [22]. The QCD Lagrangian, that derives the Feynman rules for a perturbative analysis of strong interactions, is given by:

$$\mathscr{L}_{QCD} = \sum_{\alpha} \bar{\psi}_j^{(\alpha)}(i\gamma_\mu D^\mu_{jk} - m^{(\alpha)}\delta_{jk})\psi_k^{(\alpha)} - \frac{1}{4}F^{\mu\nu}_a F^a_{\mu\nu}, \tag{1.6}$$

with the convention of summing over the repeated indices [23]. $\psi_i^{(\alpha)}$ is the fermion field representing quarks with flavor α (= u, d, s,...), mass $m^{(\alpha)}$ and color i=R, G, B. γ_μ are the 4×4 Dirac matrices. The quark covariant derivative $\mathbf{D}_\mu$ is defined as:

$$\mathbf{D}_\mu\psi = (\partial_\mu + i g_3 \mathbf{A}^a_\mu \frac{\lambda_a}{2})\psi. \tag{1.7}$$

---

[3] x represents the fraction of the proton momentum carried by a parton in the infinite momentum frame.

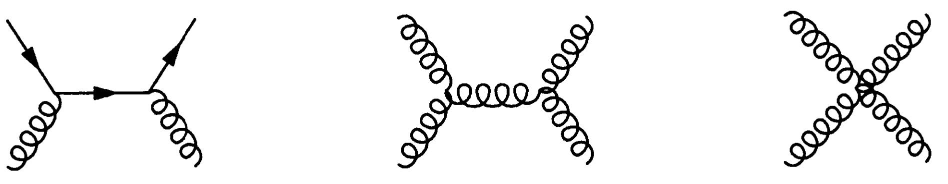

(a) Quark Exchange (b) Gluon Exchange (c) Direct Interaction

Figure 1.4: Examples of the different classes of gluon-gluon interactions [20]. (a) Interaction via quark exchange. (b) Interaction via gluon exchange. (c) Direct interaction.

Here, g_3 is the coupling constant of the theory. λ_a $(a = 1,...,8)$ are the 3×3 generator matrix of the *SU(3)* group, which obey the commutation relations:

$$[\lambda_a, \lambda_b] = 2if_{abc}\lambda_c \; (a, b, c = 1,...,8), \tag{1.8}$$

where f_{abc} are called "structure constants" of *SU(3)*. In the end, the gluon field strength tensor is expressed as follows:

$$F^a_{\mu\nu} = \partial_\mu A^a_\nu - \partial_\nu A^a_\mu - g_3 f_{abc} A^b_\mu A^c_\nu. \tag{1.9}$$

The first term of the QCD Lagrangian $\mathscr{L}_{QCD}$ describes the motion of free quarks as well as their interactions with gluons (see Fig. 1.4(a)), while the second term determines the dynamics of the gluons including the self-interactions among them as shown in Fig. 1.4(b) and Fig. 1.4(c). The gluon-gluon interaction term is a direct consequence of non-zero structure constant f_{abc}, as opposed to the photon in QED, which can only interact with other charged particles, instead of with each other themselves. Theories with structure constant equal to zero are called "Abelian". Otherwise, they are called "Non-Abelian". The most important feature of a quantum field theory is the invariance of physical observables under the local gauge transformation:

$$\psi(x) \to e^{i\alpha_a(x)\lambda_a}\psi(x) \tag{1.10}$$

1.3.4 Asymptotic Freedom and Confinement

In all types of interactions, a coupling constant (usually denoted g) is a number that determines the strength of an interaction. As an example, the fine-structure coupling

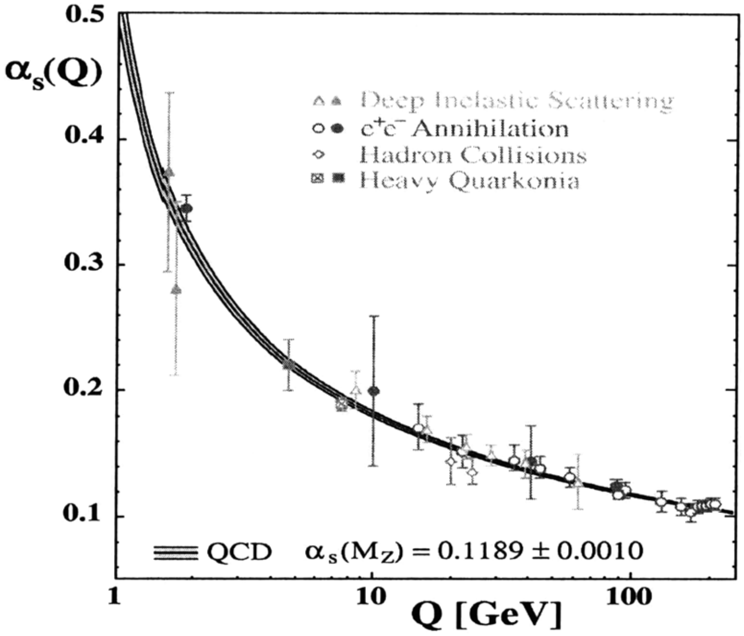

Figure 1.5: World-best measurements of the strong coupling constant as a function of energy scale [24]. NLO (open symbols) and NNLO (closed symbols) calculations are used to extract α_s from the data.

constant in QED is defined as:

$$\alpha = \frac{g^2}{4\pi} = \frac{e^2}{4\pi\epsilon_0\hbar c} \approx \frac{1}{137} \tag{1.11}$$

where e is the charge of an electron, ϵ_0 is the permittivity of free space, $\hbar$ is the reduced Planck constant and c is the speed of light. A well known feature of the fine-structure constant is that instead of being a constant, it actually varies with the length scale that is probed, or equivalently the momentum transfer Q, during the interactions. This can be understood as the effect of screening from the electron-positron pairs constantly excited from the vacuum surrounding a bare charge. The cloud of e^+e^- pairs is polarized by the bare charge in the center, which therefore in turn reduces its magnitude seen by a probe electron. However, as the energy of the probe increases, it goes deeper and deeper inside the virtual e^+e^- cloud and thus feels more net charges, which effectively increases the coupling constant.

Similar effect of vacuum polarization is also present in QCD, where virtual $q\bar{q}$ pairs are created. However, as already mentioned, the peculiar feature that distinguishes QCD from QED is that due to its non-abelian nature, gluons carry color charges, and thus can interact directly among themselves, a property that is not available for neutral photons in QED. Since a quark is always surrounded by a cloud of gluons, the color charges it carries tends to leak into the color cloud via gluon-gluon interactions and distribute uniformly. In this case, when a test quark passes through, the closer it gets to the original quark, the fewer color charges it would feel. This is essentially an anti-screening effect, resulting in a decrease of strong coupling constant with increasing energy scale, known as "asymptotic freedom" [25]. Another intuitive view of this anti-screening effect is to consider the spin response to the external magnetic field. In QED, the spin of an electron tends to align with the direction of the external magnetic field, in such a way as to enhance the field. This is an anti-screening behavior. Thus there is a competition between electric screening via virtual e^+e^- pairs and anti-screening through spin alignment. It turns out that the spin anti-screening effect wins over in QCD [26].

The effective QCD coupling strength in the "one-loop" perturbative approximation at large momentum transfer, Q, yields as follows [23, 28, 29]:

$$\alpha_s \approx \frac{4\pi}{(11-\frac{2}{3}n_f)\ln(Q^2/\Lambda^2)}, \tag{1.12}$$

where n_f denotes the number of quark flavors, parameter Λ is called the "renormalization scale" of QCD below which α_s would become so strong that perturbative treatment is no longer viable. Considering if n_f=6, α_s is always positive and decrease toward zero at very large Q value. This explains the phenomena that in deep inelastic scattering off a nucleon by an extremely energetic probe like an electron, the quark scattered inside the nucleon behaves as an almost free, non-interacting particles when it absorbs a large amount of momentum from the electron probe.

However, a paradox on the other hand seemingly arises that free, isolated quarks have never been observed in nature although they seem to be nearly free within the nucleon. Any attempt to smash two nucleons into their constituent quarks would only produce more and more new types of hadrons. This paradox of confinement is easily overcome by the concept of asymptotic freedom. Moving inside a nucleon, quarks interact with each other by exchanging virtually small amount of momentum, order of a couple of hundred MeV determined by the size of the nucleon. In this regime, the QCD coupling constant α_s is large and the interactions are strong, thus holding quarks together in the form of the nucleons. When trying to pull two quarks away from each other, a color flux tube is formed, of which the potential is positive and proportional to the distance

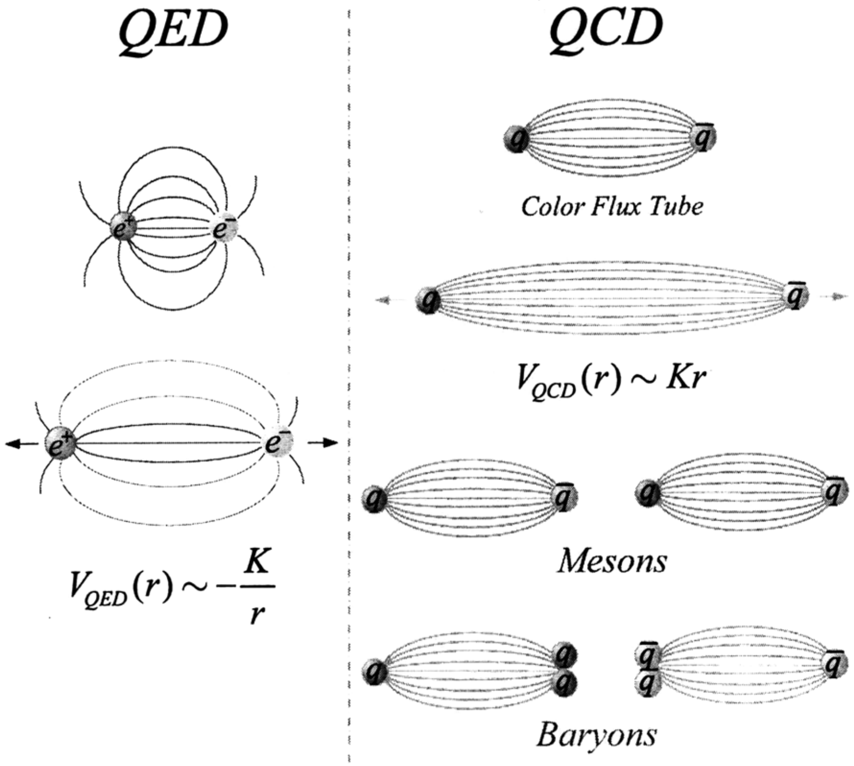

Figure 1.6: A cartoon of hadron production in the color flux tube (Right). As the quarks separate, energy accumulates in the field. A $q\bar{q}$ pair could be produced when the energy reaches the threshold of twice the quark mass. The produced quarks will bind to the original quarks to form two colorless mesons. Baryon production can happen in an analogous fashion, through the production of a diquark, antidiquark pair [27]. On the other hand, in QED (Left), as the electrons move away from each other, the electric field gets weaker. Electrons are eventually set free at infinite distance.

between the two quarks. This means that the farther away two quarks are separated, the more potential energy is accumulated in the flux tube. The amount of energy required to break them apart grows to infinity. However, as the potential energy reaches a certain threshold mass, a pair of new quark-antiquark are created, each of which is attached to one end of two smaller flux tubes broken from the original one. This kind of process will keep on until a stable colorless meson or baryon is produced. This hadronization process, referred to alternatively as fragmentation or string breaking, is responsible for the "jets" of hadrons that show up in particle detectors instead of the originally scattered quarks. See Fig. 1.6 for an illustration of the flux tube breaking process (right) as well as a comparison to the QED (left).

1.3.5 Hadronization Phenomenology

Hadronization is the process of the formation of hadrons out of quarks and gluons after the high-energy collisions occur. Since most of the hadrons come out of the collisions with a transverse momentum (p_T) ~ 400-500 MeV, this enters the low momentum transfer, long distance regime of QCD in which non-perturbative effects become dominant. Phenomenological models were developed to describe the hadronization process. A brief review on various models can be found in [30].

String Fragmentation Model

The most popular model of hadronization is the string model, often referred to Lund String Model [31]. As illustrated in Fig. 1.6, the produced quark and antiquark first move out in opposite directions, transferring their energy into a string-like color flux tube between them, which has a uniform energy per unit length (a linear potential of distance). The string then breaks up into pieces of hadrons via spontaneous $q\bar{q}$ pair production. The breaking of a string could happen at either end of quark or antiquark, or both simultaneously. An earlier version of string model was introduced by Field and Feynman, simply assuming that each parton fragments independently into the hadrons [32]. As the string breaks, hadrons are formed with energy fraction z of the original $q\bar{q}$. It proceeds iteratively until the leftover energy of the string is below some cut-off. The energy fraction distribution is known as the "fragmentation function", which is assumed to be approximately energy scale independent (as observed in the data). The relative transverse momenta of the created $q\bar{q}$ pairs are generated according to a Gaussian distribution. See [33–36] for more descriptions of the string model.

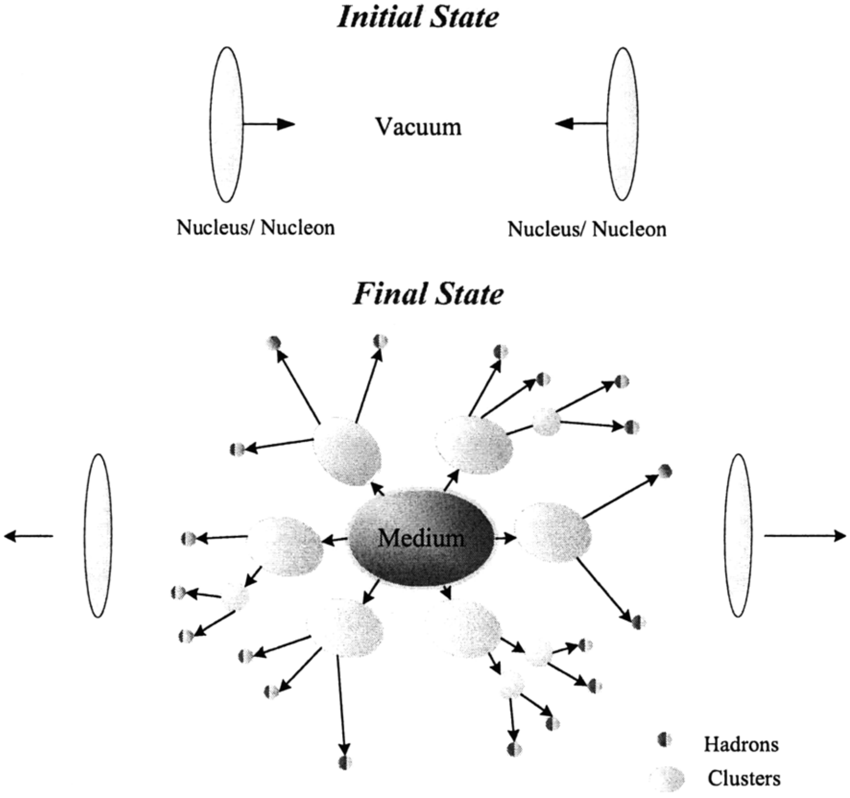

Figure 1.7: Schematic view of hadronization process via clusters.

Cluster Model

The concept of "cluster" hadronization has also proved to be very useful tool in understanding the multiparticle production processes. It is a more generic and economic approach in describing the dynamics of many-body processes. The basic idea is that hadron production takes place in two stages: first of all, color singlet groups of partons, the so-called clusters, are formed after the perturbative phase of parton evolution, and clusters then decay isotropically in its rest frame into the final state hadrons according to the density of states and kinematics [30, 37–39]. See Fig. 1.7 for an illustration of hadron production via clusters. The existence of clusters is strongly supported by many experimental data, in particular the observations of short-range correlations among the produced particles, which is the main topic investigated in this thesis. More discussions on the cluster phenomena can be found in later chapters.

1.3.6 Lattice QCD

At the low energy regime of QCD, as the coupling constant α_s becomes larger, the powerful tool of perturbative calculation is apparently inapplicable. It is important to develop non-perturbative formulation of the QCD theory. The most successful approach is the lattice QCD[40, 41], which have been extensively used in studying nucleon structure and hadronic masses. Also, the physics of a phase transition in the matter of quarks and gluons (as will be discussed later) is also intrinsically non-perturbative.

The basic idea is to discretize the Euclidean space-time into hypercubes with sides of length a. This lattice spacing provides a natural cut-off of order π/a on the momenta so that ultra-violet divergences are no longer present. As long as a is small enough, this discrete version of QCD provides an adequate approximation at that scale. The original Lorentz invariant symmetry is reduced to a hypercubic symmetry by this procedure. However, the local gauge symmetry is still preserved by constructing the gauge-invariant operator, "Wilson Loop". The space-time is converted to a Euclidean signature by using imaginary time ($t \to it$); this allows the evaluation of path integrals using the Monte Carlo technique of sampling. The path integrals can also be related to the partition function of the system, and from this thermodynamic quantities such as energy density and entropy can be extracted [42].

1.4 The QCD Phase Diagram

A phase diagram in physics or chemistry is a type of graph that describes different phases of the substance occupying different regions of the diagram at thermal equilibrium. It is calibrated by the external thermodynamical conditions or control parameters such as temperature, pressure etc. Commonly, lines of equilibrium on a phase diagram corresponds to the boundaries where phase transitions can occur.

Based on different properties near the transition boundary, there are two wide classes of phase transitions. First order phase transitions are characterized by a discontinuity in the thermodynamic quantities like density, pressure. Second order phase transitions, on the other hand, are featured by continuous but nonanalytic behavior of thermodynamic parameters. Critical point specifies endpoint of a phase boundary, beyond which two phases become indistinguishable. The characteristic length scale (or correlation length) goes to infinity at the critical point.

Being as such a remarkable fundamental theory of quarks and gluons, QCD should

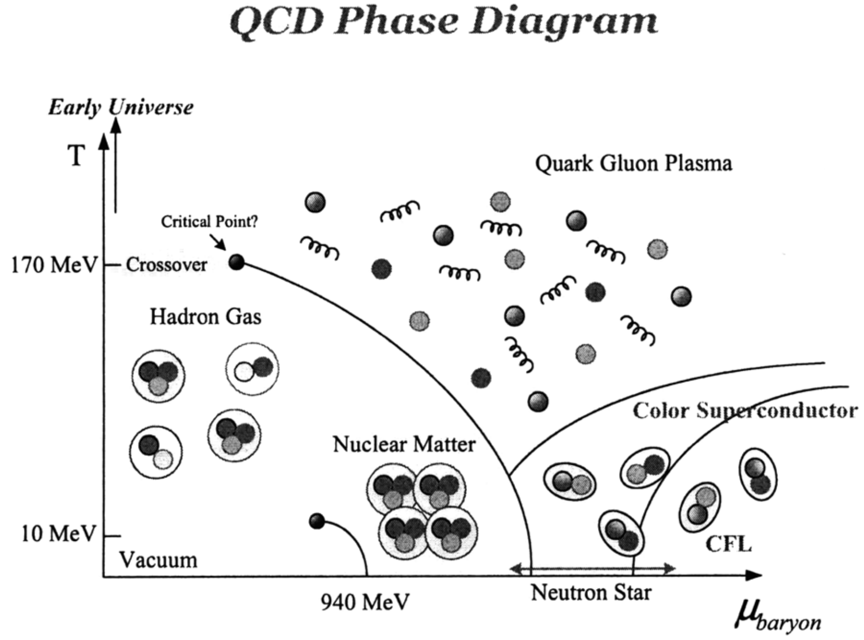

Figure 1.8: A schematic of the QCD phase diagram of nuclear matter in terms of the temperature (T) and baryon chemical potential (μ_B).

have its well defined thermodynamical properties, the knowledge of which is essential for understanding the nature of strongly interacting systems at the parton level. A contemporary view of the QCD phase diagram is illustrated in Fig. 1.8, which shows a rich structure with distinct phases of the QCD matter. The control parameters are temperature T and baryon chemical potential μ_B [4].

In the voyage of exploring the QCD phase diagram in Fig. 1.8, we start from the ordinary nuclear matter phase at low temperature with μ_B around the mass of a nucleon (~ 940 MeV). This is the condition where our daily life lives in. At this regime, quarks and gluons are confined inside nucleons, which are strongly bounded into droplets of nuclei. Going toward lower values of μ_B, or at temperature above the nuclear binding energy (~ 10 MeV), the nuclear matter evaporates into a gaseous phase of hadrons, similar to the liquid-gas transition of the molecular matter [43]. In the sections below, the states of matter at two extremes on the diagram are reviewed: high temperature but low density, and low temperature but high density. The possibility of a critical point is also discussed.

---

[4] The chemical potential characterizes the amount of energy required to add another constituent into the system.

1.4.1 Color Superconductivity

Squeezing the nuclear matter harder at low temperature toward extremely high μ_B region, a first order phase transition is expected to occur and the system turns into a weakly interacting Fermi liquid of quarks [44, 45]. "Cooper pairs" of quarks, $\langle qq \rangle$, are formed by an attractive interaction, and new condensates of "color superconductivity" would develop, a tendency toward spontaneous breaking of color symmetry in analogy to the superconductivity in condensed matter physics [46]. In this color superconducting phase, five of the eight gluons become massive via the Anderson-Higgs mechanism [47, 48], similar to the familiar "Meissner effect". Of course, note that it is different from chiral symmetry breaking in QCD at μ_B=0, which occurs in color singlet quark-antiquark pairs, $\langle q\bar{q} \rangle$.

However, unlike electrical superconductor, different flavor and color species of quarks make the color-superconducting quark matter in many varieties, each of which is a separate phase of matter. In particular, by introducing the strange quark (s) at ultra-high density $\mu_B \gg m_s$ ($\sim$ 100 MeV), where $SU(3)$ flavor symmetry of three massless quarks becomes more reliable, many new features are revealed in a three flavor theory of color superconductivity [49]. In this theory, $SU(3)_{flavor}$ and $SU(3)_{color}$ symmetry can be broken in a correlated fashion, leaving essentially only a global symmetry $SU(3)_{color+flavor}$ under which rotations in color and flavor space always happen simultaneously. This is the so-called "Color-Flavor Locking" (CFL) [49, 50]. Color superconductivity or color-flavor locking phenomena is directly relevant to the description of the core of collapsing neutron stars under its own gravity, and also neutron star collisions [51].

1.4.2 Quark Gluon Plasma

The QCD phase diagram can also be probed following another path starting from the origin at $T = 0$ and μ_B=0, where the matter is heated up to higher and higher temperature, while being kept at low baryon density (mostly a system of pions). As the temperature increases, more and more hadrons are excited from the vacuum. Since the hadrons all have roughly the same size ($\sim$ 1 fm), they start to overlap with each other at a certain critical temperature, T_c. Above T_c, quarks and gluons inside nucleons are deconfined and the broken chiral symmetry at $T = 0$ is restored, as a consequence of asymptotic freedom of strong interactions. The hadronic system dissociates into a weakly interacting gas of quarks and gluons, known as the Quark Gluon Plasma (QGP) [52, 53]. The thermodynamic properties of QCD can be reliably calculated by the Lattice Gauge Theory at

μ_B=0, which predicts a critical temperature T_c of around 170 MeV ($\sim 10^{12}$ K in terms of temperature) from Monte Carlo lattice QCD simulations [54]. The transition is more likely to be a smooth crossover from hadronic phase to partonic phase, as opposed to a first order phase transition at high baryon density region, because of non-zero masses of the constituent quarks, as opposed to a first order phase transition at high baryon density region. According to the theory of thermodynamics, the energy density of an equilibrated system is proportional to its degree of freedom. The energy density of a relativistic gas system is easily obtained from the grand canonical ensemble [42]:

$$\epsilon = 3D\frac{\pi^2}{90}T^4, \tag{1.13}$$

where D is the degree of freedom of the system. For a gas of massless pions, D_π is simply the number of massless Nambu-Goldstone bosons in n_f flavors: $D_\pi = n_f^2 - 1$. In the QGP phase, D_{QGP} is determined by:

$$\begin{aligned} D_{QGP} &= D_{gluon} + \frac{7}{8}D_{quark}, \\ D_{gluon} &= 2_{spin} \times (n_c^2 - 1), \\ D_{quark} &= 2_{spin} \times 2_{q\bar{q}} \times n_c \times n_f. \end{aligned} \tag{1.14}$$

Here, n_c and n_f refer to the number of colors and flavors. The factor 7/8 between quarks and gluons originates from the difference in statistics. With the deconfinement of quarks and gluons, the hidden color degree of freedom has released in the QGP matter, which significantly enhances the density of the system. Fig. 1.9 [54] shows the lattice calculation on the energy density of the QCD matter as a function of the temperature. It is widely accepted that a weakly interacting QGP is the form of matter at the early universe after the big bang.

1.4.3 Critical Point

The first order phase transition at low T along μ_B axis and a smooth crossover at small μ_B going up in T implies the existence of a critical point at the end of the first order phase boundary (see Fig. 1.8), where large fluctuations in thermodynamic quantities should be observed.

However, the theoretical determination of this critical point on the phase diagram is still a formidable task at the moment. Lattice calculation at finite μ_B suffers from the

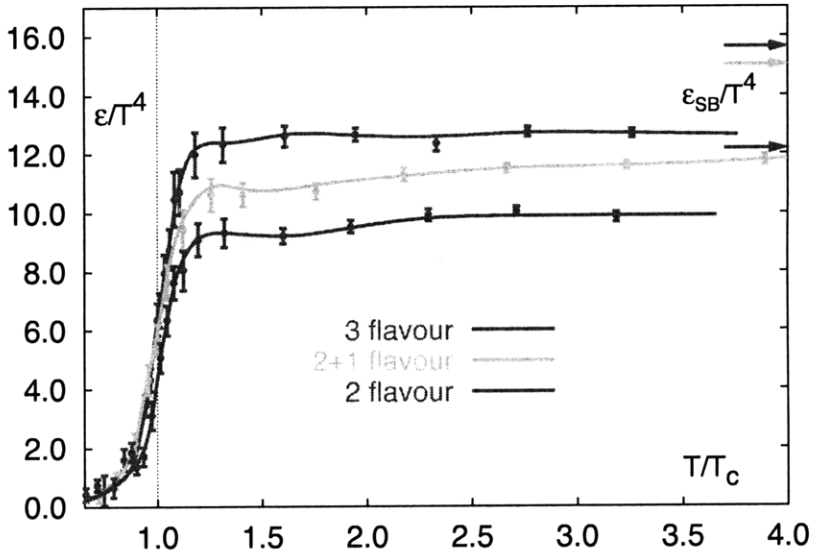

Figure 1.9: Diagram of a crossover from hadronic to QGP phase in lattice QCD calculations [54]. The quantity ϵ/T^4 represents the number of degrees of freedom in a system. ϵ_{SB}/T^4 corresponds to the Stefan-Boltzmann limit of an ideal gas non-interacting system. The critical temperature T_c at transition is around 170 MeV.

notorious "fermion sign problem" [55], and the precise location of the critical point is very sensitive to the value of the input quark mass [56]. The experimental perspectives of searching for such a critical point were initially attempted in the studies of event-by-event fluctuations in Pb+Pb collisions at SPS over the energy range of $\sqrt{s_{\rm NN}} = 5 - 15$ GeV [57]. A low-energy scan program at RHIC was initiated in 2010, in order to further investigate this topic. Future dedicated CBM experiment at FAIR-GSI was also planned in 2014, hoping to create a low temperature and baryon rich matter, and discover the critical point.

1.5 Relativistic Heavy Ion Physics

To probe the properties of QCD at high temperature, possibly a new phase of deconfined quarks and gluons, the most effective experimental technique is to accelerate heavy nuclei to extremely high kinetic energies and smash them head-on so that a significant amount of energy will be deposited in a small but sizable region of space during a short time. As emphasized by T. D. Lee, "high energy heavy-ion collisions may provide a valuable tool to examine the puzzles of symmetry breaking and quark confinement in strongly interacting quark-gluon systems" [58].

Currently, the Relativistic Heavy Ion Collider (RHIC) at Brookhaven National Laboratory (BNL) is the most powerful heavy ion collider in the world where d+Au, Cu+Cu and Au+Au collisions happen at $\sqrt{s_{\rm NN}} = 200$ GeV. In late 2009, the Large Hadron Collider (LHC) at European Organization for Nuclear Research (CERN) is expected to collide Pb+Pb ions at much higher energies (× 30). Gold nucleus, one of the heaviest stable elements, was used primarily in the ion beam at RHIC. Its nucleons are densely packed and the system size is sufficient large so that a hydrodynamic description becomes potentially sensible.

While the expected hot matter could be created, it will expand, cool off and hadronize into thousands of particles. Each of these particles gives a clue as to what might have happened during the collisions. A vast variety of experimental observables have been proposed and studied. There are strong evidences that a new type of strongly interacting matter with extremely high energy density, that is well above the predicted critical value of phase transition by lattice QCD. The evolution of the system behaves like a perfect liquid and can be described by an almost ideal hydrodynamics. However, to claim the discovery of quark-gluon plasma, more unambiguous signatures of color deconfinement and thermalization are still needed.

The four experiments at RHIC have released "white papers" in 2005, with their critical assessment of the observations after 4 years runs at RHIC [59–62]. The latest experimental and theoretical developments in the field of heavy ion physics have been always presented in the "Quark Matter" international conference, the proceedings of which can be found in Ref. [63–66].

1.5.1 Hot and Dense Medium

A crude estimate of initial energy density of the matter created in the heavy ion collisions can be obtained under the so-called Bjorken hydrodynamics, with the assumptions of longitudinal boost-invariance and free streaming expansion [67]. Shortly after the collision, the system is expected to undergo a rapid expansion, especially along the longitudinal direction at almost the speed of light since it carries large fraction of initial energy from the nuclei. For a head on gold-gold collision, it is reasonable to approximate the volume of the system as a cylinder with transverse area equal to that of a gold nucleus, $\mathscr{A}$, and length that grows as a function of time when the system expands longitudinally, $2ct$. It is also natural to consider the central rapidity region where the energies of particles are mostly produced during the collision. Ignoring the possible interactions among the produced particles themselves, the total energy contained within the cylinder is written as:

$$E = \langle E_T \rangle \frac{dN}{dy} \times \Delta y = \langle E_T \rangle \frac{dN}{dy} \times \left(\frac{d}{t} \right). \tag{1.15}$$

Here, dN/dy is the produced particle density per unit rapidity (see Fig. 1.10(a)), and $\langle E_T \rangle$ denotes the average transverse energy per particle. Δy is the rapidity gap that the system spans. It is basically a measure of the longitudinal velocity (d/t) as proved in Appendix B. Using Eq. 1.15, the system energy density thus can be calculated as:

$$\epsilon \approx \langle E_T \rangle \frac{dN}{dy} \times \left(\frac{1}{2\mathscr{A}t} \right) \approx \frac{\sqrt{(0.500\ \mathrm{GeV})^2 + m_\pi^2}\,(700)\,(3/2)}{(1 \rightarrow 2\ \mathrm{fm})\,\pi\,(6.5\ \mathrm{fm})^2} \approx 4 \rightarrow 2\ \mathrm{GeV/fm}^3 \tag{1.16}$$

It is assumed that all particles are pions with an average transverse momentum $\langle p_T \rangle =$ 500 MeV/c (see Fig. 1.10(b) [59]). The measured particle rapidity density for the most central Au+Au collisions is roughly 700 (see Fig. 1.10(a) [68] for the results per participating nucleon) with a factor (3/2) to account for the undetected neutral pions. The radius of gold nucleus is taken to be approximately 6.5 fm. The time scale t considered should not be too long since we are mostly interested in the initial state of the matter right after the collisions. It also, on the other hand, shouldn't be too short since the thermodynamic quantities are poorly defined for a system far beyond the local thermodynamic equilibrium. The measurement of elliptic flow (see discussion in Sect. 1.5.3) places an upper limit on the formation time of QGP at $\tau_0 \lesssim 1 \rightarrow 2$ fm/c [69]. This rough estimate of the energy density of the matter produced in the relativistic heavy ion collisions in Eq. 1.16 already far exceeds that of a proton, which is approximately 0.45 GeV/fm^3. It implies that the system at such high energy density is no longer at hadronic degree of freedom. Five nucleons or so are overlapped with each other. The relevant constituents of the matter are more likely to be deconfined quarks, antiquark and gluons.

1.5.2 Strongly Interacting Matter

The property of a medium can be directly explored using energetic probes to study their interactions with the medium. In ultra-relativistic heavy ion collisions, natural

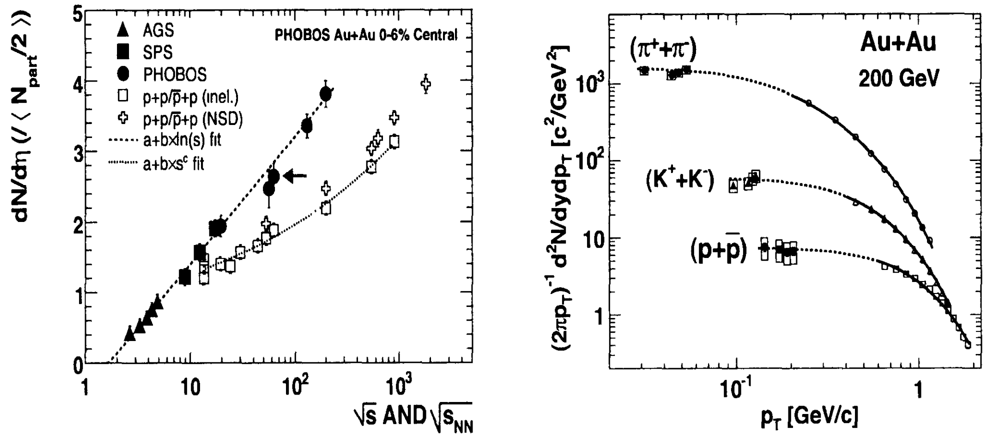

(a) (b)

Figure 1.10: (a) Normalized pseudorapidity density of charged particles emitted within $|\eta| \leqslant 1$ in p+p (p+$\bar{\text{p}}$) and central Au+Au (AGS and PHOBOS at RHIC) and Pb+Pb (SPS) collisions as a function of nucleon-nucleon center-of-mass energy [68]. (b) Transverse momentum distributions of identified charged particles emitted near midrapidity in central Au+Au collisions at $\sqrt{s_{\text{NN}}} =$ 200 GeV [59, 70].

probes of high energy partons, or "jets", are produced in the hard scattering processes of QCD. Traveling through the medium, these high-momentum partons are expected to undergo multiple interactions inside the medium and lose their energies either through collisional energy loss or medium-induced gluon radiation, the latter being the dominant mechanism in the QGP or RHIC.

Studies of particle yield with large transverse momentum can be used to explore the level of interactions present in the hot and dense medium. Measurement of the nuclear modification factor (R_{AA}), defined as the ratio of the charge hadron spectra observed in the nucleus-nucleus collisions to that in p+p collisions scaled by the assumption of binary collision number (N_{coll}, see Appendix C for details) of the hard processes, showed a strong suppression in high-p_{T} particle yield by a factor of almost 5 as shown in Fig. 1.11(a) [72]. Since this suppression, however, is not present in d+Au collisions, it suggests a final-state effect of the matter created in the heavy ion collisions.

The quenchings of high energy jets have also been demonstrated in the analysis of dihadron correlations, where the signature of back-to-back dijets was significantly modified. Figure 1.11(b) [60] shows the azimuthal correlation functions of hadrons with $p_{\text{T}} > 2$ GeV correlated to a trigger particle with $p_{\text{T}} > 4$ GeV. Pairs taken from the same

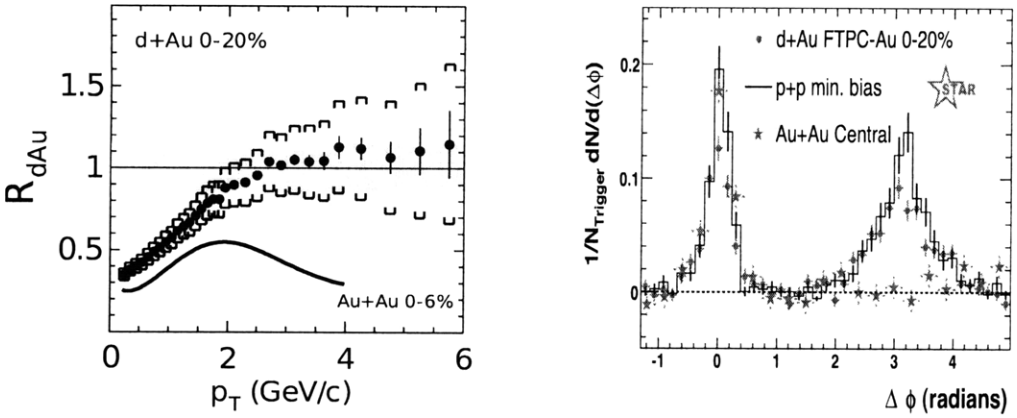

Figure 1.11: (b) Two-particle azimuthal correlations with respect to the high-p_T hadrons in p+p, d+Au, and Au+Au collisions [60]. (a) Nuclear modification factor in 0-20% central d+Au and 0-6% central Au+Au collisions measured by PHOBOS [71].

jet show up as a correlation structure at near-side ($\Delta\phi \sim 0$), which is similar for the p+p, d+Au, and Au+Au events. The away-side ($\Delta\phi \sim \pi$) correlation structure for pairs taken from back-to-back jets, on the other hand, has completely disappeared in central Au+Au events [73]. This is caused by the interactions of hard-scattered partons traversing a nearly opaque medium, and losing a large fraction of their original energies. By selecting a high-p_T leading particle, the jet is biased to be close to the surface of the volume. Therefore, the near-side correlation is less affected.

1.5.3 Perfect Liquid

In search for evidence of QGP matter, one critical issue addressed is whether the system reaches the local thermal equilibrium. Local thermal equilibrium implies the collective behavior during the evolution of the system . The collective flow is driven largely by the pressure gradient which is determined by the density gradient of the system. In a non-central heavy ion collision, the asymmetric shape of the overlapping region results in the anisotropy of its density gradient, and thus pressure gradient. This initial anisotropy in the coördinate space is eventually translated into the final-state momentum space, leading to a non-uniform azimuthal distribution of particles, a phenomena called “elliptic flow” [76, 77]. The magnitude of elliptic flow is characterized by the second Fourier coefficient of the particle azimuthal distribution relative to the reaction

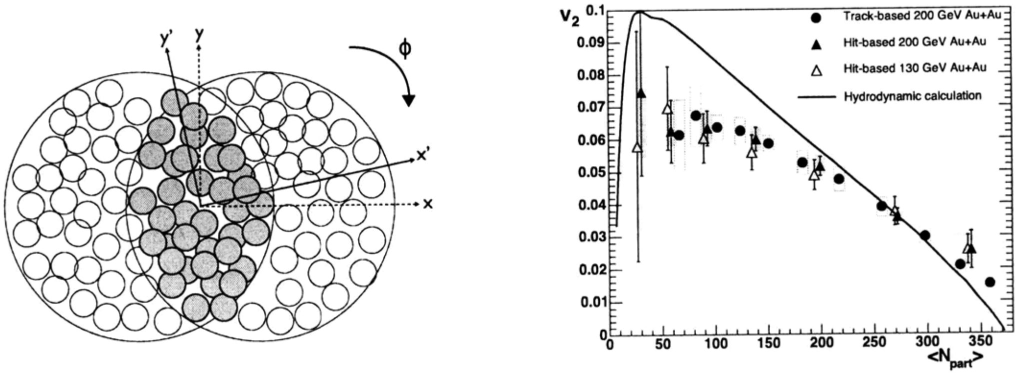

Figure 1.12: (a) Illustration of a non-central nucleus-nucleus collision depicted in the transverse plane [74]. (b) Elliptic flow (v_2) measured at $|\eta| \leqslant 1$ as a function of centrality in Au+Au collisions at $\sqrt{s_{\rm NN}}$=130 and 200 GeV using two different methods. The curve shows the prediction from a relativistic hydrodynamics calculation [75].

place angle[5], $v_2 = \langle \cos 2(\phi - \Psi_0) \rangle$, as shown in Fig. 1.12(b) [78] measured in Au+Au collisions as a function of centrality.

The presence of unexpectedly large elliptic flow inferred that the system has thermalized at the very early state after the collisions happens. The interaction is strong and mean free path is close to zero, similar to the conditions of a liquid rather than a gas as originally expected. Otherwise, any isotropic free-streaming of the source would diminish the initial anisotropy. By comparing the experimental results to the ideal hydrodynamic calculation [75], an upper-limit was set on the QGP formation time, used in estimating the initial energy density of the system in Sect. 1.5.1, as well as the possible shear viscosity which has the effect of dissipating the flow energy [79]. Furthermore, an intriguing observation that the differential elliptic flow $v_2(p_T)$ appears to scale with constituent quark number ($n_q = 2$ for mesons and 3 for baryons) [80] provides stronger evidence on the relevance of the partonic degree of freedom for the matter created in the heavy ion collisions.

---

[5] The reaction plane, Ψ_0, is conventionally defined as the plane where the impact parameter vector resides in. In QM2005, the PHOBOS collaboration pointed out that due to the event-by-event fluctuations of the distributions of participating nucleons, the actual orientation of the elliptic overlapping region (illustrated in Fig. 1.12(a) [74]) varies event-by-event, which provides a more appropriate definition of the reaction plane.

1.6 Overview of this thesis

This thesis presents results on inclusive charged two-particle angular correlations in p+p ($\sqrt{s} = 200$ and 410 GeV), Cu+Cu and Au+Au ($\sqrt{s_{\text{NN}}} = 200$ GeV) collisions over a broad range in phase space using the PHOBOS detector at RHIC. The observed correlations are interpreted in the context of the cluster model. The effective cluster size and decay width are estimated from the two-particle pseudorapidity ($\eta = -\ln(\tan(\theta/2))$) correlation functions, and presented as a function of collision energy and event multiplicity for p+p collisions, and the fraction of total inelastic cross section for Cu+Cu and Au+Au collisions.

The data used in this work were collected by the PHOBOS multiplicity array, which is a single-layer silicon detector with a broad coverage of $-5.4 < \eta < 5.4$ over almost full azimuthal angle. The experimental setup of the PHOBOS detector, as well as the RHIC accelerator, are described in Ch. 2; the procedures for calibrating the raw silicon signals are discussed in Ch. 3; Ch. 4 focuses on the procedure of characterizing the collisions events, particularly the collision vertex reconstruction and centrality determination, which involve different methods ranging from low multiplicity p+p system to highest multiplicity Au+Au collisions.

The reconstruction of the physics object used in this analysis, "particle hit", is described in Ch. 5. The technical challenges of dealing with secondary particles and high occupancy are presented. Both of these effects would modify the measured correlations from the primary tracks. Using a single layer silicon of the PHOBOS Octagon detector to measure the particles in the correlation analysis, secondary hits were partially rejected by cutting on the deposited energy. The high hit density of the Octagon in the central Au+Au event, especially at the mid-rapidity , caused the loss of particles. This is compensated in a procedure to weight hits by the local occupancy.

Analysis procedures, including the corrections applied, are detailed in Ch. 6 and Ch. 7. Final results are presented in Ch. 8 as well as their connections to the theoretical models, i.e. independent cluster model. In the end, various studies on modelings are carried out in Ch. 9, aiming toward the understandings of these observed clustering phenomena.

2 The PHOBOS Experiment

The analysis presented in this thesis used data collected by PHOBOS, one of four heavy ion experiments at the Relativistic Heavy Ion Collider (RHIC) located at Brookhaven National Laboratory (BNL). PHOBOS was designed to study the global event characteristics of heavy ion collisions. During five years of successful operations, billions of p+p, d+Au, Cu+Cu, and Au+Au collisions were recorded over a broad range of center-of-mass energies. In 2006, the PHOBOS experiment was decommissioned and the collaboration has been entirely focusing on data analysis since then. The PHOBOS collaboration consists of approximately 60 physicists from 8 institutions. A list of current members and institutions at PHOBOS can be found in Appendix A.

2.1 Relativistic Heavy Ion Collider

The Relativistic Heavy Ion Collider (RHIC) [81, 82] at Brookhaven National Laboratory (BNL) was constructed to collide heavy ions in a variety of species (primarily Au^{+79}) over a wide range of energy (up to center-of-mass energy of 200 GeV per nucleon pair), including collisions between ions of unequal nucleon numbers (d+Au) and polarized protons. Four experiments were built to study these collisions, two bigger ones (STAR[1], PHENIX[2]) and two smaller ones (PHOBOS[3], BRAHMS[4]). The STAR detector [83] featured a large barrel Time Projection Chamber (TPC) which could identify the trajectories of almost all charged particles at mid-rapidity. The PHENIX detector [84], including two large muon hodoscopes, was designed specifically to measure direct probes of the collisions such as electrons, muons and photons. The BRAHMS experiment [85] was equipped with two movable spectrometer arms to study identified particle production over a broad rapidity range, especially at the very forward region. The setups of the

---

[1] Solenoidal Tracker At RHIC

[2] Pioneering High Energy Nuclear Experiment

[3] The original experiment MARS (Modular Array for RHIC Spectroscopy) was rejected. A smaller setup under the name of one of the moons of Mars was later built.

[4] Broad Range Hadron Magnetic Spectrometers Experiment at RHIC

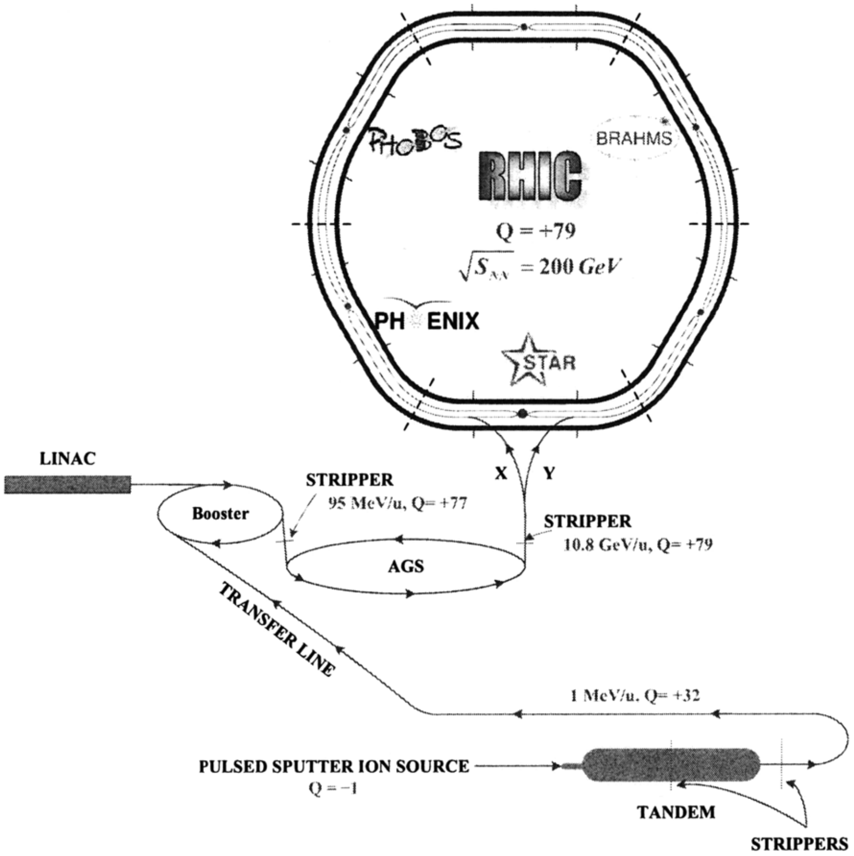

Figure 2.1: A schematic of the AGS-RHIC complex layout. Fully stripped Au^{+79} ions were injected into the two RHIC rings via X and Y respectively. A complete description of the ion acceleration chain can be found in the text. Proton beams for the study of p+p or p+A collisions are injected directly to AGS by the Linear Accelerator (Linac).

PHOBOS experiment are described in Sect. 2.2. The layout of the whole RHIC complex at BNL is displayed in Fig. 2.1.

2.1.1 Tandem Van de Graaff

The journey of the relativistic gold ion beam (Au^{+79}), that circulate in the RHIC rings, begins from a pulsed sputter source at the Tandem Van de Graaff accelerator. Negative ions (Au^{-1}) are first produced by a cesium sputter ion source and accelerated to the high voltage terminal of the Van der Graaff, which consists of two static potentials arranged in sequence. A +15 MV electrostatic-field of the first Van de Graaff machine accelerates these ions through a 2 g/cm^2 carbon stripper foil, which strips them to the +12 charge state. Then the positively charged ions enter the second -15 MV potential where they are accelerated again, reaching an energy of 1 MeV per nucleon. Upon exiting from the Tandem, the ions undergo further foil-stripping. The ones with charge state +32 are picked by the magnetic selector and then transferred to the Booster synchrotron through the Tandem to Booster (TtB) transfer line for further acceleration and stripping.

2.1.2 The Booster synchrotron

The Booster synchrotron played an essential role in producing higher intensity proton beams and the use of heavier ion species (e.g. Au) in the Alternating Gradient Synchrotron (AGS) (see discussion in Sect. 2.1.3). Leaving the Tandem Van de Graaff, heavier ions are still carrying a significant number of electrons. If any of these electrons is stripped off the ions during the beam-gas interactions, the original path they've followed would be deflected, resulting in significant beam loss. The AGS Booster has superior vacuum compared to the AGS and supplies more fully stripped ions with higher energy. After acceleration and a subsequent stripping during the transfer of the ions to the AGS, a Au^{+77} beam exists with kinetic energy of 95 MeV/nucleon. This state is specifically chosen because of its stability (i.e. only the K-shell electrons remain on the ion).

2.1.3 Alternating Gradient Synchrotron

The Alternating Gradient Synchrotron (AGS) is the first accelerator to implement the concept of strong focusing, by which not only vertical but also horizontal dimension of the beam is focused without increasing the size of the machine. This is achieved by making the magnet pole tips curved (like a "C-shaped") and alternating the orientation of these magnets, so that some of their field gradients face outward and some inward. The curved pole tips provide a better field gradient. Gold ions are accelerated up to 10.8 GeV/nucleon in the AGS. Beam is then transferred through the AGS to RHIC transfer line where gold ions are stripped off their last two electrons. Fully stripped Au^{+79} ions then enter the RHIC rings.

2.1.4 Relativistic Heavy Ion Collider Ring

RHIC consists of two concentric quasi-circular superconducting storage-accelerator rings, called blue and yellow rings, respectively. It is about 3.8 km in circumference and built from six arc sections (356 m) and six straight sections (277 m) for beam injection or interaction (see Fig. 2.1). In the middle of the straight sections lie the six interaction points, where the beams are focused down to a small spot size and collide head-on. Superconducting technology is used for the RHIC magnets in order to achieve higher magnetic field over long periods of time. Liquid helium-cooled (< 4.2 K), superconducting dipole magnets with a strength of 3.458 T bend the beam around the arc sections, while quadrupole magnets keep the beam tightly focused. On either side of each interaction point locate a common set of dipole magnets, the DX (± 10 m) and D0 (± 23 m) magnets. The two beams are brought together to share a single beam pipe by a pair of D0 magnets, and then steered to collide by two DX magnets.

Particles travel around the beam pipe in bunches of $\sim 10^9$ ions. The acceleration and storage of the beam are accomplished by two radio-frequency (RF) systems. The bunches are captured in stationary buckets of the so-called acceleration RF-system operating at 28 MHz. After reaching the operating beam energy, the bunches are transferred to the so-called storage RF system in order to limit the bunch length growth ($\sigma_L \approx 25$ cm) due to intrabeam scatterings. As the bucket size is much smaller than the interspacing between bunches, many buckets are actually empty. A "crossing clock" is thus used by RHIC to inform the experiments when two filled buckets should be colliding. Luminosity for the heaviest ions are designed to be in the 10^{26} - 10^{27} $\mathrm{cm}^{-2}\mathrm{s}^{-1}$ range. The higher Au+Au total inelastic cross section results in interaction rates comparable to p+p colliders with several orders of magnitude higher luminosity.

2.2 PHOBOS Detector Setup

The goal of the PHOBOS detector is to study the global features of the heavy ion collisions and potentially search for new physics phenomena. A 4π multiplicity silicon array was ideally suited to detect nearly all charge particles produced in the collisions with very high event triggering rate. To investigate the dynamical evolution of the system in more details, a two-arm silicon Spectrometer was built near mid-rapidity, which permitted full track reconstruction of about 2% of total particles produced in each collision. Furthermore, a series of detectors were places at the forward region down the

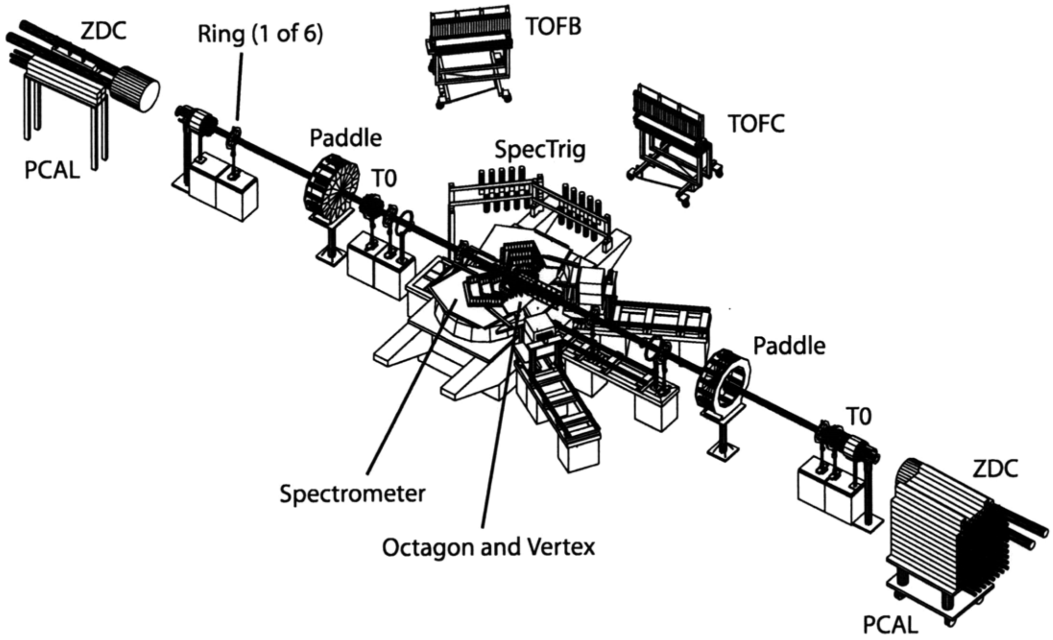

Figure 2.2: The complete PHOBOS detector setup during 2003 d+Au run.

beam pipe mainly for collision impact parameter determination and event triggering. A diagram of the complete PHOBOS detector is shown in Fig. 2.2.

2.2.1 Multiplicity Array

The PHOBOS multiplicity array was a set of single-layer silicon detector enclosing the beam pipe. It was composed of a central barrel Octagon detector, which covered a pseudorapidity range $|\eta| < 3.2$ over almost full azimuthal angle, and two sets of three Ring counters oriented perpendicular to the beam axis extending the acceptance coverage up to $|\eta| < 5.4$. The measurement was performed by recording the energy deposited in the silicon by the charged particles.

Octagon Detector

The structure of the Octagon detector is shown in Fig. 2.3 [86]. 92 silicon pad sensors were arranged in a 1.1 m long, 90 mm face-to-face diameter barrel surrounding the beam pipe mounted in 8 faces. For each face of the Octagon, there were up to 13 sensors. Sensors directly in front of the Spectrometer arms and the Vertex detectors were removed for unimpeded acceptance of the other detector systems (i.e. important for

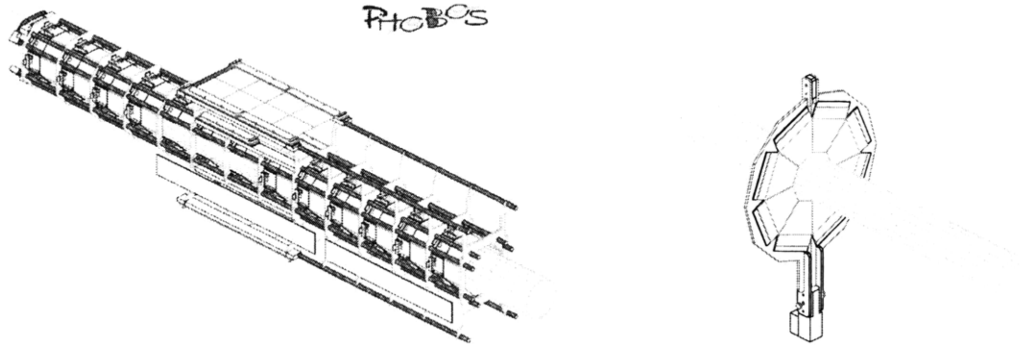

(a) Octagon and Vertex Detectors (b) Ring Detector

Figure 2.3: The PHOBOS multiplicity detectors [86].

measurement of low transverse momentum particles). The thickness of the Octagon sensors was chosen to be around 300 μm, as all the silicons in PHOBOS. Each sensor was 84 mm in length and 36 mm wide, divided into 120 pads arranged in 4 rows of 30 pads each, running along the z-direction (along the beam line). The angular granularity of the Octagon was determined by the fixed size of the readout pads which was 11.25° ($\sim$ 0.2 radians) in ϕ and ranged from 0.006 to 0.05 unit in η. About 95% of the area of each Octagon sensor was active and the gaps between them were 1 mm wide.

A light-weight Aluminum frame was also constructed as the supporting structure of the silicon sensors (see Fig. 2.3(a) [86]). Part of the frame was fabricated from Aluminum tubes, through which chilled water was circulated in order to cool the readout electronic chips affixed to each sensor. The low-Z, low mass frame near the collision point had the advantage of limiting the effect such as secondary particle production and multiple scatterings. Despite the relatively large size of the pads (2.708 mm x 8.710 mm), the Octagon sensors achieved a signal-to-noise ratio comfortably above the design goal of $S/N \approx 12/1$.

Ring Detectors

Particles emitted at very forward regions were detected by the Ring detectors. There were six Ring detectors in all, placed ±1.13 m, ±2.35 m and ±5.05 m from the interaction point. These detectors observed particles at forward pseudorapidity $3 \le |\eta| \le 4$, $4 \le |\eta| \le 4.7$ and $4.7 \le |\eta| \le 5.4$, respectively. Each Ring detector consisted of eight trapezoidal silicon sensors containing 64 pads (8 radial columns × 8 rows). The pad sizes ranged from approximately 3.8 mm × 5.1 mm at small radii, to 10.2 mm × 10.2 mm at the largest radii, with the specific sizes chosen such that each pad subtended an approximately equal η range ($\Delta\eta \approx 0.1$) for collisions occurring near the nominal interaction point ($z_{vtx} = 0$). The inner diameter of each Ring was 100 mm, extending 120 mm outward radially. The Rings and readout electronics were supported by carbon-fiber frames, to ensure that inactive material around the detectors was low-Z and would not induce a large source of secondary particles. The signal-to-noise ratio achieved for the Rings was similar to that for the Octagon. A diagram of a ring detector is shown in Fig. 2.3(b) [86].

2.2.2 Vertex Detectors

The design goal for the Vertex detector was to determine the vertex position with a precision of better than 0.2 mm in the z-direction for central collisions within 10 cm of the nominal interaction point. To achieve this goal, two sets of finely segmented silicon pad detectors were installed on the Octagon frame, above and below the beam line centered at $z = 0$. Each set was composed of two layers of silicon sensors, called the "Inner" and "Outer" Vertex detectors. Based on the hits in these two layer sensors, two-point tracklets were identified, which pointed back to the original collision vertex. The details of various vertex reconstruction algorithms will be discussed in Sect. 4.2. In addition, Vertex detectors could also be used to determine the charged particle multiplicity within the acceptance they covered.

The Inner Vertex detectors were located closer above and below the beam pipe (±56 mm in the vertical direction), consisting of two modules, each with two sensors. Each sensor was divided into 4 rows of 128 pads along the beam axis. The pads were 12 mm wide and 0.473 mm long, which gave similar granularity to the Octagon in the azimuthal direction but much greater precision in pseudorapidity. The layers further from the beam line (±118 mm in the vertical direction), known as the Outer Vertex, consisted of two rows of sensors, each row having four sensors placed side-by-side. Each of these sensors had a grid of 128 pads in the beam direction by 2 pads in the transverse direction. Pads in the Outer Vertex were 0.473 mm long and 24.070 mm wide. Sensors of the Vertex detector achieved an even better signal-to-noise ratio than those for the Octagon or Rings. The upper 4 x 2 array of the Outer Vertex sensors can be seen in Fig. 2.3 [86].

2.2.3 Spectrometer Arms

PHOBOS Spectrometers were built for track reconstruction and identification of about

2% of all the particles coming out of the collisions. Two spectrometer arms made of silicon pads were situated in a 2 T magnetic field. Particle momentum was determined from the curvature of particle's trajectory when traveling through the magnetic field. A Time-of-Flight (TOF) wall was installed further away from the beam pipe to obtain the velocity of the particles, in order to extend the capability of Particle Identification (PID) to higher momenta. Particle species at lower momentum range could be determined using the energy loss in the silicon pads of the Spectrometer arms.

PHOBOS Magnet

The PHOBOS magnet was a conventional room temperature magnet of a double dipole design with one dipole located on each side of the beam pipe, providing vertical fields of opposite polarity in the two arms (see Fig. 2.4(a) [86]). The magnet pole gap was 158 mm with coils unenergized. When fully energized at a current of 3600 A, the magnet provided a total bending power of ~ 1.5 Tm and maximum $B_y = 2.18$ T. As illustrated in Fig. 2.4(b) [59], the magnet was designed in such a way that the first six Spectrometer layers sat in almost zero field, while the remaining layers were in a region of approximately constant field of $B_y \sim 2$ T, and B_x, B_z components of less than 0.05 T. The field strength was measured using a Hall probe at 15,120 nodal points, corresponding to a precision of about 150 mm in the PHOBOS coordinate system. During the operation, the magnet polarity was also reversed after each beam dump, to ensure similar statistics in both polarities. This was essential for minimizing systematic uncertainties, particularly in the analysis of particle ratios [87, 88].

Tracking Spectrometers

The PHOBOS Spectrometer consisted of two arms, located on opposite sides of the beam pipe. Each arm had 137 sensors and 780 readout chips assembled into 42 multi-sensor modules accommodating a total of 56,064 channels. The modules were mounted on 8 Aluminum water-cooled frames that were attached to a carrier plate as shown in Fig. 2.5 [89]. The carrier plates were fabricated from a non-conductive carbon-epoxy material to minimize vibrations caused by the ripple in the magnet current. The entire magnet gap between the two poles where the spectrometer resided in had a light and air tight enclosure. The enclosure was continually flushed with dry nitrogen to ensure that the relative humidity was $< 10\%$.

The Spectrometer contained five different types of silicon sensors, details of which

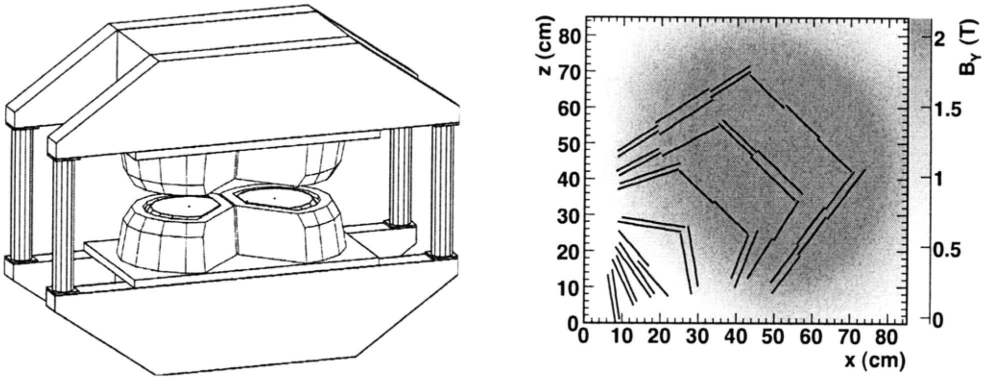

(a) PHOBOS Magnet

(b) Magnetic Field Map

Figure 2.4: (a) A picture of the PHOBOS magnet. The beam pipe goes through the center of the structure [86]. (b) The vertical magnetic field strength in the vicinity of one of the Spectrometer arms [59].

are given in Table 2.1. Sensors positioned closest to the interaction point were the most finely-grained sensors; in general, pad size increased as distance from the interaction became greater. However, the horizontal pad width was always kept small than the vertical dimension, in order to maintain good resolution in the bending direction of tracks. The spatial positioning of the Spectrometer layers and their respective sensor types are shown in Fig. 2.6 [20].

Sensor Type	Number of Pads (horiz. x vert.)	Pad Size (mm x mm)	Sensor Placement (layer numbers)
1	70 x 22	1.000 x 1.0	1-4
2	100 x 5	0.427 x 6.0	5-8
3	64 x 8	0.667 x 7.5	9-16 (inner)
4	64 x 4	0.667 x 15.0	9-12
5	64 x 4	0.667 x 19.0	13-16

Table 2.1: Properties of the various Spectrometer sensor types [90].

Time-of-Flight Wall

The Time-of-Flight (TOF) detectors were built to extend PHOBOS's PID capabilities further toward higher momenta, complimentary to the Spectrometers. There were two TOF walls installed, containing a total number of 120 scintillators per wall. Wall 'B' was

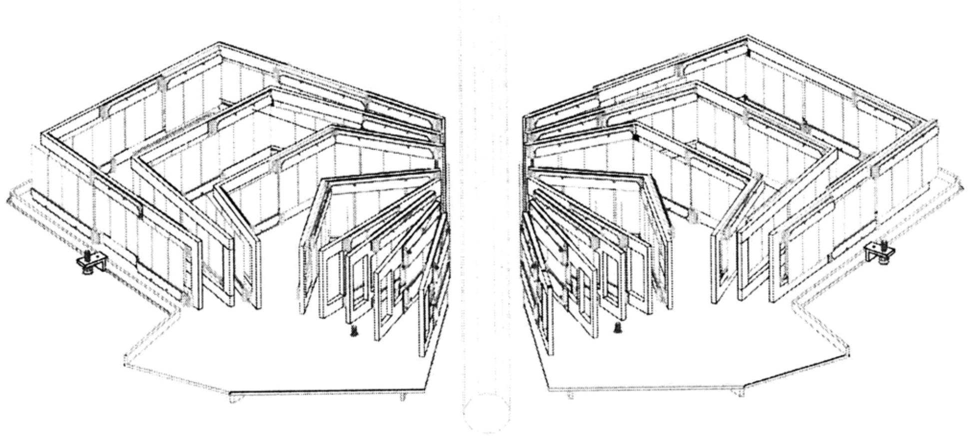

Figure 2.5: The PHOBOS multi-layer silicon two-arm Spectrometer [89].

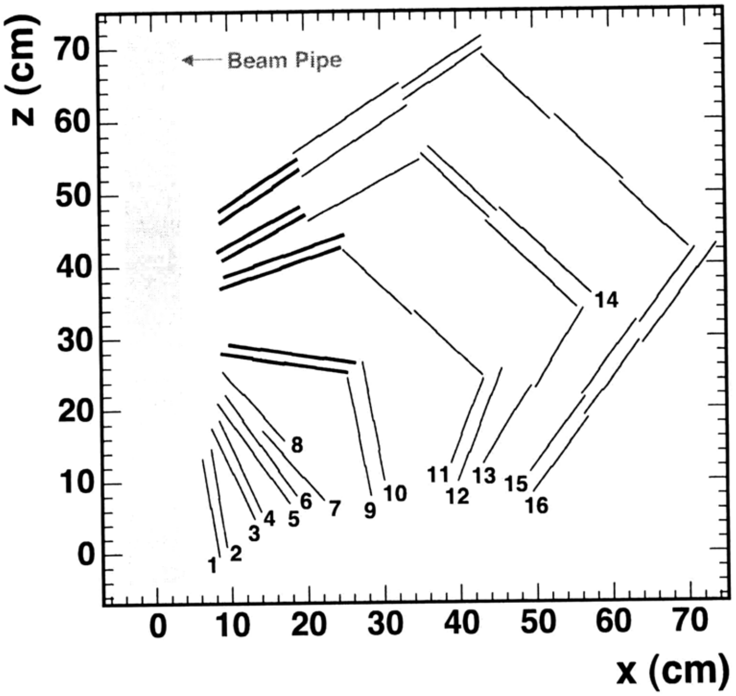

Figure 2.6: Layout of sensor layers for one PHOBOS Spectrometer arm in x-z place. The Type 3 sensors were indicated with thick lines [20].

placed at 45° relative to the beam-axis and 5.4 m from the origin, while wall 'C' was parallel to the beam-axis at a distance of 3.9 m from the origin. The length of each wall was

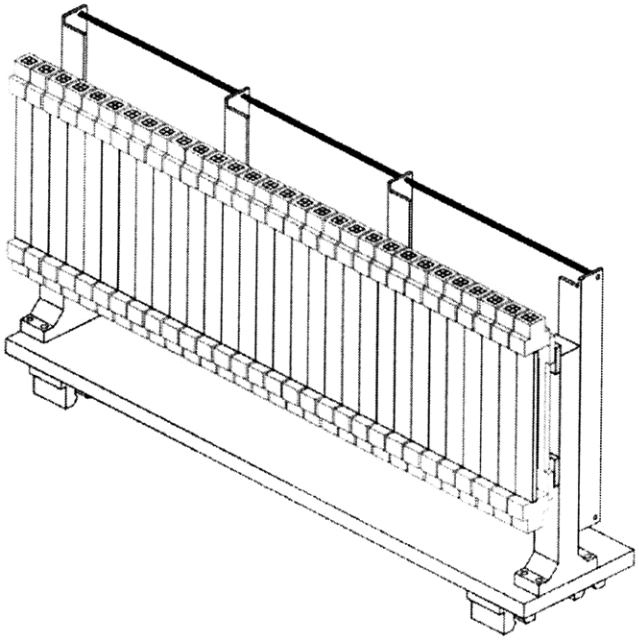

Figure 2.7: Schematic drawing of one TOF wall [59].

1.1 m long, spanning a pseudorapidity range of $0 \leq \eta \leq 1.24$.

The Bicron3 BC404 plastic scintillator was used in the construction of the TOF wall by virtue of its a good timing resolution (decay constant $\tau \sim 1.8$ ns) and a moderate attenuation length (1.6 m). Also, its maximum emission wavelength (408 nm) was close to the peak response wavelength (420 nm) of most fast Photomultiplier Tubes (PMTs). The scintillators were 200 mm high and had cross-sectional areas of 8×8 mm^2.

PMTs with fast rise time (1.8 ns) and high gain (1×10^6) (Hamamatsu R59004) were connected to the scintillators. The anode was segmented into 4 (2×2) channels per unit, which required a complex lightguide geometry and mounting fixture (see Fig. 2.7). Two PMTs were coupled via light guides to each end of four scintillators. The anode signals from PMTs were split into two components. One went into a Analog-to-Digital Converter (ADC) module after a 400 ns delay and the other was connected to a leading-edge discriminator, located close to the PMTs. The discriminator output signals from the module were then digitized using Time-to-Digital Converter (TDC) operated with a sensitivity of 25 ps/channel.

Simultaneous measurements of the time and pulse height allowed slewing corrections to be made, which achieved a measured time-of-flight resolution of approximately 75 ps (1σ) using sources and cosmic ray tests.

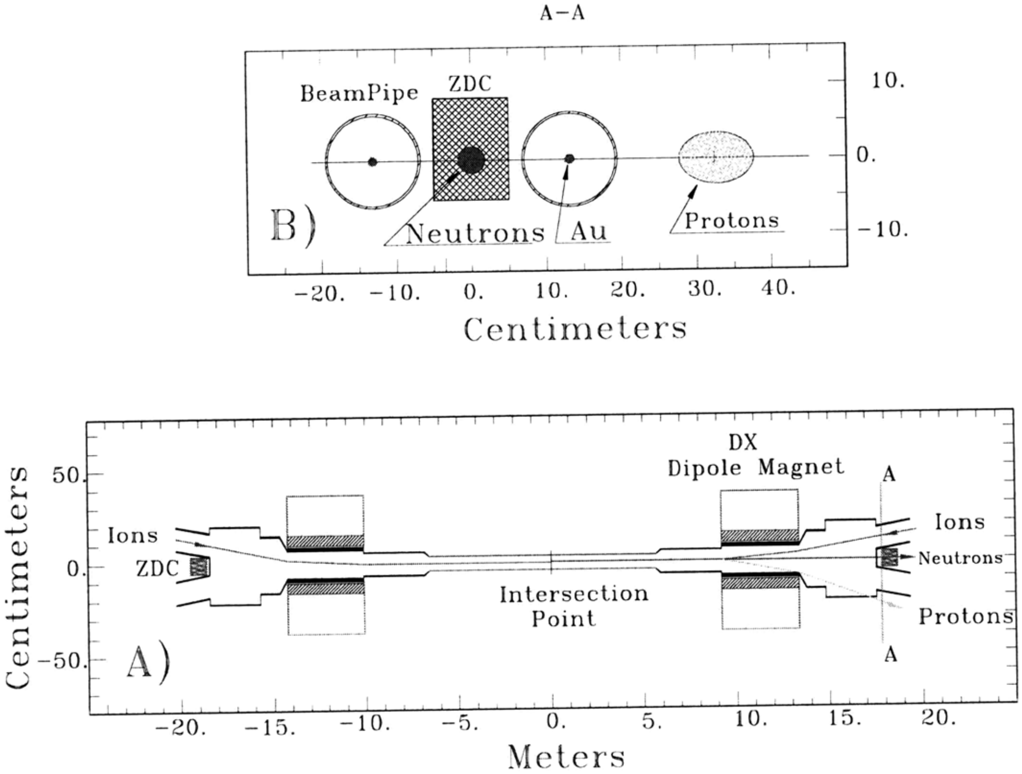

Figure 2.8: Plan view (bottom) and "beam's eye" view (top) of the ZDC location and the paths taken by gold ions, protons, and neutrons [91].

2.2.4 Calorimeters

Calorimeters at PHOBOS mainly included Zero-degree and Proton Calorimeters, located further away from the interaction point downstream of the beam pipe. They were used to detect the energy of forward going neutrons and protons respectively, most of which were broken up from the initial nucleus and thus did not participate in the reactions, known as "spectators". This was essential for the impact parameter determination of a collision, especially for studying the system size dependence of some physical observables.

Zero-degree Calorimeters

"Non-central" high energy collisions of nuclei usually led to the emission of free neutrons (those not bound in a nuclear fragment such as alpha particles) from both beam and target nuclei. Such evaporative neutrons emerged with near-beam rapidity and could be detected using a hadron calorimeter placed at "zero degree" region downstream of a collision. Although possibly affected by the breakup of the nucleus, the trajectories of these neutrons only diverged by less than 2 mrad from the beam axis at the RHIC energy of 100 GeV/nucleon.

The ZDCs were placed after the DX magnets where the two RHIC accelerator beam tubes separated at ±18.5 m from z=0. This region was ideally suited for exclusive measurement of free neutrons, since all charged particles were swept away by the DX magnets. A width of 10 cm (limited by transverse space in the "zero-degree" region) covered a deflection angle of about 2.7 mrad. See Fig. 2.8 [91] for a schematic of the ZDC positioning and the paths taken by charged particles through the DX magnets.

Each ZDC consisted of three modules made of sandwiches of 27 tungsten plates (5 mm thick) and ribbons of 20 commercial grade optical fibers (0.5 mm in diameter) which sampled the Čerenkov light ($2\lambda_I$, $50X_0$). Three modules were placed behind each other in order to collect about 98% of the neutral energy. Each module was attached to a PMT to collect the Čerenkov light from all the fibers. An orientation of 45° was chosen for the tungsten plates, which roughly coincided with the Čerenkov angle of light emitted by particles of $\beta \approx 1$ in the fibers. The energy resolution of the full ZDC set (3 modules) was found to be $\sigma_E/E \leq 20\%$ and the timing resolution was found to be better than 200 ps, which was sufficient to be used for minimum bias event trigger. A diagram of the ZDC construction is shown in Fig. 2.9 [91].

Proton Calorimeters

Adjacent to the ZDCs, in the region where protons were swept out of the beam pipe, forward Proton Calorimeter (PCAL) detectors were installed during the d+Au run to tag collisions with "proton spectators". The PCALs were constructed using lead-scintillator hadronic calorimeter modules, each comprised of a lead-scintillator brick that was 117.0 cm long with a square cross-section of 10×10 cm^2 on each side, and an array of 47×47 scintillator fibers. The construction procedure of lead-scintillator bricks required great care. Thin sheets of lead (with a 1% antimony admixture) were rolled through a grooving machine and laminated. A ribbon of 47 scintillator fibers was then inserted into the grooves. It took the process 46 times to complete a module. Attached to the brick section was an ultra-violet absorbing Lucite light guide, which ensured clean transmission of scintillation light ($\lambda = 435$ nm) without contamination from any Čerenkov radiation created in the light guide. See Fig. 2.10 [92] for a diagram of a PCAL module. A full description of PCAL can be found in [20].

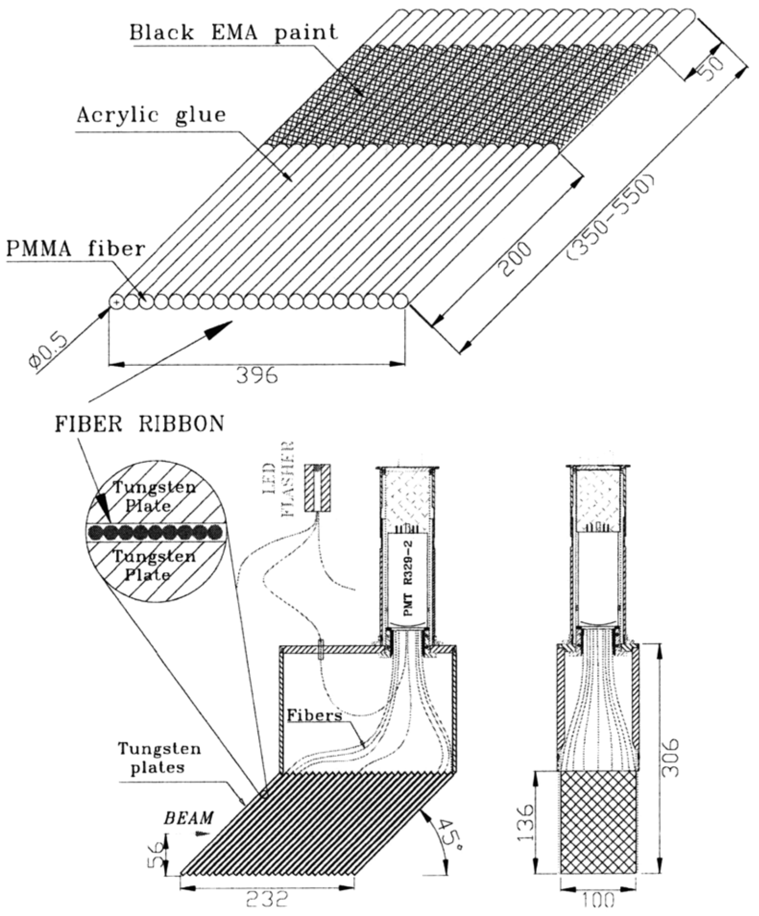

Figure 2.9: Design of a tungsten ZDC module. Dimensions shown are in millimeters [91].

2.2.5 Triggering System

The PHOBOS triggering system has three main components:

- The Paddle counters, which served as the primary Minimum Bias (MinBias) event trigger for high multiplicity Au+Au collisions;
- The Time-Zero Counters (T0s) were used to provide triggers with more accurate vertex position, and also a start-time for the TOF wall;
- The ZDCs, already described in Sect. 2.2.4, provided an experiment independent event trigger, which was useful for cross-correlating the results of different experiments.

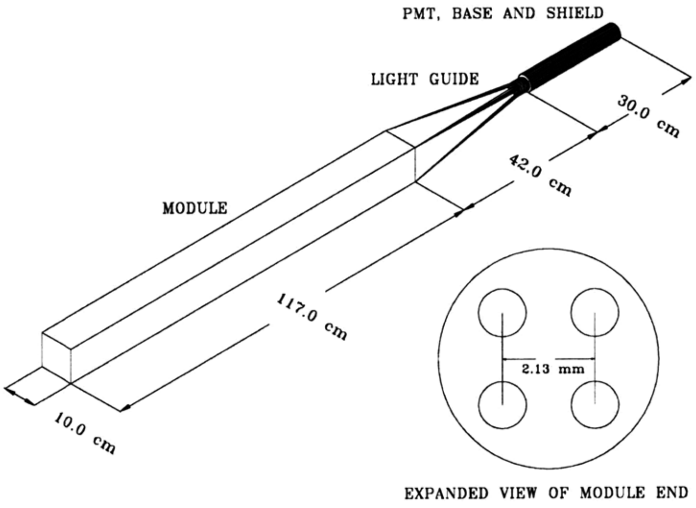

Figure 2.10: Design of a PCAL module. The inset shows the spacing of scintillator fibers [92].

Additionally, the Spectrometer Trigger (SpecTrig) counters were installed between TOF wall and the Spectrometers right before 2003 d+Au run, in order to access more events with high p_T particles. There were Čerenkov counters, two sets of 16 Lucite radiators arranged around the beam pipe at ±5.5 m. However, they were replaced by the T0s with much better precision and no longer used after the d+Au run.

Paddle Counters

The Paddle counters [93] were most efficient in triggering on collisions at high multiplicity environment like Au+Au and Cu+Cu. Paddles were made of two planar arrays of 16 wedge-shaped scintillators, perpendicularly surrounding the beam pipe at z=±3.21 m from the nominal interaction point. They subtended the pseudorapidity range $3 < |\eta| < 4.5$, with an active area of 99%. Trigger requirements based on the number of scintillators that had been fired and the total energy deposited in each array. Plastic scintillator had the advantage of good timing resolution ($\sim$ 150 ps). Large dynamic energy range (from one Minimum Ionizing Particle (MIP) up to 50 per collision) also provided a flexible event trigger that could be used to determine the event centrality (See Sect. 4.4). A diagram of a Paddle counter is shown in Fig. 2.11(a) [93].

The individual scintillator was made of BC-400 plastic, 18.6 cm in length, 0.95 cm thick, and extending from 1.9 cm long at the inner edge to 9.5 cm at the outer edge. As shown in Fig. 2.11(a) [93], the Paddle plane was oriented transverse to the beam pipe,

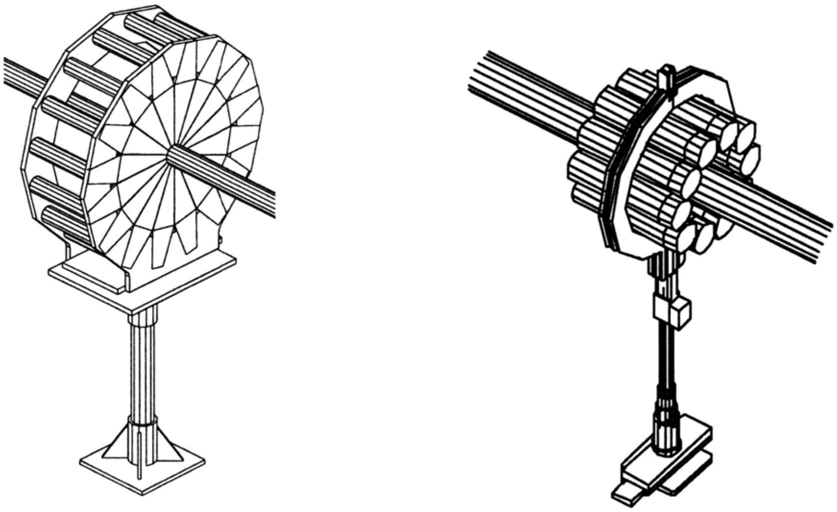
(a) Paddle Counter (b) Time-Zero Counter (T0)

Figure 2.11: Schematic diagrams of trigger counters: (a) Paddle Counter [93] and (b) Time-Zero Counter (T0).

while the PMTs were arranged longitudinally. To realize this layout, a two-component acrylic light guide was implemented, one that coupled to the scintillator and the other to the phototube. Light was reflected by a 45° Aluminized mirror through the 90° angle, transported from one component to the other.

The full Paddle counters performed with a trigger efficiency of 100% from semi-peripheral to most central event. This provided a perfect unbiased event trigger on all the collisions. Using the time difference between the two Paddle planes, a time resolution of about 1 ns was sufficient to distinguish between collision and background events that were close to the PHOBOS nominal interaction point.

Time-Zero Counters

The T0s were built in replacement of the original Čerenkov counters in order to provide more precise start-time measurement for the TOF, as well as real-time vertex information for use in triggering. There were two T0s, each consisting of 10 modules arranged in a circle of 151 mm in diameter about the beam pipe. They were located 5.4 m away from the interaction point but not always fixed. For example, during the d+Au run, one of the T0s was moved to 2.6 m from the interaction point on the deuteron exit-side of the collision. For p+p collisions, both modules could be moved much closer to each other.

The Čerenkov radiators (Bicron BC800) were still used for the T0s. However, the PMTs (Hamamatsu R2083) used for T0s were adapted to have a rise time two times faster than those used for the Čerenkov counters. This feature provided an intrinsic time resolution of 110 ps, significantly improved the timing information of the collisions. Nevertheless, their geometrical acceptance became smaller, resulting in some loss of efficiency for very peripheral or low multiplicity events. A diagram of one T0 Counter is shown in Fig. 2.11(b).

2.2.6 Data Acquisition

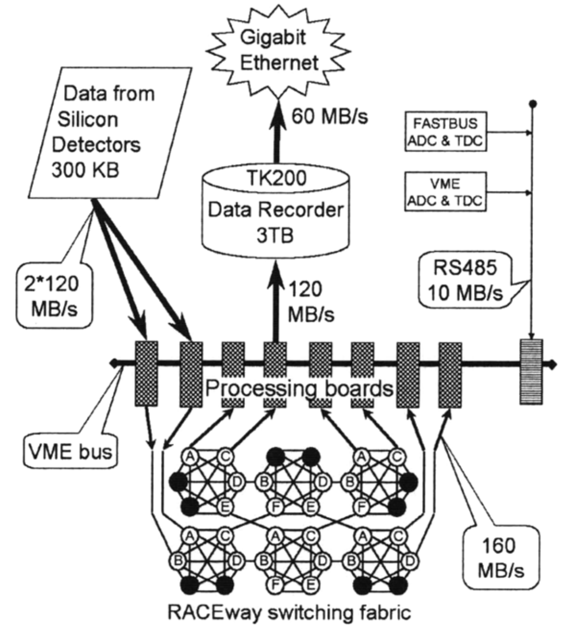

Figure 2.12: Diagram of the PHOBOS Data Acquisition (DAQ) system from [94].

The PHOBOS Data Acquisition (DAQ) was capable of accepting data from 135,000 silicon and 1500 scintillation detector channels at an event rate of over 200 Hz, and transferring the data over a Gigabit network to the RHIC central data storage system at a sustained rate of 30 MB/s. The DAQ resided in a VERSAmodule Eurocard (VME) crate. It comprised of 24 300 MHz PowerPC-750 CPU farm, a computer module to assemble the processed data into an event (event builder), a disk array for temporary data storage, a module to monitor trigger signals and a server to ship the processed data to tape storage. The various parts of the PHOBOS DAQ system are shown in Fig. 2.12 [94].

A decision would be made regarding whether or not to record an event to disk using digitized signals from the trigger detectors. A description of the digitization process for silicon signals can be found in Sect. 3.2. Details of various triggering algorithms are described in Sect. 4.1. A significant portion of the CPU farm was devoted to processing the raw data to achieve Common-Mode Noise (CMN) corrections and zero suppression, and also compress the silicon data to preserve empty channels for later offline corrections. The compression procedure utilized lossless Huffman compression algorithm, which encoded the most frequently occurring ADC samples into short bit patterns. A compression factor of 3-4 was achieved for Au+Au collision data.

The digitized signals from silicon detectors combined the signals from the scintillators, which were digitized in one FASTBUS crate (Paddles, TOF, TOs, ZDCs) and one VME crate (PCAL, SpecTrig). They were then sent to the event builder through a Front Panel Data Port (FPDP) connection at a rate of 43 MB/s. The event was then stored in memory until it could be written to the disk cache. Sequences of roughly 10,000 events were generated in the format of ROOT files of $\sim$ 1 GB in size, and then transfered to the High Performance Storage System (HPSS) at RHIC over a Gigabit Ethernet connection at a rate of 30 MB/s, as mentioned earlier.

2.2.7 PHOBOS Computing Architecture

The RHIC Computing Facility (RCF) [95] supplied computing resources to all four experiments at RHIC. All the raw data collected by the experiments were stored on a big HPSS tape storage system. A distributed and centralized disk storage farm was used for signal processing and event reconstruction of the raw data. At PHOBOS, the raw data were conveniently staged from HPSS onto the distributed disk via a web interface call CatWeb. Moreover, detector simulation and physics analysis work were carried out on the Linux Farms consisting of hundreds of computers, where the Condor batch system was installed for parallel job processing.

The PHOBOS Analysis Toolkit (PhAT) software was developed based on the ROOT [96] object-oriented C++ framework, a common tool in the area of high-energy physics to handle enormous amount of data. PhAT implemented PHOBOS-specific classes and programs. PHOBOS Monte Carlo (PMC) simulated the detector responses using the popular GEANT software [97] for correcting the detector effects. The Analysis Trees (AnT) in PHOBOS was designed based on `TTree` class of the ROOT, to provide improvements in data storage and processing efficiency over the standard ROOT file Input/Output (I/O). Tree-Analysis Modules (TAM) provided the infrastructure for data processing using *modules*. An analysis job was accomplished by using a hierarchy of *modules*, each of which was designated for a particular task. In this way, it is more efficient for maintaining the analysis tools and sharing the resources among the collaborators.

3 Silicon Detector Calibration

The semiconductor (silicon) technology was widely applied in the PHOBOS detector. Once the raw signals had been recorded in the silicon detectors, several steps were still required to determine the positions and deposited energies of the charged particles. This signal processing included pedestals and Common-Mode Noise (CMN) corrections, the gain calibrations, and the determination of dead channels.

3.1 Principle of Semiconductor Detector

Semiconductor detectors are popular in high energy physics due to their unmatched energy and spatial resolution as well as an excellent response time.

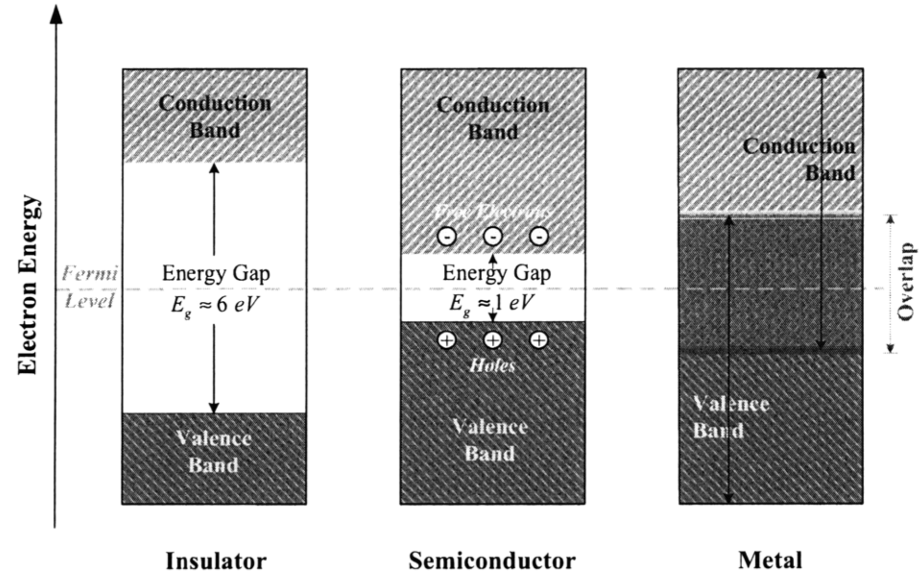

Figure 3.1: Energy band structure of conductors, insulators and semiconductors.

A semiconductor such as silicon (Si) or germanium (Ge) is a solid state material that has electrical conductivity in between a conductor and an insulator. Its energy gap between the valence band and the conduction band is relatively small (~ a few eV). Valence electrons are easily excited into the conduction band at sufficient high temperature via thermal energy, leaving behind a "hole" in the valence band (see Fig. 3.1). The mobility of electrons and holes can be enhanced by doping the pure semiconductor with impurities. If the impurity contains more valence electrons than Si or Ge, then this semiconductor is called *n-type*, whose dominant charge carrier is negative. On the other hand, the semiconductor is called *p-type* if the impurity has less valence electrons and produces more positive charged holes. These charge carriers can move under the influence of an external electric field, and generate electric current.

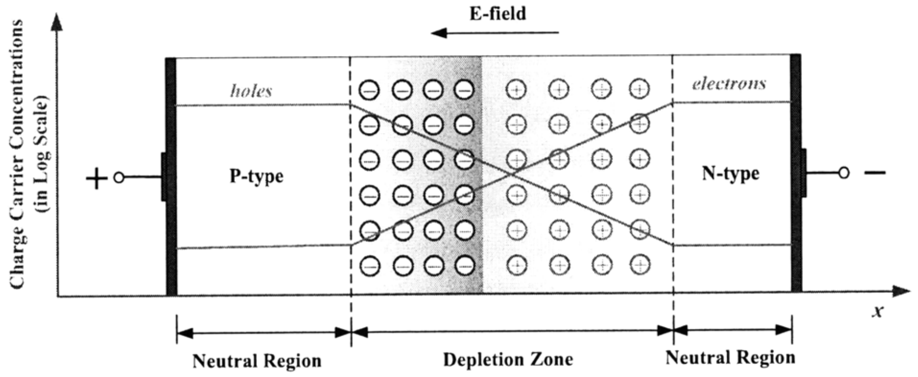

Figure 3.2: A *p-n junction* with reverse bias voltage applied. Electrons and holes concentration were represented with blue and red lines respectively. In the depletion zone,light red area is positively charged, while light blue area is negatively charged.

A *p-n junction* is formed by combining p-type and n-type semiconductor together in intimate contact. Initially, the density of electrons at n-doped side is higher. They will diffuse into p-doped side to recombine with holes (and vice verse for holes from the p-doped side) to reach the equilibrium. As a result, a "depletion zone" (also called "space charge region") is formed, which has the special property of being devoid of all mobile charge carriers. This is illustrated in Fig. 3.2. The depletion zone is the sensitive area of the silicon detector. Its volume can be increased by applying a reverse-bias voltage (a positive voltage to the n-type and a negative voltage to the p-type).

When an ionizing charged particle passes through the sensitive area, electron-hole pairs are liberated along its track and then swept out by the electric field. Electrons drift towards the anode, holes to the cathode. An electric current signal will be detected by the electrodes (charge collection), which is proportional to the ionization number, thus the energy loss of the particle. Since it takes less energy to produce electron-hole pairs in a semiconductor than it does to ionize a gas (tens of eV), silicon detectors produce a larger number of charge carriers than a gas-ionization detector, and hence have better energy resolution. Its fast charge collection also features it an excellent timing resolution. For more information on semiconductor detectors, see Ref. [98].

3.2 The PHOBOS Silicon Sensor — Design and Readout

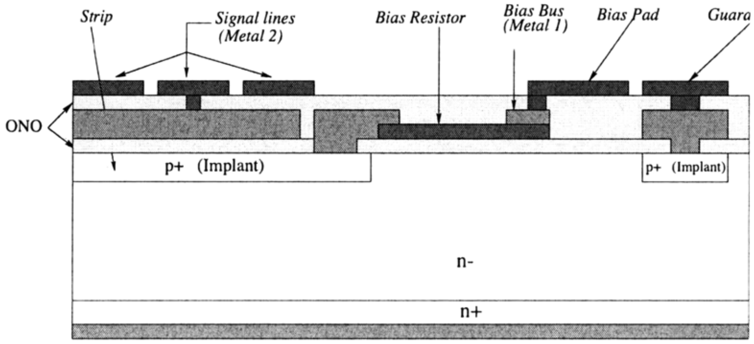

Figure 3.3: Cross-section of a silicon sensor used in PHOBOS [99].

A schematic diagram of the cross section of one PHOBOS silicon pad is presented in Fig. 3.3. The silicon sensors [99] were constructed using a $\sim 300\ \mu$m thick n-type silicon layer, with rectangular p+ implants (providing two-dimension information) heavily doped to create the p-n junction. A reverse-bias voltage of 70 V was applied via a 5.5 ± 0.2 MΩ polysilicon resistors (red), the resistance of which was required to be at least 1 MΩ. AC-coupling design was used, where the implant layer and the first metal layer (green), made of aluminum, were coupled by a capacitor formed by a 0.2 μm thick layer of silicon Oxide-Nitrous-Oxide (ONO) material (yellow). Each pad from this array was read out by a second metal line (blue) that ran along the surface of the sensor to a common bonding pad where the front-end electronics were attached at the edge of the sensor. The design of double metal layer had the advantage that the readout structure was integrated on the sensor so that the full sensor surface could be used for routing the signals.

All PHOBOS silicon detectors used VA-HDR-1 chips (64- or 128- channel version depending on the sensor granularity) as the readout, manufactured by the IDEAS company (http://www.ideas.no) and commercially available. These chips were mounted

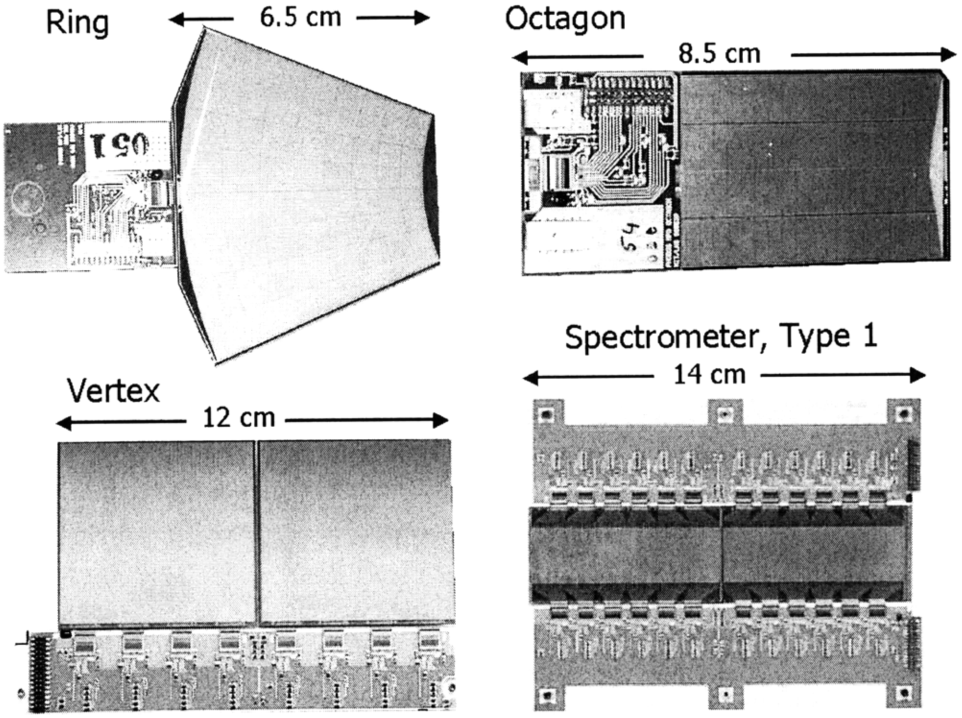

Figure 3.4: Photographs of four types of silicon sensor module.

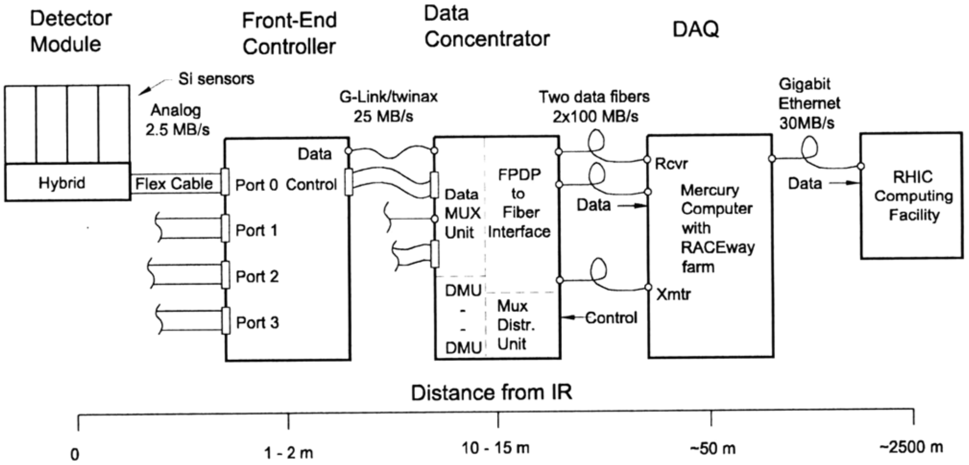

Figure 3.5: Diagram of the PHOBOS silicon detector readout architecture [100].

on a hybrid with chip inputs directly wire-bonded to the sensors. Photographs of silicon sensor modules from various PHOBOS sub-detectors are shown in Fig. 3.4. The pre-amplified signals from the readout chips were digitized by 12-bit ADCs in the Front-End Controllers (FECs). The digitized signals from each FEC was then sent via G-link interface to the Data Multiplexing Unit (DMU) in the Data Concentrator, where they were collated into serial streams and transmitted over optical fibers to the DAQ system (see Sect. 2.2.6) in the PHOBOS Counting House. Fig. 3.5 [100] summarized the full readout architecture. For further details of the PHOBOS detector readout, see Ref. [100].

3.3 Pedestal, Noise and Energy Calibrations

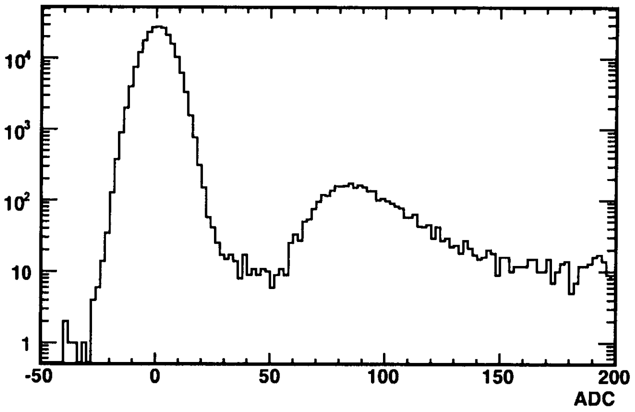

Figure 3.6: ADC signal distribution from a typical Ring sensor after subtracting the Pedestal [90]. The peak at 40 ADC units is associated with the 80 KeV deposited by the Minimum Ionizing Particles (MIPs), while the width of the peak centered at zero corresponds to the noise background.

Pedestal, Noise Corrections

The "leakage current" in semiconductor devices will contribute to the ADC signals as a non-zero offset even in the absence of any true signal. This effect would result in a "pedestal" and need to be corrected for. For low multiplicity events where the detector occupancy was low, a given silicon channel would not always be hit by a real particle. Because of that, the signal was dominated by the pedestal. At the beginning of each run, the average signal from the first several hundred events were first calculated as the "pre-pedestal". Within a narrow range around the pre-pedestal, more events were processed to locate the peak value as the pedestal to be subtracted. If the peak-finding failed, more events were added until it was found. To determine the noise, the signals from next few hundred events were fitted with a Gaussian around the most probable value determined in the previous step. The noise value corresponded to the width of the Gaussian centered at zero in Fig. 3.6.

In addition to the pedestal contribution, the voltage applied to a given chip could also shift up and down randomly. This will produce collective fluctuations on all the channels lying on it, called the Common-Mode Noise (CMN). A CMN shift could be caused by a sink in the supply voltage of a whole chip due to very large current consumption in a few channels with a large signal. To correct for CMN, the pedestal-subtracted signals were collected for groups of channels event-by-event. Any non-zero offset in the single-event pedestal-subtracted signal distribution was attributed to CMN. Therefore, the corrected signal is defined by: Corrected Signal = ADC - Pedestal - CMN.

Energy Calibrations

To convert ADC units to the actual energy deposited, a gain calibration system was used in dedicated calibration runs. A sequence of known Digital-to-Analog Converter (DAC) signals was first sent to the front-end pre-amplifiers and digitized. The output ADC signals were then compared to the input DAC signals. Finally, it was found that one ADC channel was associated with 2.1 KeV deposited energy, which corresponds to a most probably hit value (MIP peak) of 80 KeV.

After calibration, the silicon signals underwent further zero-suppression. Pixels with very low energy signals (less than 10% of the MIP value) were simply negelected and set to zero value. This considerably reduced the event size and saved large amount of storage space.

3.4 Dead and Hot Channel Corrections

Silicon channels that were not functioning properly needed to be identified and excluded in further physics analysis. These "dead" channels were determined primarily based on two criteria: the number of hits each channel received above a certain threshold, and the energy associated with each hit. After averaging over many events until each silicon channel got sufficient number of hits, those had much fewer hits or less energy per hit compared to the average were considered dead. At the other extreme, for channels having too many hits or very large energy per hit, they were considered as "hot" channels and also rejected, since they might manifest large non-statistical fluctuations and be very noisy. A map of the dead (red) and hot (green) channels in the Octagon for the 2005 PHOBOS physics run is illustrated in Fig. 3.7. About 8% of the silicon channels in the Octagon were either dead or too hot. More details about determining the "dead channel map" can be found in Ref. [90].

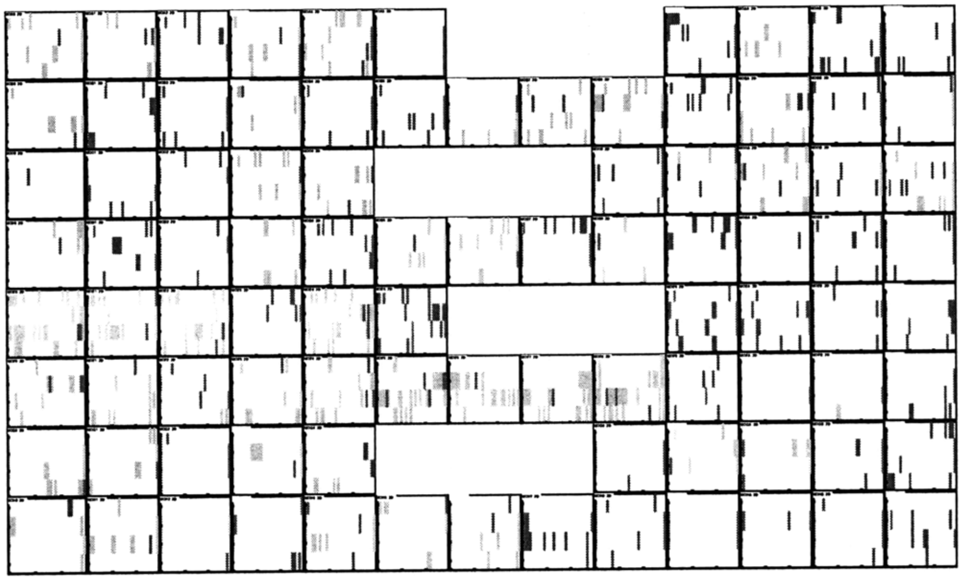

Figure 3.7: The distribution of dead (red) and hot (green) channels in the Octagon detector for the 2005 PHOBOS Cu+Cu run.

4 Event Characterization

Once the signals in various detectors were read out and processed, the characteristics of events could be reconstructed, in particular the collision vertex position and geometry. During the data taking, fast detectors were used to trigger on collision events and record them on tape. Offline selection was also performed to further reject backgrounds.

4.1 Collision Trigger

Event triggering have been playing an indispensable role in the experiments of high energy physics all along. Due to the short-range nature of interactions between the elementary particles, an event of real collision only happens once in a while although bunches of particles keep passing through each others. A decision needs to be made in whether or not record the signals of an event. Moreover, to study a particular process of interest which is usually rare, online event selection is crucial to reach sufficient statistical significance.

At RHIC accelerator, a crossing-clock was set up in order to inform the experiments when two counter-rotating beams cross each other and might produce a collision. However, this would result in mostly collisions between ions in the beam and residual gas molecules in the beam-pipe. PHOBOS experiment made use of its T0 and Paddle detectors to provide primary triggering on the real nucleus-nucleus collisions. Several types of triggering configurations were deployed in PHOBOS [101], mainly including Minimum Bias (MinBias) triggers and Vertex triggers used by the analysis presented in this thesis. A Spectrometer Trigger (SpecTrig) was designed during the d+Au run to enhance events with high p_T tracks. Details of this trigger were discussed in Ref. [89].

4.1.1 MinBias Triggering

The goal of MinBias triggers is to capture as large fraction of the total cross-section as possible, with minimal bias and losses. The PHOBOS Paddle counters were primarily used for MinBias triggers due to its relatively large acceptance. This was particularly important for triggering efficiency in the low multiplicity environment, such as 200 GeV and 410 GeV p+p collisions analyzed in this thesis, where the trigger condition required that at least one slat in each of the positive and negative Paddles was fired. For higher multiplicity systems like Cu+Cu and Au+Au collisions, two or more slats in each Paddle were required to be hit. However, only a small sample of MinBias triggered A+A events were taken primarily for multiplicity analysis, since more restrictive and precise trigger conditions could be applied to better constrain the vertex position and suppress the backgrounds events.

4.1.2 Vertex Triggering

Large sample of 200 GeV Cu+Cu (2005) and Au+Au (2004) data were collected with the Vertex triggers. Vertex triggers aimed to select events lying within the usable region of detector. The time difference between signals in two sets of T0 counters passing through a Time-to-Analog Converter (TAC) was used to select collisions that were close to the nominal vertex position along the beam-axis (i.e. $|z_{vtx}| < 10$ cm). The T0s had a much better timing resolution than the Paddles counters (about an order of magnitude), although a smaller acceptance. For the 2004 Au+Au run, the vertex window was adjusted to extend widely and asymmetric for purpose of particular analyses (i.e. ϕ meson reconstruction).

During the Au+Au and Cu+Cu runs in 2004 and 2005, a cloud of desorbed electrons were formed in the beam as a results of the increasing luminosity and interactions of lost beam particles with the beam pipe [102]. Consequently, the abundance of double beam-gas ($\mathrm{Au}^+ + \mathrm{e}^-$) events would appear as good events falling in the desired vertex range, thus invalidate the existing triggers. Under such circumstance, the ZDC information was incorporated in the triggers to counteract this effect. Imposing on energy deposited coincidentally in both sides of ZDCs ensured that at least one heavy ion collision happened in the event. Inevitably, a larger fraction of pile-up events (more than one collision at a time) had to be discarded by offline selections later.

4.2 Vertex Reconstruction

The angular (η,ϕ) information of a charged particle was calculated by the hit position in the detector relative to the event vertex. Therefore, determining collision vertex was a critical first step for the interpretation of the observed signals. It was also used as a starting point for the reconstruction of track candidates [90]. A number of algorithms were designed to find the event vertex, utilizing various subdetectors which had their own advantages in certain aspect of vertex reconstruction. For example, vertex determined by the time difference between the two Paddle counters normally provided quite a poor resolution (~ 15 cm), but larger vertex range and high efficiency.

Vertex reconstruction methods were classified into two categories: track-based and hit-based methods. Track-based method utilized the “tracklets” reconstructed from the Spectrometer or two-layer vertex detectors (inner and outer). It gave a good vertex resolution but only applicable in high multiplicity environment due to the small acceptance of the tracking detectors. On the other hand, for relatively low multiplicity events, different vertexing techniques were adopted. In such conditions, vertex was usually reconstructed using all the available hits in the single-layer Octagon detector.

4.2.1 Low Multiplicity — OctDeVertex and OctProbMultVertex

The OctDeVertex algorithm was initially designed for p+p and d+Au collisions using hits in the single-layer Octagon detector. A newer and more complicated method, OctProbMultVertex, was developed during 2005 Cu+Cu run to further enhance the vertexing performance.

OctDeVertex

The basic idea of OctDeVertex was to make use of the position and deposited energy of all the hits in the Octagon to achieve a good efficiency and reasonable resolution down to very low event multiplicity. Due to the coarse granularity of the Octagon in ϕ direction, only the location of a collision along the beam axis (z direction) was obtained. The determination of x and y components relied on the Spectrometer and Vertex detector at higher multiplicity.

As described in Sect. 3, when particles transverse a silicon pad, a common amount of energy per unit path length is normally deposited (MIP). If a particle passes through the silicon at an oblique angle, it registers a larger amount of energy in a couple of adjacent pads, which is proportional to the length of the trajectory in the silicon. In the OctDeVertex algorithm, the energy from three adjacent pads in a row along the beam direction was first combined with hit energies each above 0.4 MIP (three times the typical noise level) and together above 0.6 MIP. The position of the resulting merged hit was

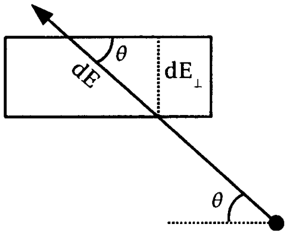

Figure 4.1: Correcting the deposited energy (*dE*) for the incident angle (θ) of a particle coming from the vertex [20].

determined by the first pad that sat closest to the nominal interaction point ($z_{vtx} = 0$). In the next step, for a chosen set of test vertex in z direction, the deposited energy of each merged Octagon hit corrected for the path length through the silicon was calculated, as illustrated in Fig. 4.1:

$$dE_{\perp} = dE\sin(\theta) = \frac{dE}{\cosh\eta} \tag{4.1}$$

where dE is the total deposited energy of the merged hit, θ is the polar angle with respect to the collision vertex. $dE_{\perp}$ represents the amount of energy left by a normal incident particle. Number of hits with angle-corrected energy between 70 KeV and 110 KeV was calculated as a function of test vertex. The true vertex corresponded to the maximum number of MIP hits (peak location), since wrong trial vertex would either over or under-correct the effect of incident angle, resulting in angle-corrected energy loss deviated away from the MIP peak. The longitudinal vertex position resolution of the OctDeVetex is about 1.5 cm for p+p events. More details of this vertexing algorithm can be found in Ref. [20, 101].

OctProbMultVertex

In Octagon Probability Multiplicity (OctProbMult) Vertexing procedure, at the initial step, the clustering of three adjacent pads was still performed. For each cluster, the probability distribution of z_{vtx} is constructed as a function of the hit position and number of merged pads, $P(N_{merged}, z_{hit} - z_{vtx})$. Then, the triangular-shaped probability distributions for each cluster were added up together. A region of the probability distribution that exceeded a certain percentage of the maximum value (by default the value was 60%) is selected. The final vertex position was then determined by the maximum value in this

Vertex Algorithm	X-resolution (μm)	Y-resolution (μm)	Z-resolution (μm)
ZVertex	2424 ± 32	163 ± 1	85 ± 1
SpecMainVertex	585 ± 7	385 ± 5	593 ± 10
SpecVertex_SpecPN	219 ± 3	297 ± 3	271 ± 4
RMSSelVertex	238 ± 4	182 ± 2	81 ± 1

Table 4.1: The resolutions of different vertex reconstruction algorithms for all the three spacial components (x, y, z) estimated from MC simulations of central Au+Au events [103].

region. The resolution of OctProbMultVertex is similar to that of the OctDeVertex.

4.2.2 High Multiplicity — RMSSelVertex

In high multiplicity Au+Au events, the vertex were reconstructed by combining several different vertexing algorithms know as RMS-Selected (RMSSel) Vertex, each of which had the advantage of finding the collision vertex in a particular dimension. This achieved a precise determination of all three spacial components (3-D) of the collision vertex. A detailed description of RMSSel Vertex finding algorithm can be found in Ref. [103].

ZVertex

The z-component of the collision vertex was best determined by ZVertex, just as its name suggested, using the two-layer Vertex detector. The first step of this algorithm is similar to the OctProbMult Vertex. Merged hits were made by clustering adjacent pads with energy loss above a minimum threshold on both layers of the Vertex detector. Then, by making all combination of tracklets from the hits in the Inner and Outer layers, and projecting back onto the $y = 0$ place, z coördinates were determined. Therefore, in the probability z distribution of these track segments, a peak value corresponds to the collision vertex position.

Similarly, projecting the tracklets onto $x = 0$ and $z = 0$ planes, the other two dimension of vertex position could also be obtained. However, the resolution was somewhat worse, especially for x coördinate due to the much larger pad size along the azimuthal direction (see Table 4.1). The systematics of ZVertex algorithm were checked between upper and lower hit pairs of the Vertex detector.

Track Intercept Algorithm: SpecMainVertex

The transverse location of the vertex was more precisely determined in the Spectrometer, using the straightline tracks constructed in the first several silicon layers. The main limitation of these algorithms was the low multiplicity due to the small phase-space coverage. Thus, they were only applicable in Au+Au collisions. The technique of track finding at PHOBOS can be found in [90].

The first method used the straight tracks that were constructed in the first four layers of the Spectrometer without constraint of the vertex. Pairs of tracks were made using all found tracks with χ^2 greater than 1%. Ones with a Distance of Closest Approach (DCA) in 3-D less than 0.4 cm were retained. The mid-point at nearest approach averaged over all such track pairs was considered as the vertex position. Each component of the vertex was separately obtained using this procedure.

True 3D Vertex Fit Algorithm: SpecVertex_SpecPN

The other Spectrometer-based vertex find algorithm that was incorporated in RMSSel Vertex also utilized straight tracks but outreached to the fifth and sixth layers. This time, the vertex position was determined in three-dimensions simultaneously using a MINUIT minimization of the DCA averaging over all selected straight tracks. This method was inevitably more computationally time-consuming than others. However, as shown in Table 4.1, it provided the best vertex reconstruction in three dimensions.

4.3 Event Selection

With the data recorded on tape, further offline selections on events were still necessary for identifying the high quality events and getting rid of undesirable backgrounds. The details of event selection criteria for each dataset used in this analysis is summarized in Table 7.1. The same cuts were also applied in the selection of MC events, except that the timing (Paddles, T0s and ZDCs) and pile-up cuts were not needed since beam-gas or pile-up events were not simulated in the MC.

4.3.1 p+p Event Selection

A clean selection of Non-Sigle-Diffractive (NSD) events was aimed for the study of inclusive observables, e.g. two-particle correlations, in p+p collisions. Both arms of the

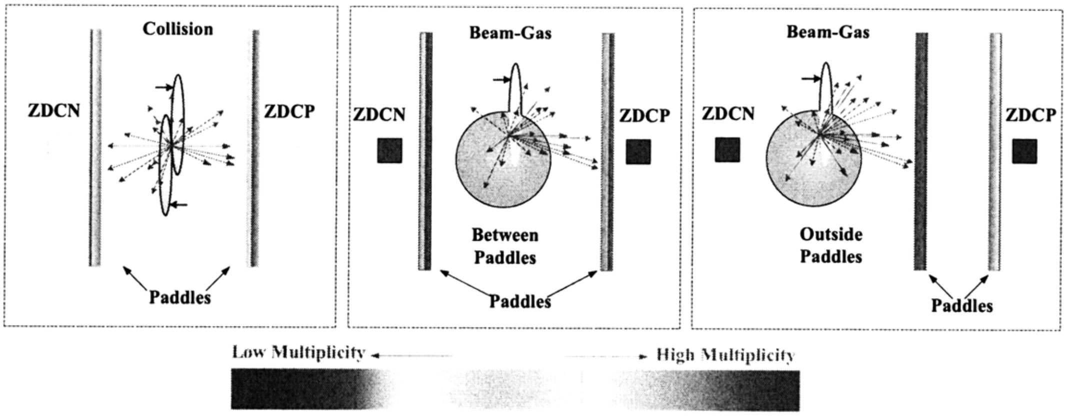

Figure 4.2: Schematic view of collisions and beam-gas interactions. A real nucleus-nucleus collision is illustrated in the left panel. Middle panel shows a beam-gas event happening between the two Paddle counters, while the case outside the two Paddles is displayed on the right.

Paddle counters were required to have at least one slat struck. In addition, since T0s were not used in the p+p minbias triggers (due to its small acceptance), a condition of Paddle Time Difference (PdlTDiff) between the positive and negative side less than 10 ns can better constrain the vertex range (described later in Sect. 4.3.2).

4.3.2 Cu+Cu Event Selection

Even after events had passed the trigger conditions described in Sect. 4.1, additional cuts were made to ensure the rejection of beam-gas events in favor of true nucleus-nucleus collisions. PHOBOS used a standard flag, called "Is Collision (IsCol)", to label if an event was a collision or not. It normally incorporated a list of cut conditions. During the Cu+Cu run, the standard IsCol selection, however, was not finalized until data processing had begun. For this reason, many trigger bits were set manually in the analysis of Cu+Cu data (see Table 7.1).

The goal of offline event selection was largely to reject beam-gas events by cutting on the PdlTDiff timing. Beam-gas events that happened outside the region between two Paddles would typically produce a longer time difference compared to the collisions in the center (see Fig. 4.2). For a relativistic particle traveling a distance of 6.4 m, it took about ±21 ns corresponding to the two peaks on the side, as seen in Fig. 4.3. PdlTDiff was required to be less than 5.0 ns, which selected collisions from the central part of the detector (75 cm), rejecting beam-gas events outside the Paddle region. Meanwhile, to

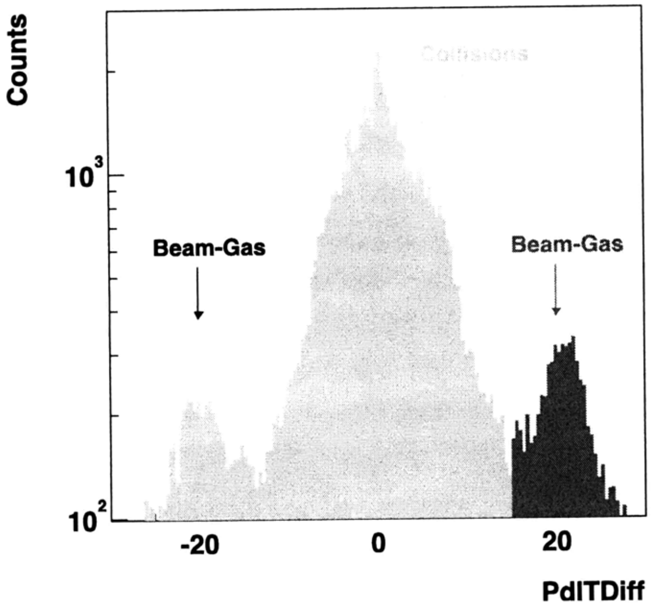

Figure 4.3: The distribution of Paddle Time Difference (PdlTDiff) shows a peak near zero, corresponding to collisions, as well as two peaks from beam-gas events at ±21 ns [101].

avoid recording signals from more than one collision, events were flagged "pre-pileup" if triggered less than 5 μs after another event, and similarly "post-pileup" if triggered less than 0.5 μs before another event. Finally, a good L1 timing required that when the previous event was rejected by the trigger logic, the fast clearing of the trigger signals had finished before the current event was recorded [101]. A valid reconstructed collision vertex was always required within the range of the Spectrometer acceptance ($-10 < z_{vtx} < 10$ cm) for building the tracks. Not only the OctProbMultVertex but also a valid OneTrackVertex was required as this vertex would serve as a seed in the track reconstruction procedure.

4.3.3 Au+Au Event Selection

Most of the offline event selections in Au+Au collisions were contained in the standard IsCol flag. This mainly included the cuts on the PdlTDiff and the ZDC timing.

Similarly to Cu+Cu, a sharp cut of ±4 ns on PdlTDiff was first placed to reject the beam-gas events occurring outside the Paddles. As in a beam-gas event, only Au ion broke up and liberated its spectator neutrons to be captured by the ZDC, only one side of the ZDCs was triggered since large amount of energy was required to fire the detector. Requiring a valid timing of both ZDCs excluded beam-gas events from between the Paddles that were not rejected by the PdlTDiff cuts. Finally, one additional cross-check was performed to avoid losing the central events. For very central events which created the most particles, only a few spectators were left, registering little signal in the ZDCs. A clear anti-correlation of signals between ZDCs and Paddles was observed [101]. If large signals were retained in both Paddles, events were allowed to fail the ZDC timing cut. The ZDC cuts were not used in Cu+Cu collisions largely because of much smaller number of spectator neutrons.

4.4 Centrality Determination

In a heavy ion collision event, two nuclei interact with each other at various impact parameters, b. Sometimes they are overlapped completely, while some other times only touched marginally. Collision centrality is a valuable parameter in relativistic heavy ion physics, which relates to the impact parameter of the collisions and number of participating nucleons.

It is essential to understand the initial conditions of two colliding nuclei for any study of the underlying physics (e.g. the initial geometric shape of the overlapping region is strongly correlated with the magnitude of observed elliptic flow). Experimentally, the centrality or impact parameter b of a collision is not a directly measurable quantity. However, by studying observables, such as multiplicity and spectator nucleons, that monotonically depends on it, events can be divided into different classes of collision centrality. PHOBOS utilized a multiplicity measurement to determine the fractional cross-section, $1-\sigma/\sigma_0$, or equivalently centrality, of a collision. Here, σ_0 represents the total inelastic cross section of Au+Au collisions and $\sigma = \int_0^b \frac{d\sigma}{db} db$. Furthermore, in the context of a Glauber Model (see Appendix C), the number of participating nucleons at given centrality can be estimated.

The centrality classification procedure at PHOBOS generally followed three basic steps:

- Correcting the trigger efficiency by comparing observed distributions in data and MC;
- Dividing the distribution of a multiplicity variable into bins of fractional cross-section;
- Using Glauber model calculation, connecting the bins of fractional cross-section

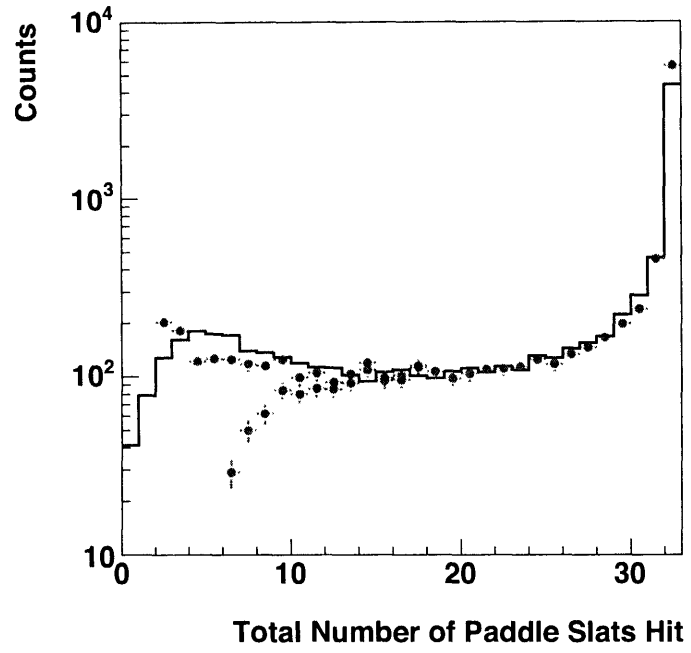

Figure 4.4: The distribution of the number of hit Paddles for HIJING (black line) and Au+Au data for the n>0 (red points) and n>2 (blue points) MinBias trigger requirements.

to the geometric variables such as impact parameter, number of participants and binary collisions.

A full description of the centrality determination procedures above including various systematic cross-checks can be found in [101].

4.4.1 Trigger Efficiency Correction

The first step of centrality determination is to estimate the trigger efficiency, in order to account for the fraction of events lost due to triggering and event selection requirements. This was performed by comparing the number of fired Paddle slats, ranging from 0 to 32, between data and HIJING sample as shown in Fig. 4.4. A plateau region between 15 and 22 hit slats emerged, which was used to normalize the distributions of data and MC. Once normalized, the efficiency was defined as the ratio of all events in data to the sum of data events with 16 to 32 hit slats and MC events with 0 to 15 hit slats.

$$\epsilon = \frac{N_{slat}^{Data}(0,32)}{N_{slat}^{MC}(0,15)+N_{slat}^{Data}(16,32)} \tag{4.2}$$

which said only in the low multiplicity region (fewer hit Paddle slats), the correction was applied to the data. This guaranteed that any discrepancy in the more central collision between data and MC, which might depend on the details of the HIJING MC would not affect the estimated fraction of missing cross-section for peripheral events. The final efficiencies for the 200 GeV Au+Au data were found to be 97% for n>0 slats hit and 88% for n>2 slats hit.

The strategy was not quite the same at lower multiplicity system like Cu+Cu collisions, since the normalization plateau of hit Paddle slats does not exist anymore. In this case, a 'shape-matching' technique was developed, that the shape of the distribution of a certain centrality variable (e.g. EOct) in MC was scaled to match that in the data at a high multiplicity region, where the event selection is close to 100%. The efficiency was then derived as the ratio of total integral of data to MC. This method was used in the d+Au Cu+Cu and low energy Au+Au runs. For 200 GeV Cu+Cu data, the final efficiency was (84 ± 5)% for the n>2 slats hit sample.

4.4.2 Fractional Cross-section Cuts

Once the trigger efficiency had been determined, fractional cross-section binning could be made with a multiplicity variable, that was required to be monotonically dependent on centrality, although not necessary to be linearly. Note that the fraction of events in each bin must correspond to the total number of events after corrected for efficiency, otherwise that fraction cut is not universal for different experimental setups. The truncated mean of the energy in the Paddles (Paddle Mean (PdlMean)) is used in 200 GeV Au+Au collisions. Figure 4.5(a) shows the clear monotonic relationship between PdlMean from a MC simulation and the number of participating nucleons (N_{part}) from a Glauber model. In Fig. 4.5(b), the distribution of PdlMean had been divided into 18 bins, each of which contains N_f particle:

$$N_f = f \times \frac{N_{obs}^{data}}{\epsilon}, \tag{4.3}$$

where f is the fraction of events in a particular bin.

For the case of Cu+Cu collisions, the number of measurable particles in the Paddles is small and found to be weakly depend on the centrality. Therefore, Cuts were made on the distribution of the total energy in the symmetric regions of the Octagon (EOct). Since the Octagon is also the part of detector for extracting physics information, potential bias might be introduced by measuring event centrality and physics observables in

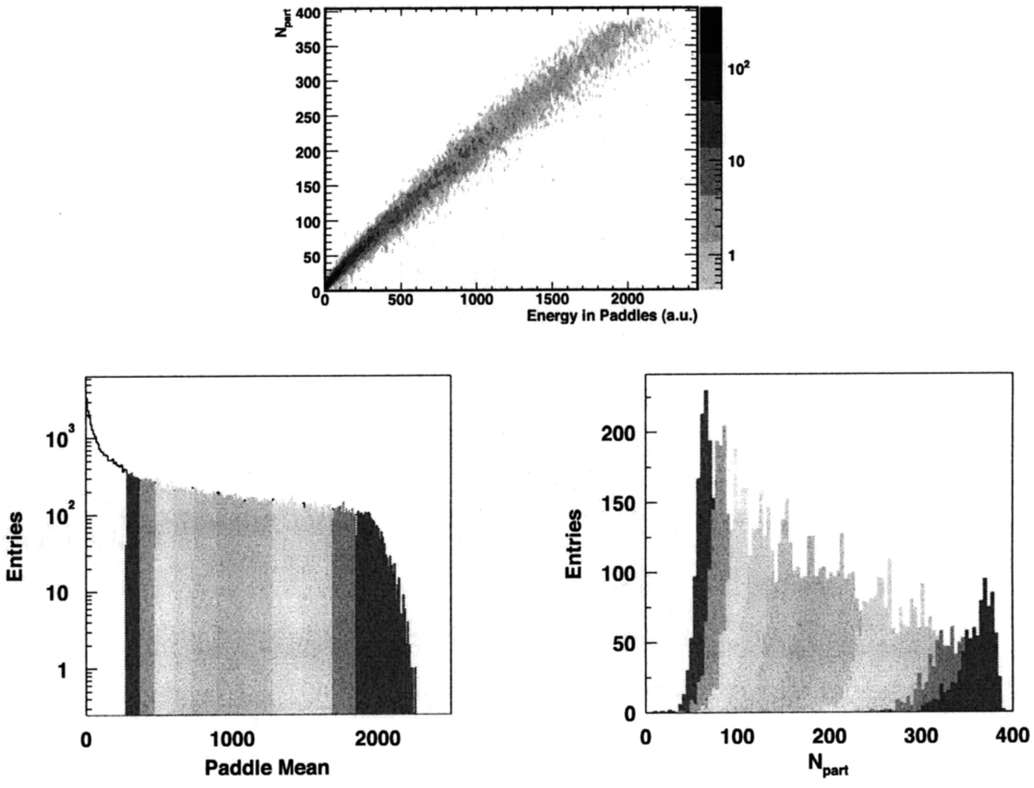

Figure 4.5: (a) The truncated mean signal in the Paddles vs number of participating nucleons (N_{part}) from HIJING MC simulation. (b) The positions of the fractional cross-section cuts on the PdlMean distribution. (c) Distribution of N_{part}in MC for the same bins shown in (b). Figures are taken from Ref. [90].

the same region of pseudorapidity. However, it turned out that only the most central bin was slightly affected.

Additionally, many other variables were also used at PHOBOS for centrality determination for special purposes and cross-checks. These included the sum of the energy in the ZDCs (ZDCSum) and the energy in all six Rings (ERing).

4.4.3 Centrality Variable Estimations

Finally, after dividing events into bins of fractional cross section, the number of participating nucleons (N_{part}) and binary collisions (N_{coll}) in the event can be estimated from the multiplicity variable in each bin, such as PdlMean and EOct. This was done based on the fact that the shape of Paddle slats hit distribution was very similar between data and HIJING model as seen in Fig. 4.4. In HIJING, N_{part}value as well as impact parameter b for each event was known. The N_{part}distributions in HIJING could be calculated for each centrality, as shown in Fig. 4.5(c). The mean N_{part}value of each bin in HIJING was thus taken to be an estimate of that in data for the corresponding bin. To extract the value of N_{coll}, the Glauber model calculation [104] was used, instead of taking directly from HIJING. See Appendix C for the description of the Glauber model.

For Cu+Cu and Au+Au collisions at $\sqrt{s_{\text{NN}}} = 200$ GeV, the estimated N_{part} and N_{coll} values for each centrality bin, and the respective PdlMean or EOct cuts, are summarized in Appendix D.

5 Particle Reconstruction

The angular information (η, ϕ) of the charged particles used in this analysis was derived from the "hits" they left in the detector. Merged hits, which represented the "real" primary particles, were constructed by combining the calibrated signals in the adjacent silicon pads using clustering algorithms.

5.1 Hit Reconstruction and Merging

Calibrated signals from the silicon detectors were recognized as "hits" , left by the trajectories of the charged particles, going through at certain spacial position on the detector and depositing a certain amount of energy. Due to the cylindrical geometry of the Octagon and Vertex detectors, a particle transversing a silicon sensor would always hit multiple pads, particularly at forward direction of small incident angle. The energy loss of this particle would be distributed on several adjacent pads, which was in general proportional to its path length. To avoid over-counting particles, hence generating artificial correlations at extremely short-range, it was very important to reconstruct the "real" particles by properly merging the energy signals from adjacent pads.

Hit merging procedure was performed using a clustering algorithm. The basic idea is summarized as follows. At the first step, hits with energy deposition above a noise threshold were selected as seeds. Then, if the adjacent pads contained an energy within some merging thresholds (a lower threshold to reject background noise and a upper threshold to avoid merging a separate hit), they would be merged to the seed hit to form one reconstructed hit. In the end, the total merged energy of a fully reconstructed candidate hit was checked against a hit threshold to further suppress the noise background and reject secondary particles.

The hit merging algorithm in the Octagon detector was described in details as it was the main detector used in the work of this thesis. Algorithms developed for Vertex and Spectrometer detectors were also mentioned but almost the same to the Octagon, except that the parameters used varied depending on different attributes of the detectors.

	Octagon	Vertex	Spectrometer
Noise Threshold (E^{oct}_{noise})	19.2 KeV	0.3 MIP	0.15 MIP
Merge Low Threshold ($E^{oct}_{mergelow}$)	19.2 KeV	0.3 MIP	0.15 MIP
Merge High Threshold ($E^{oct}_{mergeup}$)	65 - 91 KeV	N/A	N/A
Candidate Hit Threshold (E^{oct}_{hit})	40 - 55 KeV	0.7 MIP	0.5 MIP
Maximum Pads to Merge	3	2 - 3	8

Table 5.1: A summary of the thresholds used in the merging algorithms for the different sub-detectors. One MIP corresponds to 80 KeV for a 300 μm thick silicon pad.

Note that hit merging was only done among neighboring pads in the direction of finer segmentation (η). For the ring detectors, no hit merging was performed due to the near-normal incidence of particles on the sensors. If a pad of the Ring detectors registered an energy deposition greater than a hit threshold, the pad was recorded as a hit.

Octagon Hit Merging

The algorithm was designed based on the geometry of the detector as well as the assumption that in a magnetic field free region, charged particles traveled in a straight-line path. Each pad of the Octagon detector had a width of 2.7 mm in the z direction and a thickness of 0.3 mm. The whole Octagon is 1.1 m long with a distance to the beam pipe of 4.5 cm. Based on a simple geometric calculation, a track could not transverse more than three adjacent pads for the primary vertex range of $|z_{vtx}| < 10$ cm. For this reason, seed hits only tried to seek for shared energies from the most adjacent neighbors. Besides, any particle originating with $|\eta| < 0.5$ had much smaller probability of passing through more than one pad. In this region, the merging of neighboring columns was skipped. This was because, due to the high occupancy of the pads, multiple particles hitting a single pad would be the dominant effect to be taken care of (see Sect. 5.2).

A flow chart in Fig. 5.1 shows the whole procedure of hit merging. The algorithm began by moving outward from the vertex along each row of the Octagon searching for hits containing raw deposited energy (ΔE^{oct}_{raw}) above the Octagon noise threshold, E^{oct}_{noise} (19.2 KeV). Once such a seed hit was found, the energy of each its neighboring column was normalized to the value per 300 μm path length:

$$\Delta E^{oct}_{corr} = \frac{\Delta E^{oct}_{raw}}{sin(\theta_{pad})} \times \frac{300\,\mu\text{m}}{D_{pad}}, \tag{5.1}$$

where θ_{pad} corresponded to the polar angle of the pad relative to the collision vertex and D_{pad} was the thickness of the pad. This was due to the fact that, particles emitted

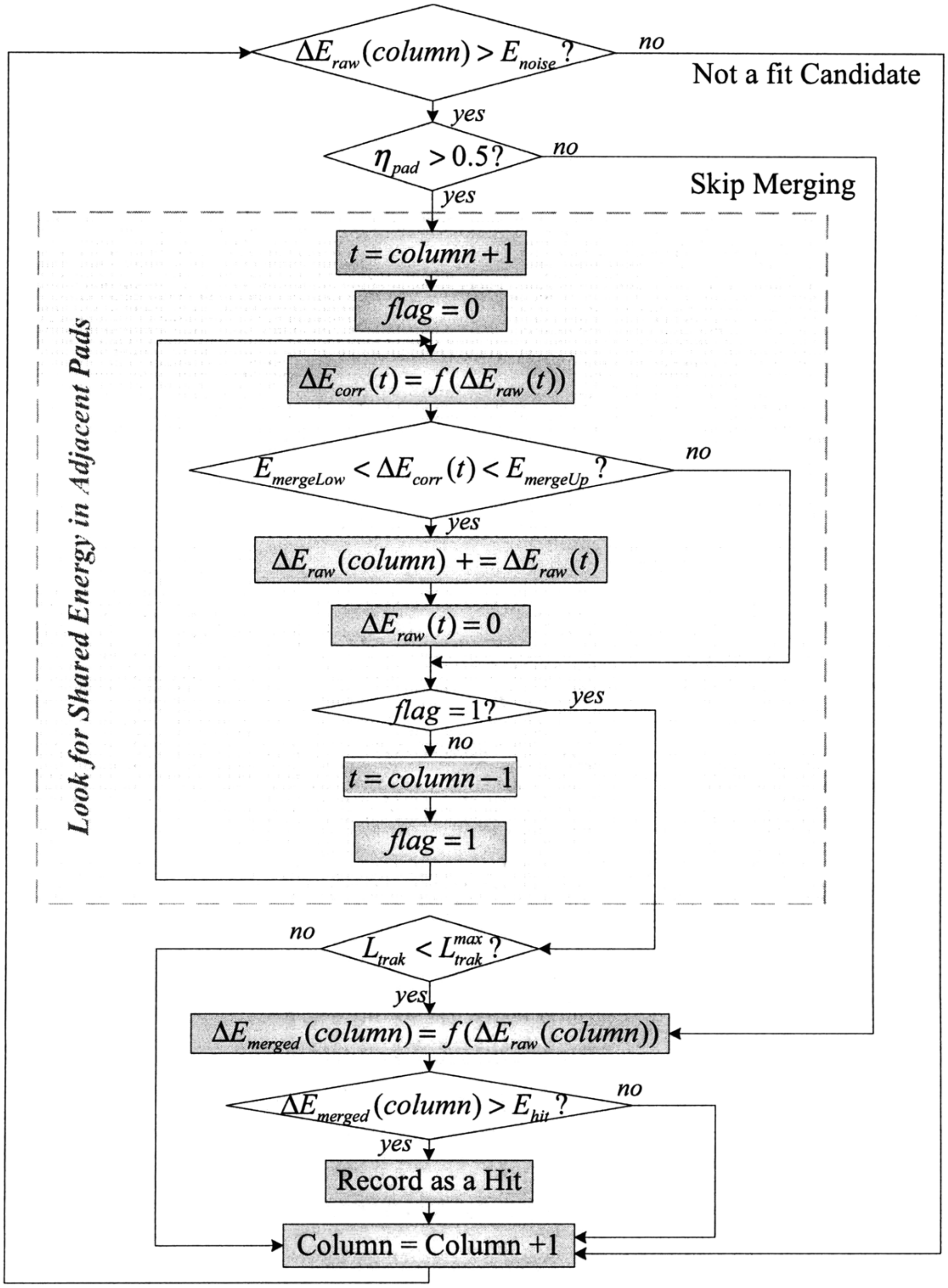

Figure 5.1: Flow chart of hit merging algorithm in adjacent pads.

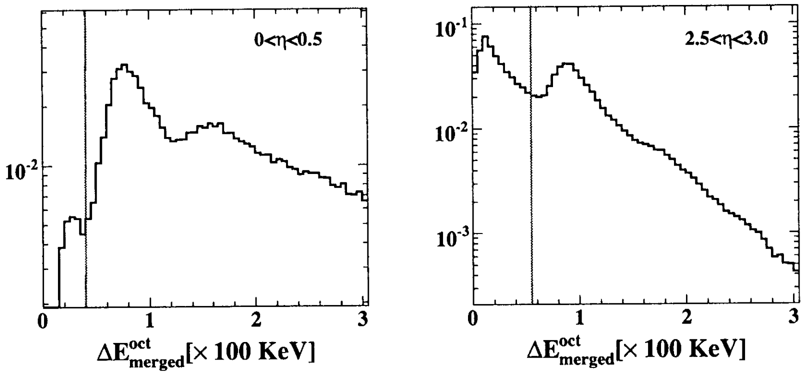

(a) Mid-rapidity (b) Forward Rapidity

Figure 5.2: Distributions of angle-corrected energy loss for candidate hits at (a) mid-rapidity and (b) forward rapidity. The red lines correspond to the threshold above which a primary particle was identified.

at different incident angle deposited energy that was approximately proportional to its path length in the silicon sensor. In order to apply energy cuts on the hits over the whole detector in a consistent way, it was necessary to scale them to a common path length (i.e. at the normal incidence, or equivalently the thickness of the pad), so-called "angle-corrected" energy loss, ΔE^{oct}_{corr}. In addition, the thicknesses of the silicon pads were not always identical all over the detector due to the technical limitations. This effect could also be compensated by applying angle correction. The angle-corrected energy in a neighboring pad was merged to the seed hit only if it fell into the range between the merging lower and upper thresholds ($E^{oct}_{mergelow}$, $E^{oct}_{mergeup}$). If $\Delta E^{oct}_{corr} < E^{oct}_{mergelow}$ (19.2 KeV), this neighboring hit was still considered as a noise hit and rejected. On the other hand, if $\Delta E^{oct}_{corr} > E^{oct}_{mergehigh}$, it had enough energy to be a separate particle and would not be merged. The merging upper threshold was chosen to be as a function of pseudorapidity: $E^{oct}_{mergeup} = 65.0$ KeV + 8.75 KeV $\times|\eta|$ according to studies in Ref. [105]. However, in the p+p collisions where the event multiplicity was significantly low, the probability of two real particles hitting two adjacent pads was negligible. Monte-Carlo studies using the PYTHIA event generator show that, 98% of hits on adjacent pads in η are created by single primary particles with a small angle of incidence. For this reason, $E^{oct}_{mergeup}$ was set to infinity to merge almost all the adjacent pads.

Finally, for a candidate to be considered a proper hit, the number of merged pads of a candidate hit (L_{track}) must not exceed the maximum value (L^{max}_{track}) that could be traversed by a particle at this incident angle. Also, another cut was applied that required

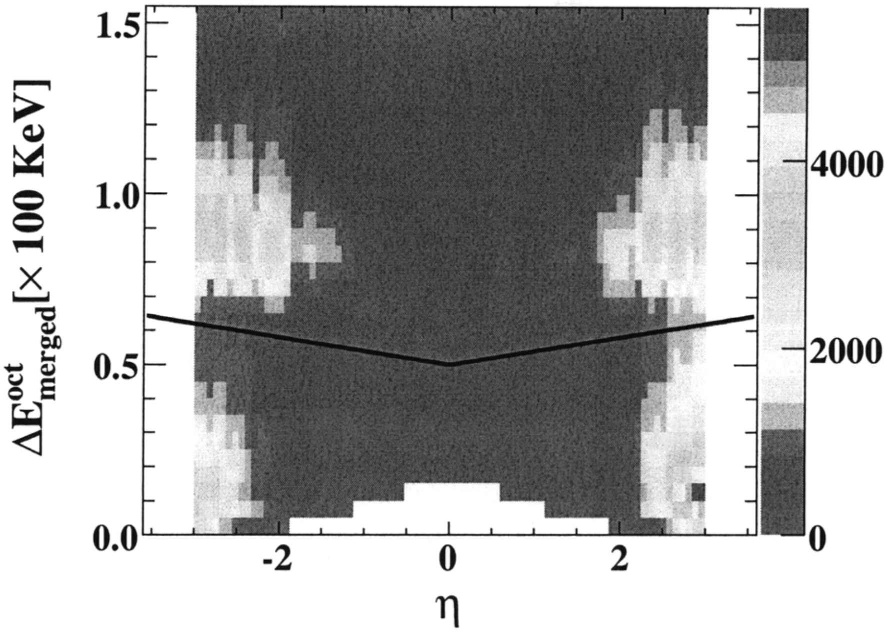

Figure 5.3: The distribution of Octagon hits as a function of pseudorapidity and angle-corrected energy for merged candidate hits. The black line corresponds to the cut of 50.0 KeV + 4.0 KeV $\times|\eta|$. The lack of hits at mid-rapidity is due to the Octagon holes.

its angle-corrected, merged energy, ΔE^{oct}_{merged}, exceeded a hit threshold, E^{oct}_{hit} (see Fig. 5.3). This cut was very effective in excluding a large fraction of secondary particles since if a particle was not originated from the primary vertex, its actual path length in the pad was smaller than what was assumed from the primary vertex, resulting in a small value of ΔE^{oct}_{merged}. Fig. 5.2 shows the distributions of ΔE^{oct}_{merged} for candidate hits at mid-rapidity and forward rapidity. A secondary peak clearly emerged at smaller energy loss region. A cut could be roughly determined between the secondary and primary (80 KeV) peaks at each pseudorapidity slice, which gave a "V"-shaped pseudorapidity dependent hit threshold: $E^{oct}_{hit} = 50.0$ KeV + 4.0 KeV $\times|\eta|$. The threshold parameters for the various sub-detectors are listed in Table 5.1 for comparison.

Vertex Hit Merging

Vertex hits were merged in a similar way to the Octagon hits but for different threshold parameters (see Table 5.1). Moving along each row, seed hits were required to have a

ΔE^{vtx}_{corr} of at least 0.3 MIP, where one MIP corresponds to 80 KeV. The hit in the next column was merged to the seed hit if it also passed the 0.3 MIP cut on its ΔE^{vtx}_{corr}; otherwise, a new hit seed search began. Only two adjacent pads (or three in the region $|\eta| > 0.5$) were allowed to be merged. The final candidate of merged hit was required to have an angle-corrected energy greater than 0.7 MIP to be counted as a hit. The position of the merged Vertex hit was the energy-weighted mean of the merged pads.

Spectrometer Hit Merging

In the Spectrometer, the hit merging procedure was almost identical to that for the Octagon and Vertex detectors, except for different cut parameters (see Table 5.1). Because of the finer resolution in the horizontal direction, charged tracks could traverse the silicon at quite shallow angles after being bent by the magnetic field. Therefore, the maximum number of adjacent pads that could be merged was increased to eight.

5.2 Occupancy Weighting

As going toward more central collisions, the charged multiplicity grew significantly, especially at the mid-rapidity region. In the most central Au+Au collisions, up to 80% of pads on the Octagon at mid-rapidity would show large signals. As a result, the probability that a single silicon pad contained energy deposition from multiple charged particle tracks became very high. In order to extract the "true" information of correlations between primary particles in this analysis, this high "occupancy" effect needed to be properly accounted for.

Several occupancy correction methods had been developed in the previous PHOBOS analysis including the measurements of charged particle multiplicity [105], forward-backward (F-B) multiplicity correlations [106] and elliptic flow [107]. However, those methods turned out not to be directly suitable in this work. To derive two-particle correlations in both $\Delta\eta$ and $\Delta\phi$ dimensions, occupancy effect had to be corrected locally in small η and ϕ region, and also event-by-event. In charged multiplicity measurement, occupancy was only corrected as a function of η after averaging over all the events. F-B multiplicity correlation analysis utilized a semi-analog event-by-event method but still no ϕ dependence was implemented. The attempt of a local event-by-event occupancy correction was first exploited in the elliptic flow analysis using a digital method. The basic idea was to estimate an occupancy weight for a given hit based on the number

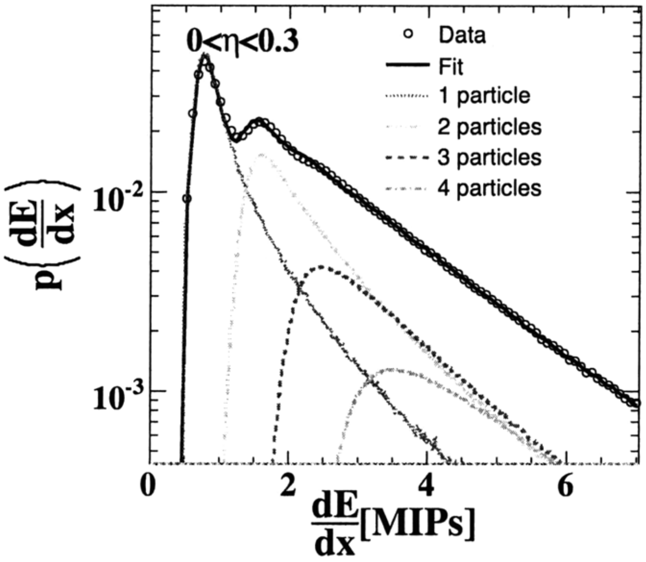

Figure 5.4: dE/dx distribution of hits from the Octagon at $0 < \eta < 0.3$ (open circles) fitted by a sum (solid line) of predicted dE/dx distributions for various number of particles hitting a single pad (dashed lines) for the most central 3% of 200 GeV Au+Au collisions.

of occupied pads in the vicinity of this hit as well as the assumption of Poisson statistics. The drawback of this approach was that the occupancy weights derived for these hits were correlated with each other. In studying the correlations between these hits, additional correlations will be created artificially.

A new analog correction method was developed in this work to effectively compensate for the influence of the occupancy effect event-by-event. The dE/dx[1] distribution of hits in a very low multiplicity environment (e.g. 55%-60% peripheral Cu+Cu with an occupancy of about 4% at midrapidity) has been measured first in a narrow η bin of 0.3 unit (same bin size as for $R(\Delta\eta,\Delta\phi)$), to approximate the dE/dx distribution for a single particle hitting a single silicon pad, $p_1\left(\frac{dE}{dx}\right)$. By sampling $p_1\left(\frac{dE}{dx}\right)$ i times, the dE/dx distribution of i particles hitting a single pad can be predicted, $p_i\left(\frac{dE}{dx}\right)$ (i=1, 2, 3....). Then, the dE/dx distribution in more central data events, $p\left(\frac{dE}{dx}\right)$ (with unit integral), is measured and fitted by a sum of $p_i\left(\frac{dE}{dx}\right)$ (with unit integral) with weighting factor w_i:

$$p\left(\frac{dE}{dx}\right)=\sum_i w_i p_i\left(\frac{dE}{dx}\right) \tag{5.2}$$

---

[1] Unless indicated, dE/dx always refers to the angle-corrected energy loss of merged hits (ΔE^{oct}_{merged}).

as illustrated in Fig. 5.4 for the most central 3% of 200 GeV Au+Au collisions as an example.

With extracted weight w_i, the relative contribution of different number of particles hitting a single pad can be estimated as a function of dE/dx, $w_i p_i\left(\frac{dE}{dx}\right)/\sum_i w_i p_i\left(\frac{dE}{dx}\right)$, (see Fig. 5.5(a)). It suggests that at low dE/dx end, a silicon pad is most likely to be hit by a single primary track, whereas multiple particles per pad event becomes dominant as it goes to higher dE/dx region. The average number of particles per pad can thus be calculated as a function of dE/dx,

$$N\left(\frac{dE}{dx}\right) = \frac{\sum_i i \times w_i p_i\left(\frac{dE}{dx}\right)}{\sum_i w_i p_i\left(\frac{dE}{dx}\right)}. \tag{5.3}$$

which is illustrated in Fig. 5.5(b) for one bin of $0 < \eta < 0.3$.

Performing the procedure above in each η bin, the average number of particles per pad as a function of dE/dx and η, $N\left(\eta, \frac{dE}{dx}\right)$, is derived and shown in Fig. 5.6. In analysis of two-particle correlations, each hit is assigned a weight $N\left(\eta, \frac{dE}{dx}\right)$ based on its η and dE/dx. Using this procedure, the effects of high occupancy are removed at the hit level.

As a cross check, the overall fractional contribution of different number of particles per pad was calculated as follows:

$$P_{data}(N) = \frac{w_N}{\sum_i w_i}, \tag{5.4}$$

which is shown in Fig. 5.7 still for bin $0 < \eta < 0.3$ as an example. It is well fitted by the probability distribution that any pad is hit N times under the assumption of Poisson statistics:

$$P_{poisson}(N) = \frac{\mu^N e^{-\mu}}{N!}, \tag{5.5}$$

where μ corresponds to the true occupancy of the detector.

Again, this cross check can be performed in bins of η for the data (Fig. 5.8(a)), for the fits by Poisson distribution (Fig. 5.8(b)), and for the ratio of data-to-fits (Fig. 5.8(c)). As one can see from Fig. 5.8(c), the probability distribution of N particles hitting a single pad extracted from the data coincide with the Poisson statistics over a wide range of η.

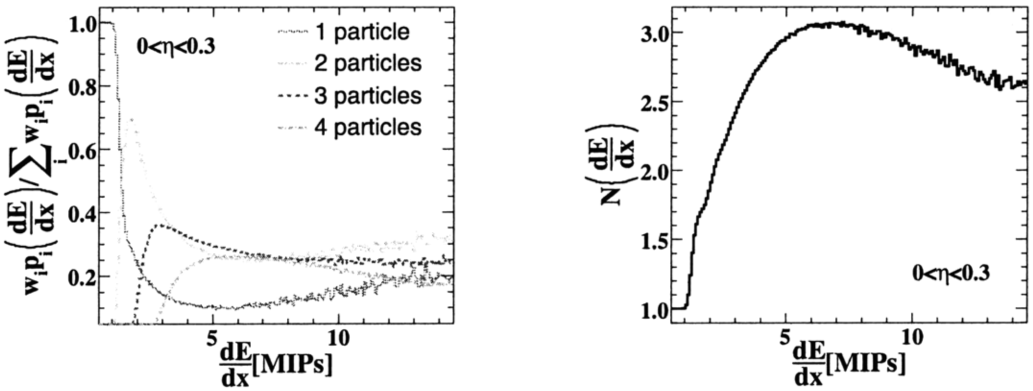

(a) Fractional contribution

(b) Average number of particles pad

Figure 5.5: (a) Fractional contributions from different number of particles per silicon pad and (b) Estimated average number of particles per silicon pad from the Octagon at $0 < \eta < 0.3$ as a function of dE/dx for the most central 3% of 200 GeV Au+Au collisions.

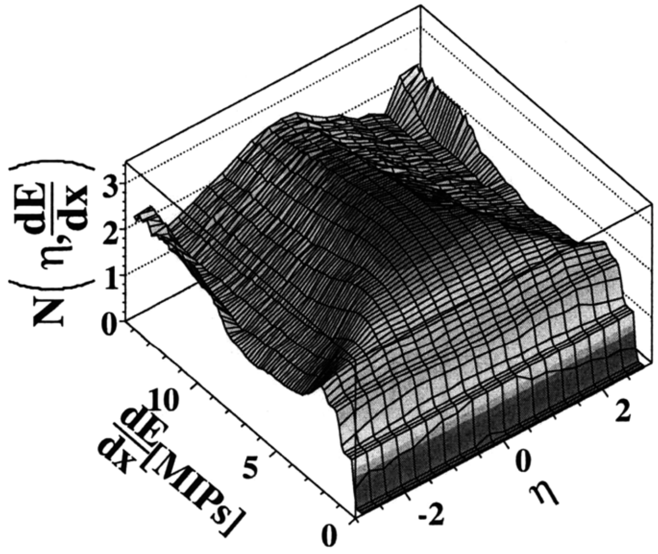

Figure 5.6: Estimated average number of particles per silicon pad from the Octagon as a function of η and dE/dx for the most central 3% of 200 GeV Au+Au collisions.

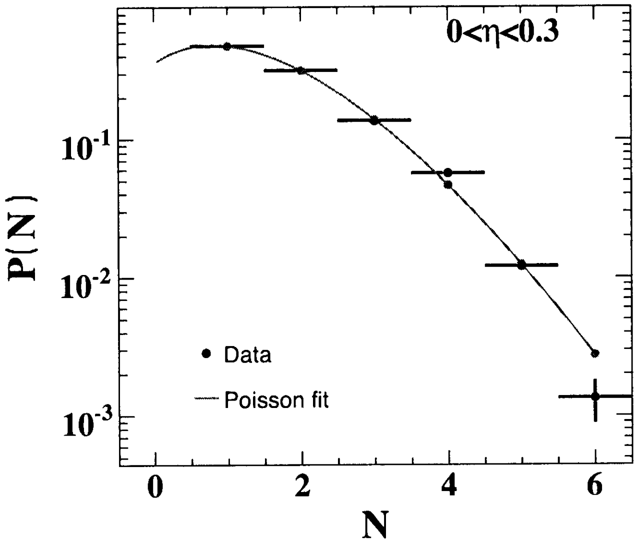

Figure 5.7: The probability distribution of different number of particles per silicon pad from the Octagon at $0 < \eta < 0.3$ for the most central 3% of 200 GeV Au+Au collisions (black solid circles). The solid curve corresponds to the fit by a Poisson distribution. The red solid circles are sampled points at integer values from the Poisson distribution.

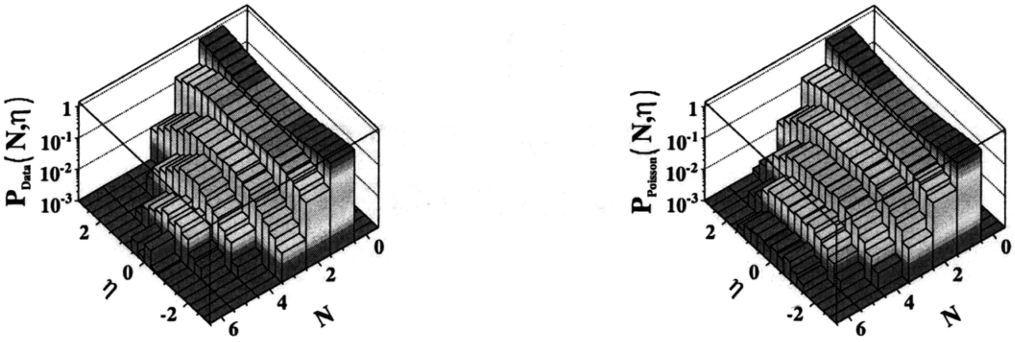

(a) Data

(b) Poisson fits

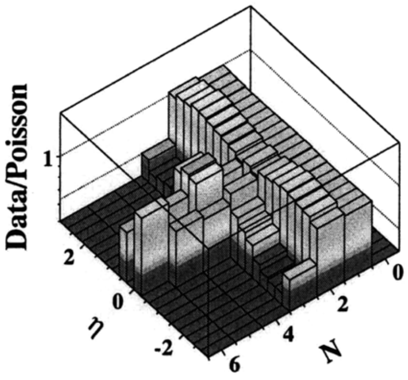

(c) Data-to-fit ratio

Figure 5.8: (a) The probability distribution of different number of particles per silicon pad at different η, (b) The fitted Poisson probability distribution to (a) as a function of number of particles per pad and η, and (c) The ratio of data to Poisson fits for the probability distribution of number of particles per pad from the Octagon at different η for the most central 3% of 200 GeV Au+Au collisions.

6 Technique of Two-particle Angular Correlations

Particle correlation studies at the PHOBOS detector exploit the large $\eta - \phi$ coverage, which is by far the largest of all RHIC experiments. The PHOBOS Octagon detector, covering pseudorapidity $-3 < \eta < 3$ over almost the full azimuth, is well suited to measure the correlations between particles emitted from the collisions. Since the Octagon is a single-layer silicon detector, there is no p_{T}, charge or mass information available on the particles. All charged particles (mean transverse momentum $p_{\mathrm{T}} \sim 450$ MeV) above a low-p_{T} cutoff of 35 MeV/c (which is the threshold for a particle making out of the beryllium beam pipe) are included on equal footing, as opposed to another on-going analysis at PHOBOS which studies the correlations with respect to a high p_{T} triggered particle [108]. Therefore, this work mainly focuses on the soft regime of hadronic physics. Forward Ring, Vertex and Spectrometer subdetectors, which could extend the acceptance up to $-5.4 < \eta < 5.4$, are not used because of the huge background fluctuation and various granularity of the silicon pad.

In this chapter, the analysis technique of two-particle angular $(\Delta\eta, \Delta\phi)$ correlations for inclusive charged particles is developed. In particular, the two-particle correlation function used in this analysis is defined, including the detailed procedure of building signal and background distributions. For a detector with irregular geometrical acceptance (like the PHOBOS Octagon detector), it is essential to properly construct the background such that it precisely cancels the detector inefficiencies in the signal. At the end of this chapter, two-particle correlation functions for MC generator (PYTHIA) are first illustrated as an example.

6.1 Defining the Two-particle Correlation Function

Generally speaking, the angular correlation function measures the increased likelihood that two particles will be found in a particular angular configuration compared to random pairs drawn from the single-particle distribution. Typically, such a correlation function involves the construction of a signal distribution of same event pairs and a background distribution of pairs mixed from different events, which removes all possible correlations. It is of critical importance that the signal and background distributions have similar multiplicity (hence single-particle distributions) and matching detector acceptance. For this reason, the analysis is performed in small bins of collision centrality and event vertex. Following an approach similar to that in Ref. [109], the inclusive charged two-particle angular correlation function in two-particle $(\eta_1, \eta_2, \phi_1, \phi_2)$ space is defined as follows:

$$R(\eta_1,\eta_2,\phi_1,\phi_2)=\left\langle (n-1)\left(\frac{\rho_n^{\rm II}(\eta_1,\eta_2,\phi_1,\phi_2)}{\rho_n^{\rm I}(\eta_1,\phi_1)\rho_n^{\rm I}(\eta_2,\phi_2)}-1\right)\right\rangle \tag{6.1}$$

where,

$$\rho_n^{\rm I}(\eta,\phi)=\frac{1}{n\sigma_n}\frac{d^2\sigma_n}{d\eta d\phi}$$

is the single charged particle density distribution and

$$\rho_n^{\rm II}(\eta_1,\eta_2,\phi_1,\phi_2)=\frac{1}{n(n-1)\sigma_n}\frac{d^4\sigma_n}{d\eta_1 d\eta_2 d\phi_1 d\phi_2}$$

denotes the charged two-particle pair distribution. Here σ_n is the total cross section of observing events with n charged particles. The above distributions obey the normalization relations:

$$\int \rho_n^{\rm I}(\eta,\phi)d\eta d\phi=1$$

and

$$\int \rho_n^{\rm II}(\eta_1,\eta_2,\phi_1,\phi_2)d\eta_1 d\eta_2 d\phi_1 d\phi_2=1.$$

At PHOBOS, we concentrate on the difference in azimuthal angle and pseudorapidity between two particles. The correlation function in Eq. 6.1 is simplified by averaging over $-3<(\eta_1+\eta_2)/2<3$ and $-180^\circ<(\phi_1+\phi_2)/2<180^\circ$ (for the PHOBOS Octagon), reducing the dimensionality of the parameter space to $\Delta\eta(=\eta_1-\eta_2)$ and $\Delta\phi(=\phi_1-\phi_2)$ with a range of $|\Delta\eta|<6$ and $|\Delta\phi|<180^\circ$:

$$R(\Delta\eta,\Delta\phi)=\left\langle (n-1)\left(\frac{\rho_n^{\rm II}(\Delta\eta,\Delta\phi)}{\rho^{\rm mixed}(\Delta\eta,\Delta\phi)}-1\right)\right\rangle. \tag{6.2}$$

The pair distribution $\rho_n^{\rm II}(\Delta\eta,\Delta\phi)$ (with unit integral) is determined by taking particle pairs from the same event, then averaging over all events. The mixed-event background, $\rho^{\rm mixed}(\Delta\eta,\Delta\phi)$ (with unit integral), is constructed by randomly selecting single particles from two different events with similar vertex position and centrality bin, representing a product of two single-particle distributions.

The vertex bin size used in event-mixing is chosen to be 0.5 cm for p+p collisions and 0.2 cm for Cu+Cu and Au+Au collisions, mainly determined by the vertex resolution of the detector. Since the background is found to be largely multiplicity independent (i.e. within a centrality bin of heavy ion collision), we use the inclusive $\rho^{\mathrm{mixed}}(\Delta\eta, \Delta\phi)$ in our calculations of Eq. 6.2. The track multiplicity n is introduced in $R(\Delta\eta, \Delta\phi)$ to compensate for trivial dilution effects from uncorrelated particles [109]. This stems from the fact that the number of uncorrelated pairs grows quadratically with n, while the number of correlated pairs grows only linearly. In this way, if a heavy ion collision is simply a superposition of individual p+p collisions, and thus has the same local correlations, the same correlation function should be observed.

6.2 Building the Signal and Background distribution

For determining the signal pair distribution, the $\Delta\eta$ and $\Delta\phi$ of all possible two-particle pairs in each event are first calculated, and filled a distribution $\rho_n^{\mathrm{II}}(\Delta\eta, \Delta\phi)$ that is scaled to unit integral. It is then weighted by the event multiplicity normalization term $(n-1)$ within the measured acceptance and averaging over all events, which gives $\left\langle (n-1)\rho_n^{\mathrm{II}}(\Delta\eta, \Delta\phi) \right\rangle$.

The background distribution, $\rho^{\mathrm{mixed}}(\Delta\eta, \Delta\phi)$, is constructed using the so-called event-mixing technique. Two particles of a mixed pair are randomly picked from two different events within the same vertex and centrality bins such that they have similar single-particle distributions (as already mentioned). Limited by the angular resolution, mixed pairs whose two particles hit the same pad of the Octagon sensors are rejected since these pairs cannot be identified in the signal distribution. The vertex of each event has also been set to discrete value, i.e. the center of each vertex bin. This is due to the fact that for pairs in the signal distribution, their two particles always originate from exactly the same vertex positions, while it is normally not the case in the background without vertex binning (all events within a vertex bin are allowed to form mixed pairs). Since sensors on the Octagon are generally not in perfect close contact, a slight mismatch of event vertex in the background effectively increases the gap between the sensors, thus reducing the efficiency in making pairs compared to the signal. The tiny shift of the event vertex is found to have negligible impact on angular variables (η, ϕ) of the particles, hence nor on the final results.

Practically, instead of carrying out event-mixing process among all the available events. Events are subdivided into pools, each of which contains a certain number of events. Background is derived in each pool of events and averaged over all the event pools in the end. This essentially distributes the task of event-mixing into parallel jobs so that the process tremendously speeds up.

In order to gain high quality mixed-event background, two major factors need to be determined appropriately for each event pool:

- (1) Number of events contained
- (2) Number of mixed pairs to be generated

The number of events per pool should be large enough to acquire sufficient statistics. On the other hand, it shouldn't be too big since the potential fluctuation as a function of time in the external condition of the detector could induce artificial signals for very large dataset collected over a long period of time. Typically, a couple of hundred up to several thousand events are included for each pool.

Similarly, the number of mixed pairs should also be large enough to reach a good signal-to-background ratio, and limited to avoid "over-sampling", i.e. the same pair of particles being picked more than once. For a pool of N events with on average $\overline{n}$ particles per event, the total number of available particles would be $N_{\text{particle}} = \overline{n} * N_{\text{evt}}$. The maximal number of mixed pairs that could possibly be formed without over-sampling, therefore, is approximately

$$N_{\text{pair}}^{\text{max}} = \frac{N_{\text{particle}} * (N_{\text{particle}} - 1)}{2}, \tag{6.3}$$

regardless of all the requirements on the pairs which generally make $N_{\text{pair}}^{\text{max}}$ much smaller. To estimate the probability of over-sampling, let N_{pair} be the number of mixed pairs to be taken. The total number of different ways of taking N_{pair} pairs which allows over-sampling would be:

$$C_{N_{\text{pair}}^{\text{max}}+N_{\text{pair}}-1}^{N_{\text{pair}}} = \frac{(N_{\text{pair}}^{\text{max}} + N_{\text{pair}} - 1)!}{N_{\text{pair}}!(N_{\text{pair}}^{\text{max}} - 1)!}. \tag{6.4}$$

On the other hand, if over-sampling is prohibited, this number reduces to:

$$C_{N_{\text{pair}}^{\text{max}}}^{N_{\text{pair}}} = \frac{(N_{\text{pair}}^{\text{max}})!}{N_{\text{pair}}!(N_{\text{pair}}^{\text{max}} - N_{\text{pair}})!}. \tag{6.5}$$

Consequently, the probability of over-sampling can be calculated as follow:

$$P_{\text{over-sample}} = 1 - \frac{C^{N_{\text{pair}}}_{N^{\text{max}}_{\text{pair}}}}{C^{N_{\text{pair}}}_{N^{\text{max}}_{\text{pair}}+N_{\text{pair}}-1}} \tag{6.6}$$

which indicates that as long as $N^{\text{max}}_{\text{pair}} \gg N_{\text{pair}}$, $P_{\text{over-sample}}$ is ~ 0. In choosing the value of N_{pair}, it is more convenient to parametrize it as $N_{\text{pair}} = N_{\text{particle}} * f$, where f basically represents on average the frequency of each particle in the event pool paired with other particles from different events. Since $N^{\text{max}}_{\text{pair}} \propto (N_{\text{particle}})^2$, the over-sampling issue can be avoided by properly selecting f such that the condition $N_{\text{particle}} \gg f$ is fulfilled. The signal-to-background pair ratio is calculated to be $\sim \overline{n}/f$, and typically requires a value between 1/4 and 1/10 to guarantee that the uncorrelated-pair background in the signal is well reproduced by the mixed-event distribution. Parameters of event-mixing technique eventually used in this work are listed in Table 6.3 for different types of collisions.

A set of sample signal and background distributions for PYTHIA MC event generator at primary particle level are shown in Fig. 6.1. The overall shapes of signal and background are largely similar. To extract the information of correlations, the two-particle correlation function is calculated according to Eq. 6.2 and displayed in Fig. 6.2 for generator level PYTHIA. The actual information in $R(\Delta\eta, \Delta\phi)$ is reflected to the full $\Delta\eta$ and $\Delta\phi$ range in order to more clearly show the shape of the correlation function. As one can see, copious structures emerge in Fig. 6.2 for PYTHIA even without any selection in p_{T} of the particles. The physical implications of two-particle correlation functions will be discussed later in Chapter 8.

6.3 Projected 1-D $\Delta\eta$ and $\Delta\phi$ Correlation Function

To analyze the correlation structure quantitatively, the 2-D correlation function is projected into a 1-D correlation functions $R(\Delta\eta)$ and $R(\Delta\phi)$ by integrating $\rho^{\text{II}}_n(\Delta\eta, \Delta\phi)$ and $\rho^{\text{mixed}}(\Delta\eta, \Delta\phi)$ separately as follows:

$$\begin{aligned} R(\Delta\eta) &= \left\langle (n-1)\left(\frac{\int \rho^{\text{II}}_n(\Delta\eta, \Delta\phi)d\Delta\phi}{\int \rho^{\text{mixed}}(\Delta\eta, \Delta\phi)d\Delta\phi} - 1\right)\right\rangle \\ &= \left\langle (n-1)\left(\frac{\rho^{\text{II}}_n(\Delta\eta)}{\rho^{\text{mixed}}(\Delta\eta)} - 1\right)\right\rangle. \end{aligned} \tag{6.7}$$

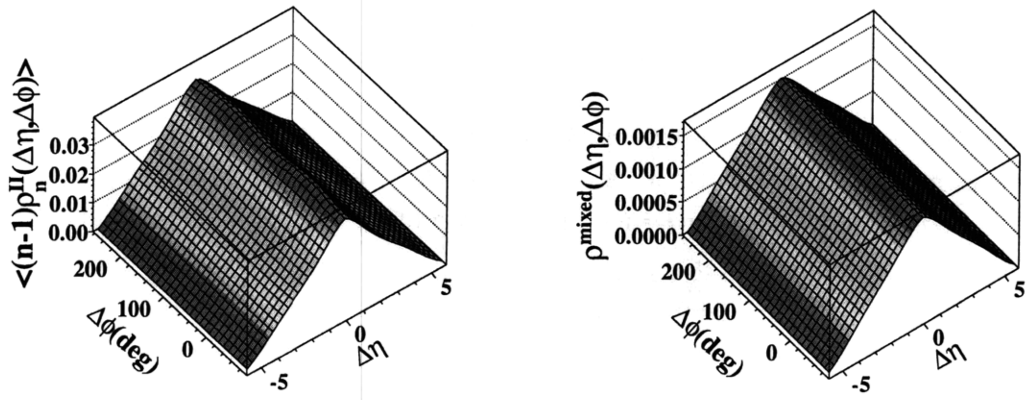

(a) Signal, PYTHIA

(b) Mixed-Event Background, PYTHIA

Figure 6.1: (a) Signal and (b) Mixed-event background ($\Delta\eta$,$\Delta\phi$) distributions for PYTHIA with primary tracks at $\sqrt{s} = 200$ GeV.

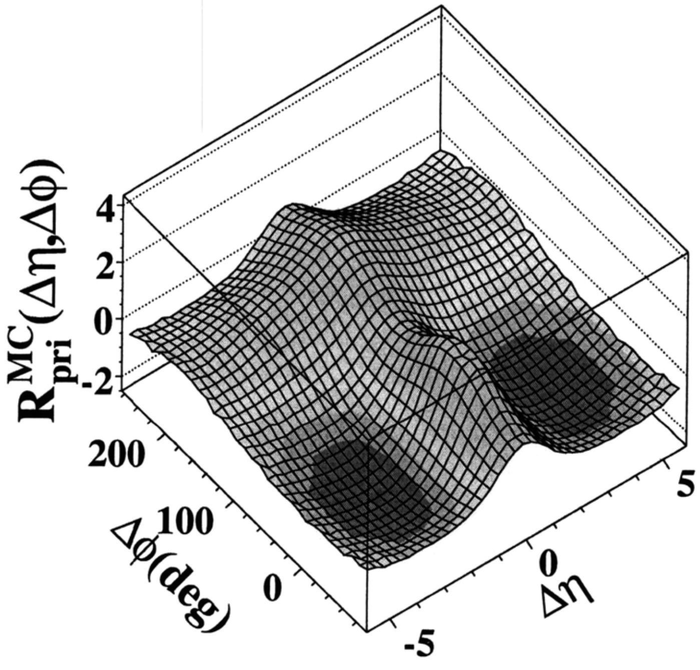

Figure 6.2: Two-particle correlation function in $\Delta\eta$ and $\Delta\phi$ for PYTHIA with primary tracks at $\sqrt{s} = 200$ GeV.

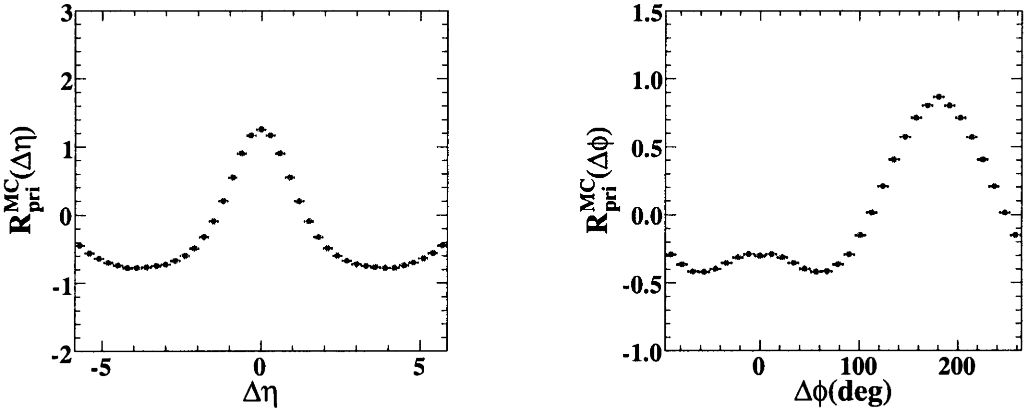

(a) 1-D $\Delta\eta$, PYTHIA

(b) 1-D $\Delta\phi$, PYTHIA

Figure 6.3: Projected 1-D two-particle correlation functions (a) in $\Delta\eta$ and (b) in $\Delta\phi$ for PYTHIA with primary tracks at $\sqrt{s} = 200$ GeV.

$$\begin{aligned} R(\Delta\phi) &= \left\langle (n-1)\left(\frac{\int \rho_n^{\mathrm{II}}(\Delta\eta, \Delta\phi) d\Delta\eta}{\int \rho^{\mathrm{mixed}}(\Delta\eta, \Delta\phi) d\Delta\eta} - 1 \right) \right\rangle \\ &= \left\langle (n-1)\left(\frac{\rho_n^{\mathrm{II}}(\Delta\phi)}{\rho^{\mathrm{mixed}}(\Delta\phi)} - 1 \right) \right\rangle . \end{aligned} \tag{6.8}$$

Results for PYTHIA with primary particle tracks are shown in Fig. 6.3.

p+p, 200 GeV					p+p, 410 GeV				
Centrality Bin	Z_{vtxbin} (mm)	$\overline{n}_{\lvert\eta\rvert<3}$	f	$\overline{n}_{\lvert\eta\rvert<3}/f$	Centrality Bin	Z_{vtxbin} (mm)	$\overline{n}_{\lvert\eta\rvert<3}$	f	$\overline{n}_{\lvert\eta\rvert<3}/f$
N/A	5	15	400	0.04	N/A	5	17	400	0.04

Cu+Cu, 200 GeV					Au+Au, 200 GeV				
Centrality Bin	Z_{vtxbin} (mm)	$\overline{n}_{\lvert\eta\rvert<3}$	f	$\overline{n}_{\lvert\eta\rvert<3}/f$	Centrality Bin	Z_{vtxbin} (mm)	$\overline{n}_{\lvert\eta\rvert<3}$	f	$\overline{n}_{\lvert\eta\rvert<3}/f$
7 (45%-50%)	2	140	1400	0.10	7 (45%-50%)	2	399	3500	0.11
8 (40%-45%)	2	175	1600	0.11	8 (40%-45%)	2	511	4000	0.13
9 (35%-40%)	2	215	1800	0.12	9 (35%-40%)	2	642	4500	0.14
10 (30%-35%)	2	263	2000	0.13	10 (30%-35%)	2	798	5000	0.16
11 (25%-30%)	2	320	2200	0.15	11 (25%-30%)	2	984	5500	0.18
12 (20%-25%)	2	386	2400	0.16	12 (20%-25%)	2	1203	6000	0.20
13 (15%-20%)	2	463	2600	0.18	13 (15%-20%)	2	1464	6500	0.23
14 (10%-15%)	2	554	2800	0.20	14 (10%-15%)	2	1774	7000	0.25
15 (6%-10%)	2	650	3000	0.22	15 (6%-10%)	2	2087	7500	0.28
16 (3%-6%)	2	740	3200	0.23	16 (3%-6%)	2	2383	8000	0.30
17 (0%-3%)	2	852	3400	0.25	17 (0%-3%)	2	2656	8500	0.31

Table 6.1: A summary of parameters used in the mixed-event background technique.

7 Data analysis and Corrections

Following the development of formalism in Chapter 6, procedure of obtaining the two-particle correlation functions in the data is described in this chapter, including various corrections applied and studies of the systematic uncertainties. In particular, preliminary results in p+p collisions are discussed in both 2-D and 1-D for illustration.

7.1 Event and Particle Selection

The data presented in this work for p+p collisions at $\sqrt{s} = 200$ and 410 GeV, Cu+Cu and Au+Au collisions at $\sqrt{s_{\rm NN}} = 200$ GeV were collected during RHIC Run 4 (2004) and Run 5 (2005) using the large-acceptance PHOBOS Octagon multiplicity detector. Single diffractive events in p+p collisions were suppressed by requiring at least one hit in each of two sets of 16 scintillator paddle counters located at distances of −3.21 m and 3.21 m from the nominal interaction point z_{vtx}=0 along the beam axis. They cover an acceptance of $3 < |\eta| < 4.5$ and $-180° < \phi < 180°$. For Cu+Cu and Au+Au collisions, the primary event trigger used the time difference between signals in two sets of 10 Čerenkov counters located at $4.4 < |\eta| < 4.9$, to select collisions that were close to z_{vtx}=0. Events that passed all the cuts used in this analysis are summarized in Table 7.1.

The angular coordinates (η, ϕ) of charged particles are measured using the spacial location of merged hits in the Octagon. Noise and background hits are rejected by placing a lower threshold on the deposited energy corrected for the path length through the silicon after hit merging, assuming that the charged particle originated from the main vertex. Depending on η, the merged hits with less than 50-60% of the energy loss expected for a Minimum Ionizing Particle (MIP) are rejected. In analysis of A+A collisions, a weight also is assigned to each hit to compensate for high occupancy effect. More details of hit reconstruction have been described in Chapter 5.

	p+p, 200 GeV	**p+p, 410 GeV**
Magnetic field	Off	Off
Trigger Condition	IsCol && Paddle.Nn>0 && Paddle.Np>0 (L0&0x0013)!=0 && (L1&0x0004)!=0	IsCol && Paddle.Nn>0 && Paddle.Np>0 (L0&0x0013)!=0 && (L1&0x0004)!=0
Vertex Selection	$\|z_{vtx}\| < 10$ cm, OctDeVertex	$\|z_{vtx}\| < 10$ cm, OctDeVertex
Dead Channel Map	DeadChannelHitArraysPR04_ppRepass	DeadChannelHitArraysPR05_ppRepass
Detector Geometry	PR04pp.0.SURVEY_3.ALIGN.2	PR05.0.SURVEY_3.ALIGN.2
# of events selected	0.25 M	0.30 M

	Cu+Cu, 200 GeV	**Au+Au, 200 GeV**
Magnetic field	On	On
Trigger Condition	|PdlTDiff|<5 && Paddle.Nn>2 && Paddle.Np>2 (L1&0x0100)=0 && TrgT.Extra[7]>0	IsCol && Paddle.Nn>2 && Paddle.Np>2 NotPrePileup && NotPostPileup
Vertex Selection	$\|z_{vtx}\| < 6$ cm, OctProbMultVertex	$\|z_{vtx}\| < 6$ cm, RMSSelVertex
Centrality Class	Bin 7 (45 – 50%) through 17 (0 – 3%), PR05 EOct TrgCuts (Appendix D)	Bin 7 (45 – 50%) through 17 (0 – 3%), PR04 PdlMean TrgCuts (Appendix D)
Dead Channel Map	DeadChannelHitArraysPR05_BOFF	DeadChannelHitArraysPR04_ppRepass
Detector Geometry	PR05.0.SURVEY_3.ALIGN.2	PR04.0.SURVEY_3.ALIGN.2
# of events selected	4.0 M	4.0 M

Table 7.1: A summary of the event selection for the two-particle correlations analysis in p+p, Cu+Cu and Au+Au collisions.

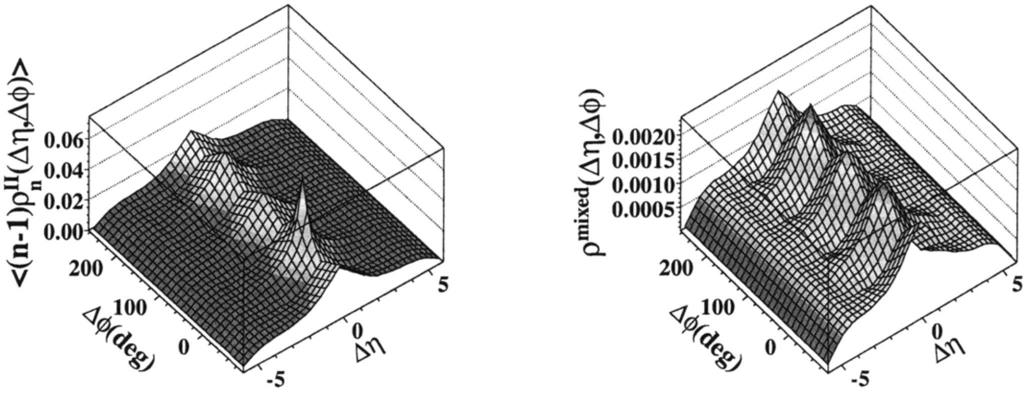

(a) Signal, Raw p+p data

(b) Mixed-Event Background, Raw p+p data

Figure 7.1: (a) Signal and (b) Mixed-event background ($\Delta\eta$,$\Delta\phi$) distributions in one z_{vtx} bin ($0.0 < z_{vtx} < 0.5$ cm) for p+p collisions at $\sqrt{s} = 200$ GeV.

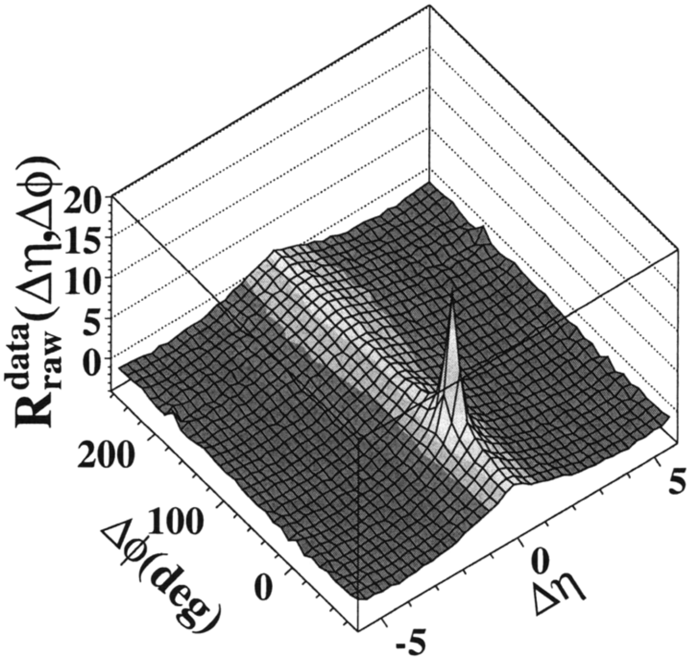

Figure 7.2: Two-particle correlation function in $\Delta\eta$ and $\Delta\phi$, in one z_{vtx} bin ($0.0 < z_{vtx} <$ 0.5 cm) for raw data in p+p collisions at $\sqrt{s} = 200$ GeV.

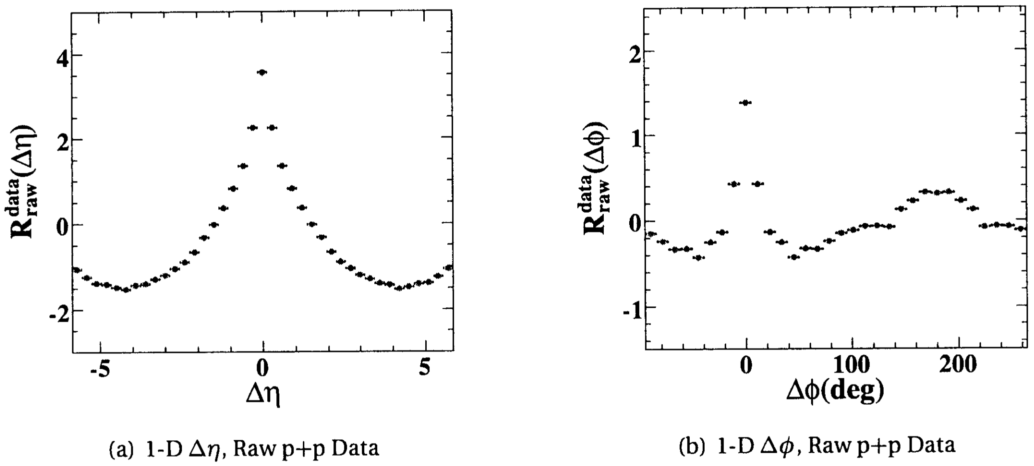

(a) 1-D $\Delta\eta$, Raw p+p Data

(b) 1-D $\Delta\phi$, Raw p+p Data

Figure 7.3: Projected 1-D two-particle correlation functions (a) in $\Delta\eta$ and (b) in $\Delta\phi$, in one z-vertex bin ($0.0 < z_{vtx} < 0.5$ cm) for raw data in p+p collisions at $\sqrt{s} = 200$ GeV.

7.2 Preliminary Results of Raw Data

Signal and background distributions in p+p collisions at $\sqrt{s} = 200$ GeV for one z-vertex bin ($0.0 < z_{vtx} < 0.5$ cm) are presented in Fig. 7.1, similarly to the case of PYTHIA in Fig. 6.1. As one can see, the irregular structures which exist in both signal and background of data are due to the holes on the Octagon, resulting in inefficiency of obtaining pairs especially with $\Delta\phi \sim 45°$ and 135°. However, after dividing the signal by the background, all the structures induced by the detector acceptance are essentially canceled out in the correlation function $R(\Delta\eta, \Delta\phi)$ (see Fig. 7.2). A huge spike emerges around $(\Delta\eta, \Delta\phi) \sim (0, 0)$ in $R(\Delta\eta, \Delta\phi)$. Such a strong short-range correlation in p+p collisions is in general not expected without any triggering on high p_T particles. MC studies show that it is mainly contributed by the secondary detector effects such as δ-electrons[1], γ conversions[2] and weak decays.

1-D correlation functions $R(\Delta\eta)$ and $R(\Delta\phi)$ are also obtained by projecting $\rho^{II}_{n}(\Delta\eta, \Delta\phi)$ and $\rho^{mixed}(\Delta\eta, \Delta\phi)$ following Eq. 6.7. The results are shown in Fig. 7.3 for the raw p+p data.

---

[1] Electrons produced by energetic charged particles knocking orbiting electrons out of atoms.

[2] A photon converts into a e^+e^- pair when interacting with materials

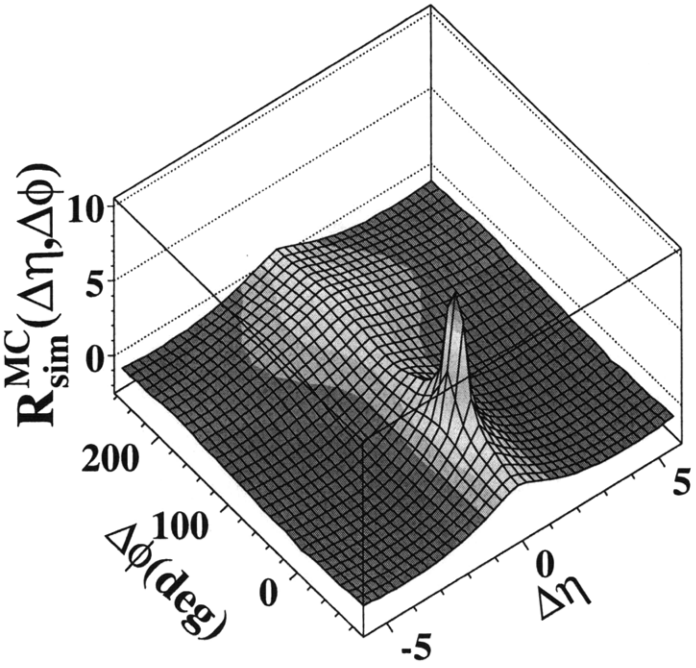

Figure 7.4: Two-particle correlation function in $\Delta\eta$ and $\Delta\phi$ for PYTHIA with full GEANT detector simulation and reconstruction procedures in one z_{vtx} bin ($0.0 < z_{vtx} < 0.5$ cm) at $\sqrt{s} = 200$ GeV.

7.3 Correction Procedure to Raw Correlation Function

With a single layer silicon of the PHOBOS Octagon detector, only one hit of each charged track can be measured. Secondary effects that are mainly caused by the interactions between primary particles and experimental materials (beam pipe, detector etc.), such as δ-electrons, γ conversions (into e^+e^- pairs) and weak decays cannot be directly rejected. These will contribute to correlations unrelated to those between primary hadrons, and modify the shape of the measured correlation function especially at very short-range. Besides, the incomplete azimuthal acceptance in some pseudorapidity regions naturally suppresses the overall correlation strength, but MC simulations show that it does not change the shape of the correlation in $\Delta\eta$ and $\Delta\phi$. In order to correct for these detector effects in the data, correlation functions are calculated for MC p+p events (e.g. PYTHIA) at $\sqrt{s} = 200$ GeV both at the generator level for true primary charged hadrons, $R^{MC}_{pri}(\Delta\eta,\Delta\phi)$ (Fig. 6.2) and with the full GEANT detector simulation (which calibrates the detector responses) and reconstruction procedure, $R^{MC}_{sim}(\Delta\eta,\Delta\phi)$

(Fig. 7.4). The whole correction procedure can be summarized by the following equation:

$$R^{\text{data}}_{\text{final}}(\Delta\eta,\Delta\phi) = A\times[R^{\text{data}}_{\text{raw}}(\Delta\eta,\Delta\phi) - S(\Delta\eta,\Delta\phi)]. \tag{7.1}$$

This procedure applies to 1-D correlation functions in exactly the same way as well.

To get the final correlation function, $R^{\text{data}}_{\text{final}}(\Delta\eta,\Delta\phi)$, one applies Eq. 7.1 to the raw correlation function (after occupancy hit weighting in A+A collisions), $R^{\text{data}}_{\text{raw}}(\Delta\eta,\Delta\phi)$. The correction term $S(\Delta\eta,\Delta\phi)$ is used to subtract the effects of secondaries and weak decays, and the constant scaling factor, A, is used to remove the overall suppression in correlation functions due to the holes, hot and dead channels, as well as gaps between the silicon sensors in the PHOBOS acceptance. This procedure is done separately for each vertex bin, and then average over all the vertex bins. Three different MC generators are used to estimate the systematic uncertainties to the correlation function from this correction procedure, including PYTHIA, HIJING, and a modified PYTHIA in which all intrinsic correlations have been removed by performing event-mixing at the primary hadron level (i.e. before weak decays). Typically the systematic error (biggest for the peak at $\Delta\eta$=0 and $\Delta\phi$=0) is less than 5%.

7.3.1 Secondary Correction

The overall correlation structure consists of both intrinsic and secondary correlations and these two sources of correlations are found to be largely independent of each other in MC studies, i.e. the correlation from secondaries is mostly determined by sensor thickness, detector geometry, known cross-sections and decay kinematics. Within a narrow vertex range (0.5cm), the generator level MC correlation function excluding particles outside the PHOBOS detector acceptance, $R^{\text{MC}}_{\text{pri,acc}}(\Delta\eta,\Delta\phi)$, is compared to the correlation function observed after processing the same MC events with all the primary hadrons through the GEANT simulation (with occupancy hit weighting in A+A collisions), $R^{\text{MC}}_{\text{sim}}(\Delta\eta,\Delta\phi)$ (Fig. 7.4). The difference between the two correlation functions, $S(\Delta\eta,\Delta\phi)$ (Fig. 7.5(a)), is attributed to the effects of secondary interactions, weak decays, and the reconstruction procedure:

$$S(\Delta\eta,\Delta\phi) = R^{\text{MC}}_{\text{sim}}(\Delta\eta,\Delta\phi) - R^{\text{MC}}_{\text{pri,acc}}(\Delta\eta,\Delta\phi). \tag{7.2}$$

To validate that the secondary correction function is independent of the input primary correlations, $S(\Delta\eta,\Delta\phi)$ obtained from standard PYTHIA generator is compared to HIJING and a modified PYTHIA with all the intrinsic correlations destroyed using event-

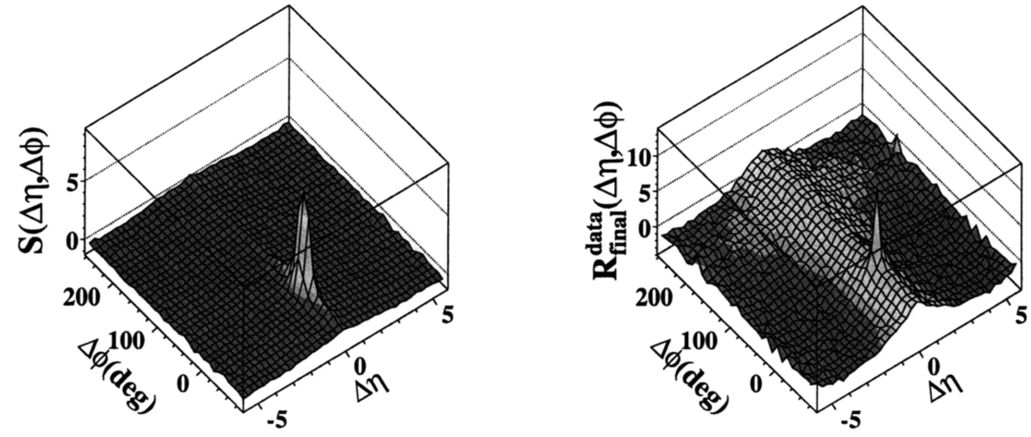

(a) Secondary Correction Function

(b) Final Correlation Function

Figure 7.5: (a) Secondary correction function $S(\Delta\eta, \Delta\phi)$ obtained from PYTHIA and (b) Final two-particle correlation function in $\Delta\eta$ and $\Delta\phi$, in one z_{vtx} bin ($0.0 < z_{vtx} < 0.5$ cm) for p+p collision data at $\sqrt{s} = 200$ GeV.

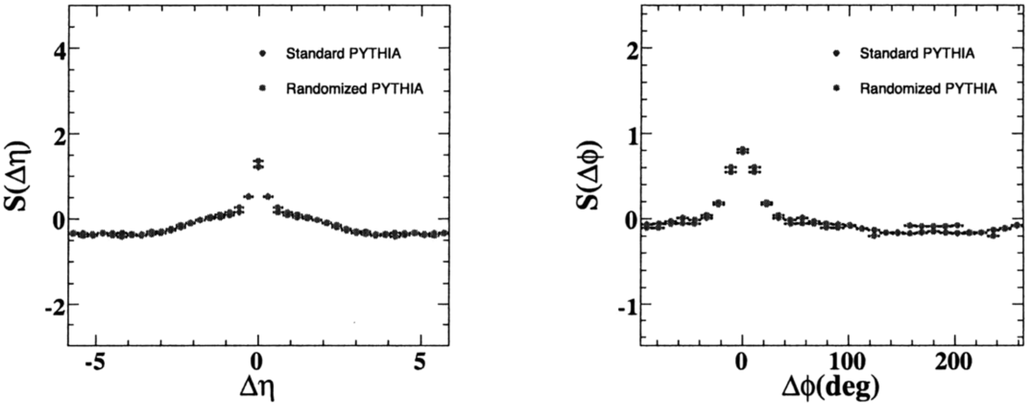

(a) 1-D $\Delta\eta$ Secondary Correction Function

(b) 1-D $\Delta\phi$ Secondary Correction Function

Figure 7.6: Comparison of 1-D secondary correction functions (a) in $\Delta\eta$ and (b) in $\Delta\phi$ obtained from Standard PYTHIA and modified PYTHIA with all the intrinsic correlations destroyed using event-mixing.

mixing and found to be the same except a little discrepancy up to at most 2% at the peaks (see Fig. 7.6 for 1-D case of $\Delta\eta$).

As one can see, both the 2-D correlation function for the data (Fig. 7.2) and for the PYTHIA simulations (Fig. 7.4) have a sharp peak at small $\Delta\eta$ and $\Delta\phi$, which is twice as high in the data as in the fully simulated MC events, but not present in the analysis using primary particles from the MC generator (Fig. 6.2). In the full GEANT simulations, the particles contributing to this peak are found to be mainly δ-electrons (50%) and γ conversions (40%). The width of the peak is about 0.3 in $\Delta\eta$ and 28° in $\Delta\phi$ for both data and MC, indicating the same origin. However, the final data still contain a much narrower peak at the near-side of $R^{\rm data}_{\rm final}(\Delta\eta,\Delta\phi)$ (Fig. 7.5(b)). It is likely that this small angle structure results from background and detector effects which are not fully included in the GEANT MC simulation, although it is not possible to rule out unknown physics effects not implemented in the event generators. Since the physics of the cluster-like particle production investigated in this analysis is dominated by correlations on scales of approximately one unit in $\Delta\eta$, as will be shown later, the analysis proceeds by rejecting pairs in a small two-particle acceptance of $|\Delta\eta| < 0.15$ and $|\Delta\phi| < 5.625°$ (the single bin centered at $\Delta\eta$=0 and $\Delta\phi$=0). Studies using primary particles from MC generators and the fully simulated events show that the extracted cluster parameters, described in Chapter 8, change by less than 0.1% due to this cut.

7.3.2 Incomplete Acceptance and Efficiency Correction

To estimate the suppression in correlation strength due to detector acceptance and inefficiencies, $R^{\rm MC}_{\rm pri}(\Delta\eta,\Delta\phi)$ is compared to $R^{\rm MC}_{\rm pri,acc}(\Delta\eta,\Delta\phi)$. A χ^2 test is used to extract a scaling correction factor, A (which is associated with the minimum χ^2 as shown in Fig. 7.7(a)), for each vertex bin:

$$\chi^2 = \int \frac{[R^{\rm MC}_{\rm pri}(\Delta\eta,\Delta\phi) - A\times R^{\rm MC}_{\rm pri,acc}(\Delta\eta,\Delta\phi)]^2}{\sigma^{\rm MC}_{\rm pri}(\Delta\eta,\Delta\phi)\times A\times\sigma^{\rm MC}_{\rm pri,acc}(\Delta\eta,\Delta\phi)}\, d\Delta\eta d\Delta\phi \tag{7.3}$$

where $\sigma^{\rm MC}_{\rm pri}(\Delta\eta,\Delta\phi)$ and $\sigma^{\rm MC}_{\rm pri,acc}(\Delta\eta,\Delta\phi)$ are the uncertainties of the correlation function $R^{\rm MC}_{\rm pri}(\Delta\eta,\Delta\phi)$ and $R^{\rm MC}_{\rm pri,acc}(\Delta\eta,\Delta\phi)$. This scaling factor, A, is independent of $\Delta\eta$ and $\Delta\phi$, and is found to vary between 1.3 and 1.5 over the vertex range used in this analysis. Fig. 7.7(b) illustrates the comparison in the case of 1-D $\Delta\eta$ correlation functions. A has been estimated using different event generators and turned out to be consistent within 3%.

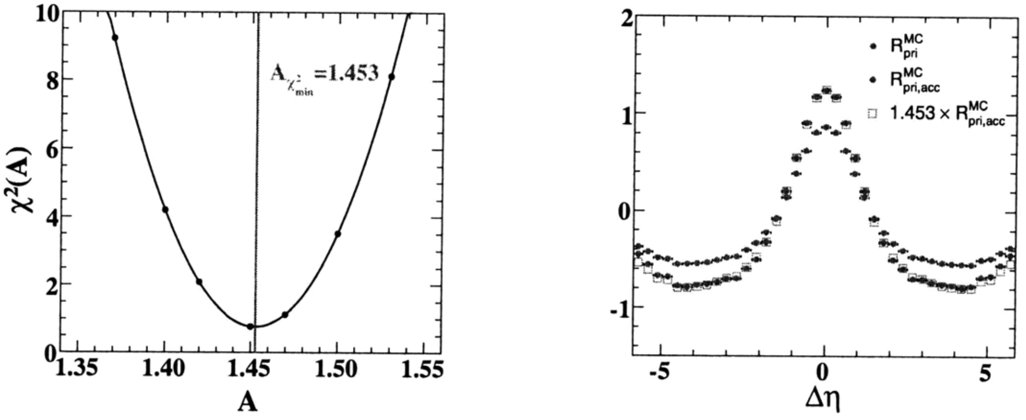

(a)

(b)

Figure 7.7: (a) χ^2 calculated from Eq. 7.3 with different acceptance scale factor A. The vertical line indicates the value of A which gives the minimum χ^2, $A_{\chi^2_{min}}$. (b) 1-D $\Delta\eta$ correlation functions for PYTHIA with primary tracks, primary tracks folded with PHOBOS acceptance, and primary tracks folded with PHOBOS acceptance but scaled by $A_{\chi^2_{min}}$ found in (a).

7.4 Vertex Averaged Final Correlation Function

After applying all the corrections, the result obtained in each small vertex bin, $R_{\text{final}}^{\text{data,vtx}}(\Delta\eta,\Delta\phi)$, is averaged over the entire vertex range:

$$< R_{\text{final}}^{\text{data}}(\Delta\eta,\Delta\phi) >= \frac{\sum_{\text{vtx}} N_{\text{evt}}^{\text{vtx}} R_{\text{final}}^{\text{data,vtx}}(\Delta\eta,\Delta\phi)}{\sum_{\text{vtx}} N_{\text{evt}}^{\text{vtx}}} \tag{7.4}$$

where $N_{\text{evt}}^{\text{vtx}}$ is the number of events in a particular vertex bin. This last step gives the final result of the two-particle correlation function in the data.

7.5 Systematic Errors

The systematic uncertainty related to the correction procedure has been mentioned above in Sect. 7.3, which is approximately 5%, the same for p+p, Cu+Cu and Au+Au collisions. It is quoted as the "scale" errors (presented as shaded bands in the final results) in the sense that all the points of the correlation function tend to be scaled up and down in a correlated fashion within the errors. In addition, other "point-to-point" systematic uncertainties are calculated by varying the vertex position and hit energy

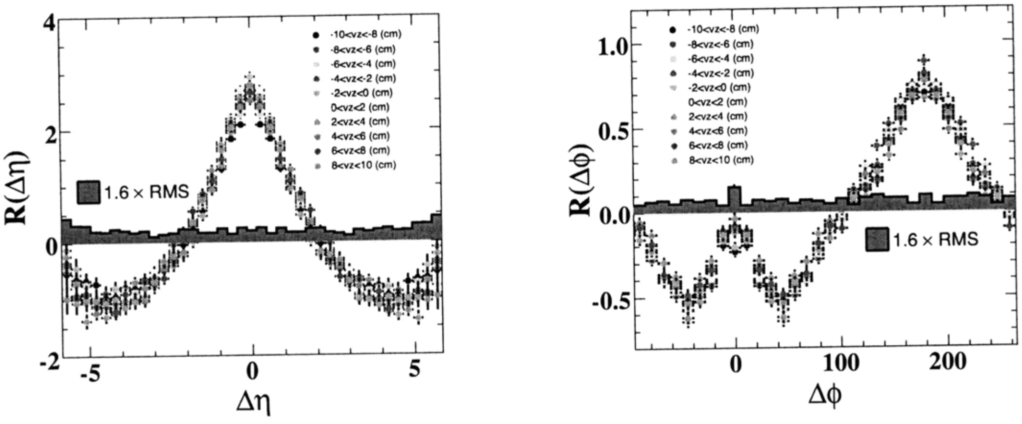

(a)

(b)

Figure 7.8: Corrected 1-D two-particle (a) $\Delta\eta$ and (b) $\Delta\phi$ correlation functions for 10 vertex bins in p+p collisions at $\sqrt{s} = 200$ GeV. The filled histogram indicates the systematic errors induced from the vertex position dependency.

threshold cuts, and comparing different occupancy correction methods for A+A collisions.

For each selection of parameters, a set of correlation functions are constructed under different conditions (i.e. 10 different vertex positions), and fully corrected using the MC procedure described above. The RMS of these correlation functions is calculated as an estimate of the systematic error from each particular source. The systematic errors due to the vertex position dependency, hit threshold cuts and occupancy correction method are added in quadrature to get the total RMS for each bin in $\Delta\eta$ and $\Delta\phi$. The vertex position dependency turns out to be the dominant source of the uncertainties in p+p collisions, and contribute almost equally to the occupancy correction method in A+A collisions. The final systematic uncertainties are quoted as 90% C.L.(1.6 × RMS).

7.5.1 Vertex Position Variation

Since the acceptance of our detector is strongly dependent on vertex position, any systematic uncertainties due to acceptance and geometrical description should manifest themselves as a dependence of the final results on vertex position. In Fig. 7.8, the fully corrected 1-D two-particle $\Delta\eta$ and $\Delta\phi$ correlation functions for all 10 vertex bins in p+p collisions are shown. 1.6× RMS of 10 correlations functions are calculated for each bin (filled histogram), which is roughly 6% relative to the overall scale. In A+A collisions,

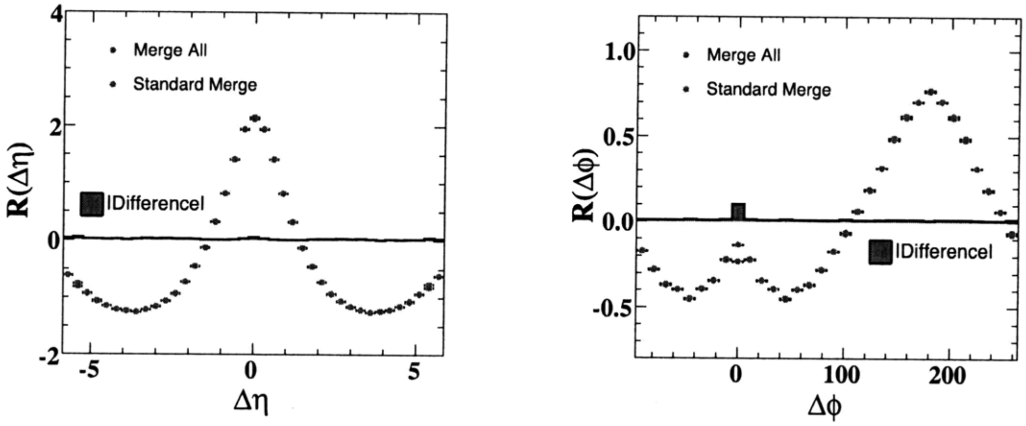

(a)

(b)

Figure 7.9: Corrected 1-D two-particle (a) $\Delta\eta$ and (b) $\Delta\phi$ correlation functions, compared between standard merging and merging all adjacent pads in p+p collisions at $\sqrt{s} = 200$ GeV. The filled histogram indicates the systematic errors induced from the hit reconstruction and merging procedure.

the errors from this source are comparable to that in p+p.

7.5.2 Hit Reconstruction and Merging

The threshold cuts in hit merging algorithm are used to reject noise or background hits, discriminate between isolated primary particles and ones that share their energies among adjacent pads. A variation of the thresholds allows us to test the impact of the hit reconstruction procedure on the final results.

Two types of hit merging setups are investigated and compared:

- Standard hit merging with parameters listed in Table 5.1, used in A+A collisions.
- *Merge High Threshold* is set to infinity such that all hits in adjacent pads are merged, used in p+p collisions.

In p+p collisions (see Fig. 7.9), the difference between the two setups is negligible, except for the bin at $\Delta\eta = 0$ and $\Delta\phi = 0$, a region sensitive to hits that are very close to each other (i.e. in adjacent pads). The effect is expected to be larger in A+A since merging all close hits will definite lose significant fraction (depending on multiplicity) of primary particles. However, it is compensated partially by the occupancy correction, which recovers the true number of particles on each pad based on the merged deposited energy,

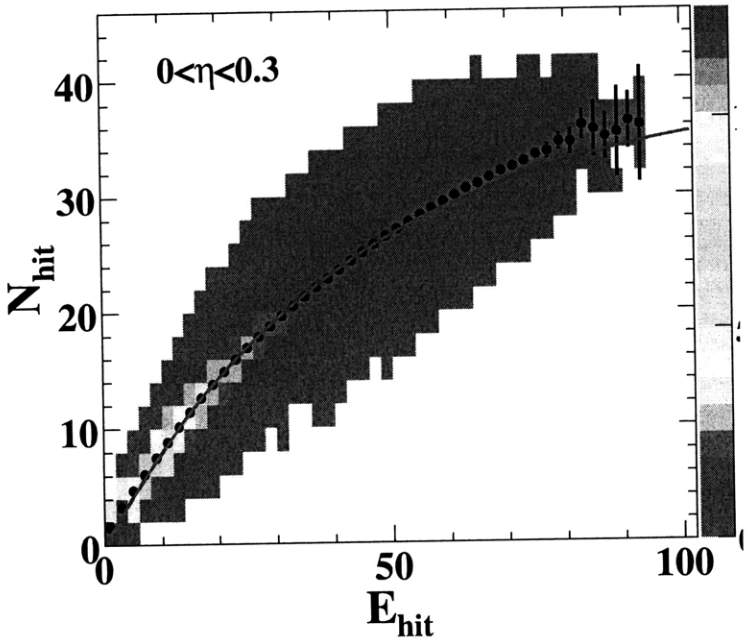

Figure 7.10: Total number of hits (N_{hit}) v.s. total normalized energy loss (E_{hit}) for $0.0 < \eta < 0.3$ in Au+Au collisions at $\sqrt{s_{NN}} = 200$ GeV. The solid curve corresponds the fit by Eq. 7.5.

and thus still not a dominant source of systematic errors compared to others. To be conservative, the full difference of the correlation functions between these two hit merging methods are included as part of the final systematic uncertainties.

7.5.3 Occupancy Correction

In order to evaluate the effectiveness of the occupancy correction developed in this thesis, the results from another semi-analog method used in the Forward-Backward correlation analysis are compared.

The basic idea is that by plotting the total number of hits (N_{hit}) v.s. total normalized energy loss (E_{hit}) in a give η bin (Fig. 7.10), a fit is performed according to the Poisson statistics:

$$N_{hit} = N_{hit}^{max}(1 - \exp(-\frac{E_{hit}}{E_{hit}^{max}})) \tag{7.5}$$

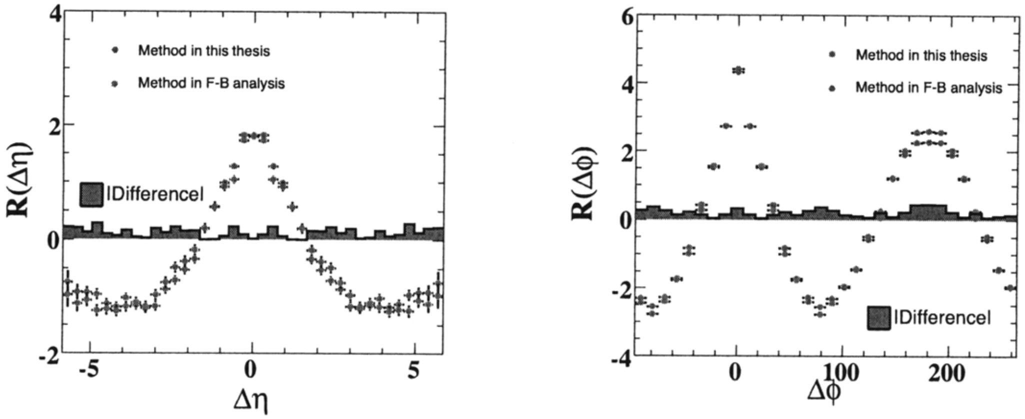

(a)

(b)

Figure 7.11: Corrected 1-D two-particle (a) $\Delta\eta$ and (b) $\Delta\phi$ correlation functions, with occupancy correction method compared between the one developed in this thesis and that used in the Forward-Backward correlation analysis, in the most central 3% Au+Au collisions at $\sqrt{s_{\rm NN}} = 200$ GeV. The filled histogram indicates the systematic errors induced from the occupancy correction method.

where N_{hit}^{max} and E_{hit}^{max} are the fit parameters. The ratio $\frac{E_{hit}^{max}}{N_{hit}^{max}}$ is indeed the slope parameter of the curve in the limit of $N_{hit} \to 0$, which corresponds to the average normalized energy loss per real particle. A semi-analog occupancy weighting factor f^{occ} thus can be estimated using the actual normalized energy loss per hit, $\frac{E_{hit}}{N_{hit}}$, compared to that per particle, $\frac{E_{hit}^{max}}{N_{hit}^{max}}$:

$$f^{occ} = \frac{E_{hit}}{N_{hit}} / \frac{E_{hit}^{max}}{N_{hit}^{max}} \tag{7.6}$$

which represents the actual number of particles hitting the detector. In the original method, f^{occ} is only estimated as a function of η since on average the occupancy is uniform in ϕ. This is, however, not the case if considered event-by-event due to the presence of elliptic flow. In two-particle correlation analysis, factor f^{occ} has to be extracted as a function of both η and ϕ so that the local occupancy is appropriately corrected and right magnitude of flow modulation in ϕ is recovered. Comparison of the final results between the new method in this thesis and semi-analog method in F-B correlation analysis can be found in Fig. 7.11 for the most central 10% Au+Au events, where the occupancy effect is expected to be most prominent. The difference between the two for each bin is considered as an additional source of systematic errors in A+A collisions.

8 Results and Physics Discussion

Final results on two-particle angular correlations in p+p ($\sqrt{s}$ = 200 and 410 GeV), Cu+Cu and Au+Au collisions ($\sqrt{s_{\mathrm{NN}}}$ = 200 GeV) over a very broad acceptance in $\Delta\eta$ and $\Delta\phi$ are presented in this Chapter. The observed two-dimensional (2-D) correlation structure shows a complex correlation structure in the hadronic final state (see Sect. 8.1), which has a natural interpretation in the concept of "cluster" emission.

After reviewing the general idea of cluster model developed in the middle of 1970s, a simple Independent Cluster Model (ICM) is implemented using Monte Carlo and shown to well describe the qualitative feature of the data in Sect. 8.2. The observed short-range correlations in $\Delta\eta$ are parameterized in terms of the effective cluster size and decay width.

In Sect. 8.3, the properties of clusters are systematically studied in p+p collisions as a function of collision energy and event multiplicity as an essential baseline measurement to the more complex heavy ion system. Moving on to Cu+Cu and Au+Au collisions, the extracted cluster size and decay width are presented as a function of system size. Furthermore, by separating clusters into near-side ($0° < \Delta\phi < 90°$) and away-side ($90° < \Delta\phi < 180°$), more detailed information on the properties of the clusters in the heavy ion collisions is obtained.

Finally, the effect of limited η acceptance on the cluster parameters is also addressed. Extrapolating limited acceptance ($|\eta| < 3$) to full phase space using MC models, cluster properties unbiased by detector acceptance are estimated. This comprehensive analysis of cluster properties in p+p and A+A collisions should provide useful information for understanding the hadronization stage, but may also give insight into physics relevant at much earlier times.

Results in this thesis have been first shown in *Quark Matter* — International Conference on Ultra-Relativistic Nucleus-Nucleus Collisions — in 2006 [110] and 2008 [111], and also published in *Phys. Rev. C* [112, 113].

8.1 2-D Correlation Structures

8.1.1 Correlation Structure in proton-proton Collisions

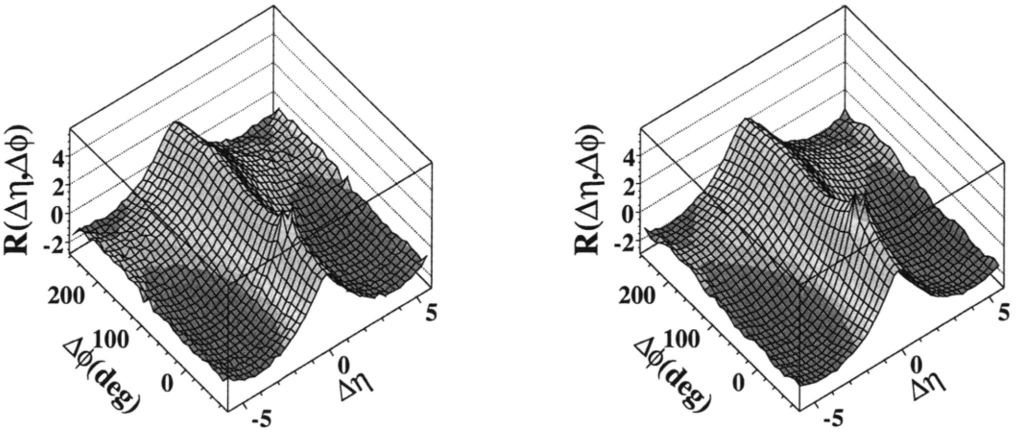

(a) p+p 200 GeV

(b) p+p 410 GeV

Figure 8.1: Two-particle angular correlation function in $\Delta\eta$ and $\Delta\phi$ in p+p collisions at $\sqrt{s} = 200$ GeV and 410 GeV (regions of $|\Delta\eta| < 0.15$ and $|\Delta\phi| < 5.625°$ are excluded) [112].

The final two-particle inclusive correlation functions in p+p collisions, averaged over 10 vertex bins, are shown as a function of $\Delta\eta$ and $\Delta\phi$ at $\sqrt{s} = 200$ GeV (Fig. 8.1(a)) and 410 GeV (Fig. 8.1(b)) [112]. The near-side hole corresponds to the excluded region of $|\Delta\eta| < 0.15$ and $|\Delta\phi| < 5.625°$. The systematic uncertainties in the absolute value of R($\Delta\eta$,$\Delta\phi$) are of the order of 0.3, relative to a peak value of 5, with little $\Delta\eta$ or $\Delta\phi$ dependence.

The complex 2-D correlation structure shown in Fig. 8.1 is approximately Gaussian in $\Delta\eta$ and persists over the entire $\Delta\phi$ range, becoming broader toward larger $\Delta\phi$ (which will be discussed in quantitative detail below). Similar structures also exist in PYTHIA (Fig. 6.2) though they do not reproduce the full strength of the short-range rapidity correlations seen in the data. The qualitative features of the observed correlation structure are consistent with an independent cluster approach according to a simulation study from the ISR experiment using a low-mass resonance (ρ,ω,η) gas model [109]. A more general MC implementation of the independent cluster model is developed in this thesis (see Sect. 8.2.2). The excess of the near-side peak ($\Delta\eta \sim 0$ and $\Delta\phi \sim 0$) relative to the away-side could be partially a result of the HBT effect [114]. This possibility is investigated in the Appendix E using a simple MC model and found to be negligible for the cluster properties investigated in the later sections.

8.1.2 Correlation Structure in Heavy Ion Collisions

Similarly to p+p, the final 2-D two-particle inclusive correlation functions for charged particles in Cu+Cu and Au+Au collisions after all corrections are shown in Fig. 8.2 as a function of $\Delta\eta$ and $\Delta\phi$ for the five centrality classes (40%-50%, 30%-40%, 20%-30%, 10%-20%, 0%-10%) at $\sqrt{s_{_{NN}}} = 200$ GeV. The cluster-like short-range correlation structure in $\Delta\eta$ is also observed over the whole $\Delta\phi$ range in A+A as seen in p+p. Compared to p+p collisions at the same energy in Sect. 8.1.1, heavy ion collisions show not only the cluster-like structure, but also a $\cos(2\Delta\phi)$ modulation due to elliptic flow [115]. Note that the magnitude of flow seen in the correlation function is

$$\langle (n-1)v_2^2 \rangle,$$

by definition. This explains why there seems to be much larger flow signal in more central A+A collisions.

To subtract off the v_2 component and study the cluster-like correlation structure directly in 2-D is a highly non-trivial task. First of all, the magnitude of v_2 varies significantly over a large range of η which requires an η-dependent description of flow modulation in the two-particle correlation function. Most importantly, the measurement of v_2 from the standard method (which is often used for flow subtraction from two-particle correlation function) is in general affected by cluster-like correlations, or so-called "non-flow" effects. In STAR, a similar analysis of inclusive two-particle correlations was performed in a much smaller η acceptance ($|\eta| < 1$) [116], which attempted to decompose the 2-D correlation structure into a minimum set of physics sub-components including a v_2 term assumed to be constant within $|\eta| < 1$. Some interesting features of centrality dependence of various components were observed. Taking the advantage of a large η coverage, an on-going analysis at PHOBOS is dedicated to studying the non-flow effects in flow fluctuation measurement using the two-particle correlation technique developed in this thesis [117].

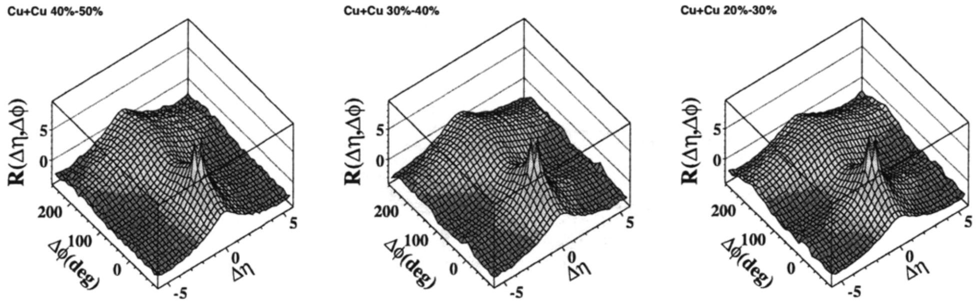

(a) Cu+Cu 40%-50%　(b) Cu+Cu 30%-40%　(c) Cu+Cu 20%-30%

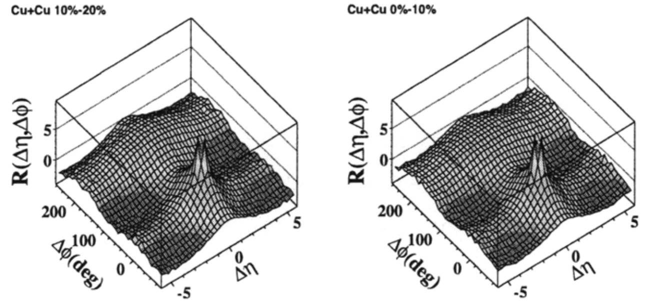

(d) Cu+Cu 10%-20%　(e) Cu+Cu 0%-10%

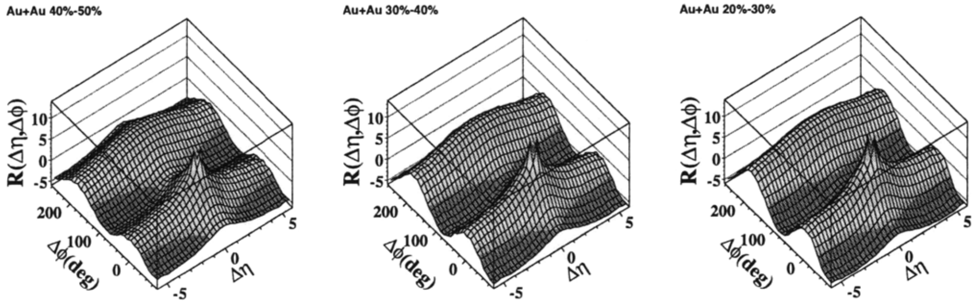

(f) Au+Au 40%-50%　(g) Au+Au 30%-40%　(h) Au+Au 20%-30%

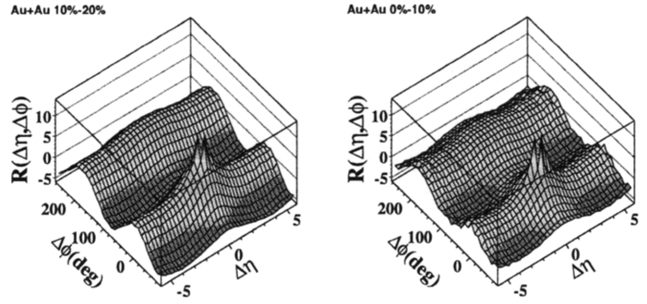

(i) Au+Au 10%-20%　(j) Au+Au 0%-10%

Figure 8.2: Two-particle angular correlation functions in $\Delta\eta$ and $\Delta\phi$ in Cu+Cu and Au+Au collisions for five centrality classes at $\sqrt{s_{\mathrm{NN}}} = 200$ GeV (regions of $|\Delta\eta| < 0.15$ and $|\Delta\phi| < 5.625°$ are excluded) [113].

8.2 Independent Cluster Emission Model

8.2.1 Concept of Cluster Emission

The idea that hadrons are produced in clusters, rather than individually, has had great success in describing many features of multiparticle production in high energy hadronic collisions [109, 118–121]. In a scenario of independent cluster emission, clusters are formed before the final-state hadrons and are independently emitted according to a dynamically generated distribution in η and ϕ. The clusters subsequently decay isotropically in their own rest frame into the observed final-state hadrons. The postulate of independent emission of isotropic clusters has been widely applied to reproduce the observed positive, short-range characteristics of inclusive two-particle correlations [109, 118–122]. where the observed correlation strength and extent in phase space can be parameterized in terms of the cluster multiplicity, or "size" (the average number of particles in a cluster) and the decay "width" (the separation of the particles in pseudorapidity). However, it should be noted that independent cluster emission is only a phenomenological approach which provides no insight as to the mechanisms by which clusters are formed. Further modeling is required to connect these studies to the underlying QCD dynamics.

A related measurement, studying the forward-backward multiplicity correlations, was performed in Au+Au collisions at center of mass energy per nucleon pair ($\sqrt{s_{\rm NN}}$) of 200 GeV using the PHOBOS detector at the RHIC [106]. The event-by-event observable $C = (N_F - N_B)/\sqrt{N_F + N_B}$ is constructed, where N_F and N_B are defined to be the total multiplicity in two symmetric regions forward and backward of mid-rapidity. The variance (σ_C^2), which is related to the cluster size, was measured. An effective cluster size of approximately 2-3, increasing with the size of the pseudorapidity window, was observed. In heavy ion collisions at RHIC, it has been predicted that the formation of a Quark Gluon Plasma (QGP) could modify cluster properties relative to p+p collisions [123]. Unfortunately, the method used in Ref. [106] was found to have intrinsic limitations for measuring the properties of clusters emitted near mid-rapidity. This makes direct tests of these predictions difficult and suggests a need for different methods to access cluster properties directly.

8.2.2 Monte Carlo Implementation

A Monte Carlo simulation of the Independent Cluster Model (ICM) is realized in the analysis of this thesis based on the simple assumption of isotropic decay of the clusters. In our ICM approach, for each event clusters are generated, each with a given mass, transverse momentum (p_T) and longitudinal momentum ($p_\parallel$). The cluster decays isotropically in its rest frame into K particles (assumed to be pions) constrained by the available phase space (This is realized by a ROOT class `TGenPhaseSpace`).

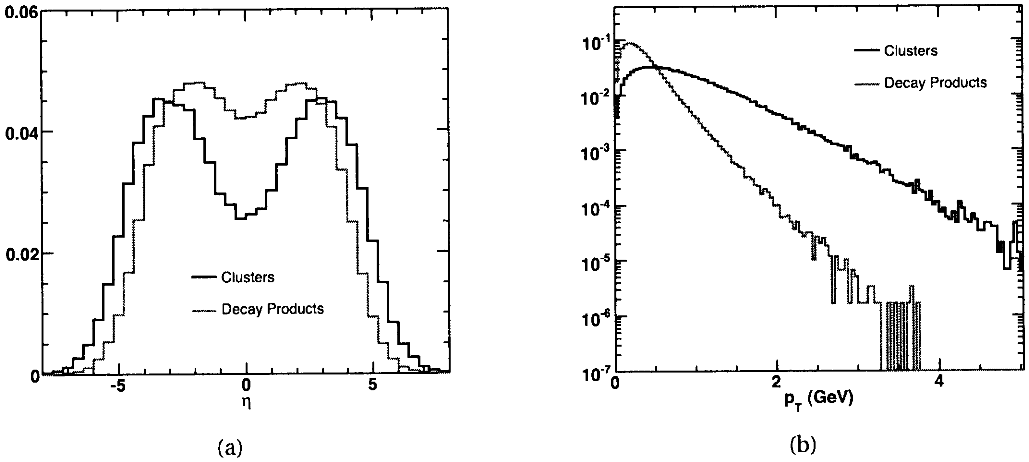

Figure 8.3: (a) $dN/d\eta$ and (b) dN/dp_T distributions for clusters (red) and their decay products (black) in the Independent Cluster Model (ICM).

The mass of the clusters is taken to be $0.35 \times K$ (GeV/c^2). The p_T and $p_\parallel$ of the clusters are drawn from distributions according to the functional forms:

$$\frac{dN}{dp_T} \sim p_T \times \exp(-p_T/\overline{p_T})$$

$$\frac{dN}{dp_\parallel} \sim \frac{a_1}{\cosh(p_\parallel/b_1)} + \frac{a_2}{\cosh(p_\parallel/b_2)} + \frac{a_3}{\cosh(p_\parallel/b_3)}$$

and have always been tuned to match the measured $dN/d\eta$ and dN/dp_T spectra for final state inclusive charged particles [70, 124, 125]. In addition, the global momentum of the clusters is always conserved event-by-event in order to preserve the $\cos(\Delta\phi)$ component typically seen in the 2-D correlation function of p+p collisions (e.g. in Fig. 8.1).

In Fig. 8.4, an example of a 2-D two-particle correlation function derived from ICM is shown with $K = 3$ measured in an acceptance of $|\eta| < 3$, same as the PHOBOS Octagon. It shows a qualitatively similar structure to what's observed in p+p collisions (see Fig. 8.1), a Gaussian shape short-range correlation along $\Delta\eta$ which gets wider going from near-side ($\Delta\phi \sim 0°$) to away-side ($\Delta\phi \sim 180°$). This observed complex correlation structures (also in data) can be understood in a scenario of cluster emission. The narrower hump in the near-side ($\Delta\phi \sim 0°$) part of the correlation function can be understood as the contributions primarily from higher p_T clusters because their decay products are highly Lorentz boosted along the cluster momentum direction and thus closer to each other, as well as from many-body decays [109]. On the other hand, the broader away-side generally arises from the decay of clusters with lower p_{T}.

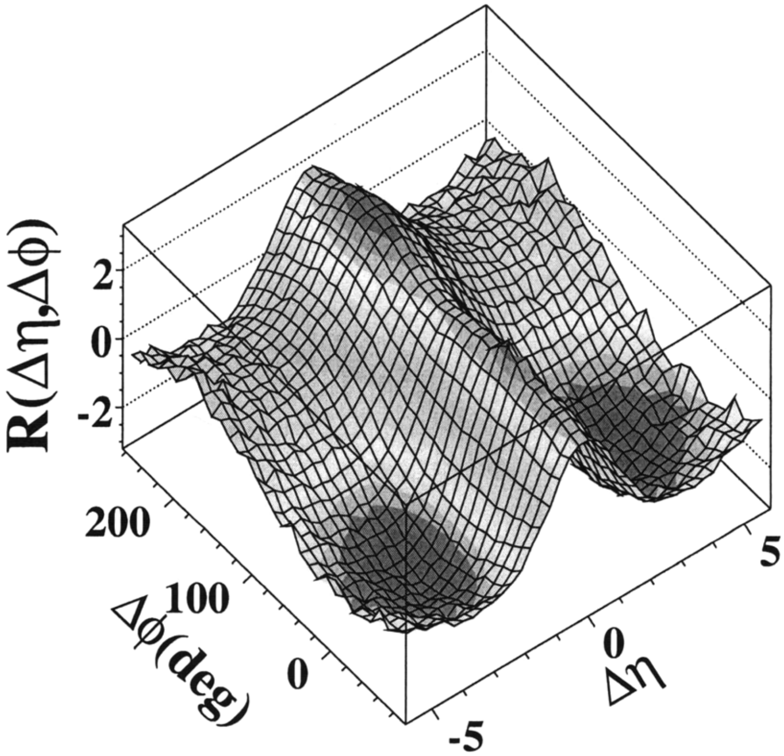

Figure 8.4: Two-particle correlation function in $\Delta\eta$ and $\Delta\phi$ for ICM with $K = 3$ and $\gamma = 0$.

8.3 Cluster Properties from 1-D Pseudorapidity Correlation Functions

8.3.1 Extract Cluster Parameters

In the context of an independent cluster emission model, the properties of clusters can be parameterized in terms of effective cluster size and decay width from two-particle pseudorapidity correlation function (defined in Eq. 6.7). The formalism is deduced following a similar way to Ref. [122].

Assume that in an n body event, c clusters are produced with a probability distribution of $P(c)$. For each cluster, it decays into K_i (i=1,2,...c) particles, which gives the relation:

$$\sum_{i=1}^{c} K_i = n$$

. Now let $\Gamma(\eta_1,\eta_2)$ be the probability density function of two particles present in the same cluster having pseudorapidity η_1 and η_2, and assumed to be independent of K_i and c.

Recall that in Sect. 6.1, the single- and two-particle pseudorapidity density with certain event multiplicity n are expressed as:

$$\rho_n^I(\eta) \equiv \frac{1}{n\sigma_n}\frac{d\sigma_n}{d\eta}.$$

$$\rho_n^{II}(\eta_1,\eta_2) \equiv \frac{1}{n(n-1)\sigma_n}\frac{d^2\sigma_n}{d\eta_1 d\eta_2}$$

with normalization relations:

$$\int \rho_n^I(\eta)d\eta = 1$$

$$\int \rho_n^{II}(\eta_1,\eta_2)d\eta_1 d\eta_2 = 1$$

where σ_n denotes the cross section of observing events with n charged particles.

In the context of cluster scenario, the two-particle density $\rho_n^{II}(\eta_1,\eta_2)$ can be constructed as a sum of two independent terms:

$$\rho_n^{II}(\eta_1,\eta_2)=\frac{1}{n(n-1)}\sum_{c=1}^{n}P(c)\{\sum_{i=1}^{c}K_i(K_i-1)\Gamma(\eta_1,\eta_2)+\sum_{i\neq j=1}^{c}K_iK_j\rho_n^I(\eta_1)\rho_n^I(\eta_2)\}. \quad (8.1)$$

where, for the first term on the right hand side, it represents the contributions of two-particle pairs within the same cluster, whereas the second term corresponds to all possible ways of finding two particles in two different clusters. It thus simply proportional to a product of two single-particle density distributions. It is convenient to rearrange Eq. 8.1 further to the following form:

$$\rho_n^{II}(\eta_1,\eta_2)=\frac{1}{n-1}[n\rho_n^I(\eta_1)\rho_n^I(\eta_2)-\Gamma(\eta_1,\eta_2)]+\frac{1}{n-1}\frac{<K^2>}{<K>}[\Gamma(\eta_1,\eta_2)-\rho_n^I(\eta_1)\rho_n^I(\eta_2)] \quad (8.2)$$

where,

$$<K^2>=\sum_{c,N}P(c)(\sum_{i=1}^{c}K_c^2)/\sum_{c,N}cP(c)=\sum_{c,N}P(c)(\sum_{i=1}^{c}K^2)/<c>$$

$$<K>=\sum_{c,N}P(c)(\sum_{i=1}^{c}K)/\sum_{c,N}cP(c)=n/<c>$$

$\sum_{c,N}$ represents averaging over all the possible configuration of cluster as well as all the events.

In this way, the two-particle pseudorapidity correlation function can be expressed as:

$$\begin{aligned} R(\eta_1,\eta_2) &= \left\langle (n-1)\left(\frac{\rho_n^{II}(\eta_1,\eta_2)}{\rho_n^I(\eta_1)\rho_n^I(\eta_2)}-1\right)\right\rangle \\ &= \frac{<(K-1)K>}{<K>}\left[\frac{\Gamma(\eta_1,\eta_2)}{\langle\rho_n^I(\eta_1)\rho_n^I(\eta_2)\rangle}-1\right] \\ &= \alpha\left[\frac{\Gamma(\eta_1,\eta_2)}{\langle\rho_n^I(\eta_1)\rho_n^I(\eta_2)\rangle}-1\right]. \end{aligned} \quad (8.3)$$

By integrating over $\eta_1+\eta_2$ and only concentrating on the relative difference in pseudorapidity ($\Delta\eta$), the formalism of two-particle $\Delta\eta$ correlation function (defined in Eq. 6.7) is derived in the context of cluster emission model:

$$R(\Delta\eta) = \alpha\left[\frac{\Gamma(\Delta\eta)}{\rho^{\text{mixed}}(\Delta\eta)} - 1\right]. \tag{8.4}$$

The correlation strength α is a parameter containing information about the first two moments (mean and sigma) of the distribution of cluster size K. The function $\Gamma(\Delta\eta)$ is chosen to be a Gaussian function

$$\propto \exp[-(\Delta\eta)^2/(4\delta^2)]$$

with δ characterizing the correlation range in η space of particles produced by a single cluster. The background distribution $\rho^{\text{mixed}}(\Delta\eta)$ is just the distribution obtained by event-mixing introduced in Sect. 6.1. To correct for the holes in the PHOBOS acceptance, the ratio of the background are calculated for PYTHIA primary particles, $\rho^{\text{mixed}}_{\text{MC,pri}}(\Delta\eta)$, and compared to the one obtained in the full GEANT simulations, $\rho^{\text{mixed}}_{\text{MC,sim}}(\Delta\eta)$. The ratio is applied to the background calculated from the data, $\rho^{\text{mixed}}_{\text{data,raw}}(\Delta\eta)$, as a multiplicative factor:

$$\rho^{\text{mixed}}_{\text{data,final}}(\Delta\eta) = \frac{\rho^{\text{mixed}}_{\text{MC,pri}}(\Delta\eta)}{\rho^{\text{mixed}}_{\text{MC,sim}}(\Delta\eta)} \times \rho^{\text{mixed}}_{\text{data,raw}}(\Delta\eta). \tag{8.5}$$

In this way, the background distribution is independent of experimental setups.

The effective cluster size is defined via the relation:

$$K_{\text{eff}} = \alpha + 1 = \frac{\langle K(K-1)\rangle}{\langle K\rangle} + 1 = \langle K\rangle + \frac{\sigma_K^2}{\langle K\rangle}. \tag{8.6}$$

The δ parameter is equal to the width of the $\Delta\eta$ distribution of the particle pairs from the cluster. It is connected with another variable also characterizing the cluster width, σ_η (understood as the width of the distribution of the difference $\eta_{particle} - \eta_{cluster}$), by the formula: $\delta = \sqrt{\frac{K}{K-1}} \times \sigma_\eta$, for fixed K. The factor $\sqrt{\frac{K}{K-1}}$ difference is due to the fact that the average of $\eta_{particle}$ in a cluster is constrained to be conserved (equal to $\eta_{cluster}$). Of course, without direct knowledge of the distribution of K, the average cluster size $\langle K\rangle$ and width σ_η cannot be derived based on K_{eff} and δ. However, by a χ^2 fit of Eq. 8.4 to the measured two-particle pseudorapidity correlation function, the effective cluster size K_{eff} and width δ can be estimated.

A cluster model fit from Eq. 8.4 is performed to the two-particle pseudorapidity correlation function at full phase space for ICM with input $K = 3$, shown in Fig. 8.5 including the resulting fit parameters. As illustrated, Eq. 8.4 provides a good fit and successfully extracts the input cluster size in K_{eff}. The effect of limited η coverage (e.g. $|\eta| < 3$ at

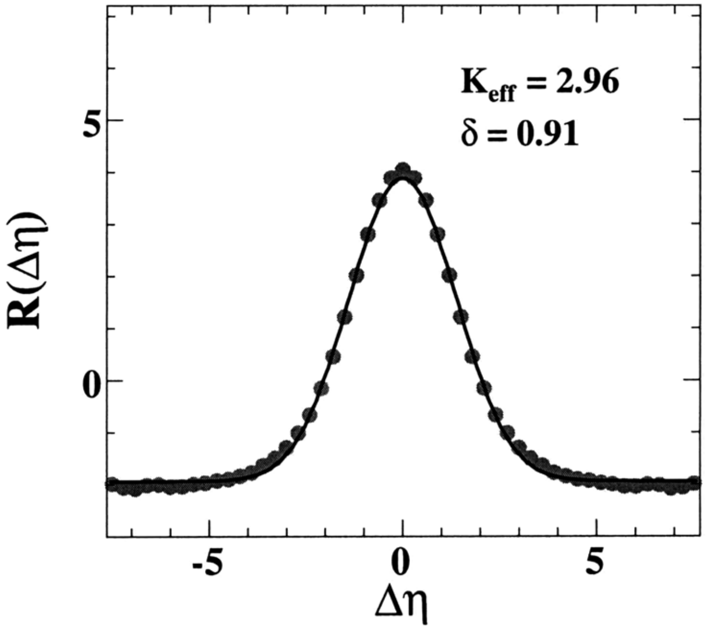

Figure 8.5: Two-particle $\Delta\eta$ correlation function at full phase space for ICM with input $K = 3$. The solid curve corresponds to the cluster model fit using Eq. 8.4.

PHOBOS) on the cluster parameters will be discussed in Sect. 8.4.

8.3.2 Cluster Properties in proton-proton Collisions

The two-particle pseudorapidity correlation function $R(\Delta\eta)$ in p+p collisions, averaged over the $\Delta\phi$ range from 0° to 180° and 10 vertex bins (-10 cm< z_{vtx} <10 cm), is shown in Fig. 8.6 at $\sqrt{s} = 200$ and 410 GeV. The error bars (also in Fig. 8.6 - 8.10) correspond to point-to-point systematic errors with 90% C.L. The error bands (also in Fig. 8.6 - 8.10) denote an overall scale error with 90% C.L. as an indication of the uncertainties in the correction method which tends to move all of the data points up and down in a correlated fashion. The statistical errors are negligible due to the large p+p event sample used in this analysis.

Correlation functions in bins of vertex are individually fit using Eq. 8.4 to extract the effective cluster size, K_{eff}, and the cluster decay width, δ. These results are then averaged over the vertex range to find the final results. The curve showing Eq. 8.4 with the final averaged values of the fit parameters is also displayed in Fig. 8.6 along with $R(\Delta\eta)$. The independent cluster model provides a good fit to the data over a large range in $\Delta\eta$,

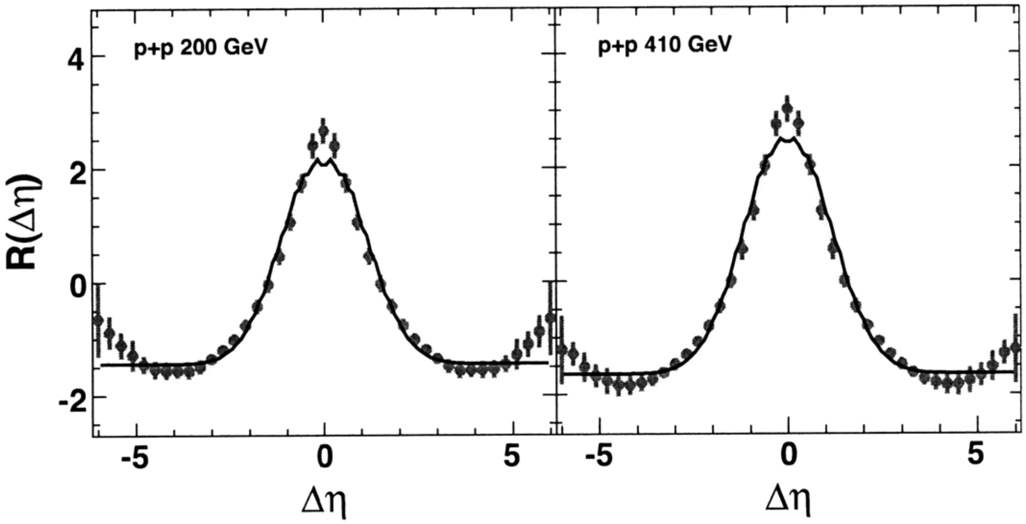

Figure 8.6: Two-particle $\Delta\eta$ correlation function, averaged over the $\Delta\phi$ range from 0° to 180°, in p+p collisions at $\sqrt{s}$ = 200 GeV (left) and 410 GeV (right). The solid curves correspond to the cluster model fits using Eq. 8.4 over the measured $\Delta\eta$ range, excluding the three points around $\Delta\eta$=0. The error bars and bands correspond to point-to-point systematic errors and overall scale errors respectively with 90% C.L. The statistical errors are negligible [112].

as shown in Fig. 8.6. An effective cluster size $K_{\text{eff}} = 2.44 \pm 0.08$ and width $\delta = 0.66 \pm 0.03$ for $\sqrt{s} = 200$ GeV and $K_{\text{eff}} = 2.66 \pm 0.10$, $\delta = 0.67 \pm 0.03$ for $\sqrt{s} = 410$ GeV are obtained with scale errors of 5% for K_{eff} and 3% for δ. The three most central points (a region of $|\Delta\eta| < 0.45$) in $R(\Delta\eta)$ are excluded from the fits mainly due to the large uncertainty stemming from residual detector effects, or perhaps other physics at this small scale in $\Delta\eta$. However, including them from the fit affects K_{eff} and δ by no more than 3%.

In Fig. 8.7, the PHOBOS data are compared with previous measurements of K_{eff} and δ as a function of $\sqrt{s}$. At lower ISR energies [109, 119], K_{eff} is approximately constant within error bars. At the higher SPS energies [118], UA5 finds K_{eff} to be larger than at the ISR, but with little energy dependence between 200 GeV and 900 GeV. The PHOBOS data are in good agreement with the UA5 measurements and, with much higher statistics in the p+p event sample, show a clear energy dependence of K_{eff}. By contrast, the cluster decay width δ remains almost constant over the full range of collision energies. The event generators, HIJING and PYTHIA, show a similar energy dependence of K_{eff} and δ to the data, but with a significantly lower magnitude of K_{eff}.

The observed cluster size cannot be fully explained by a resonance decay model

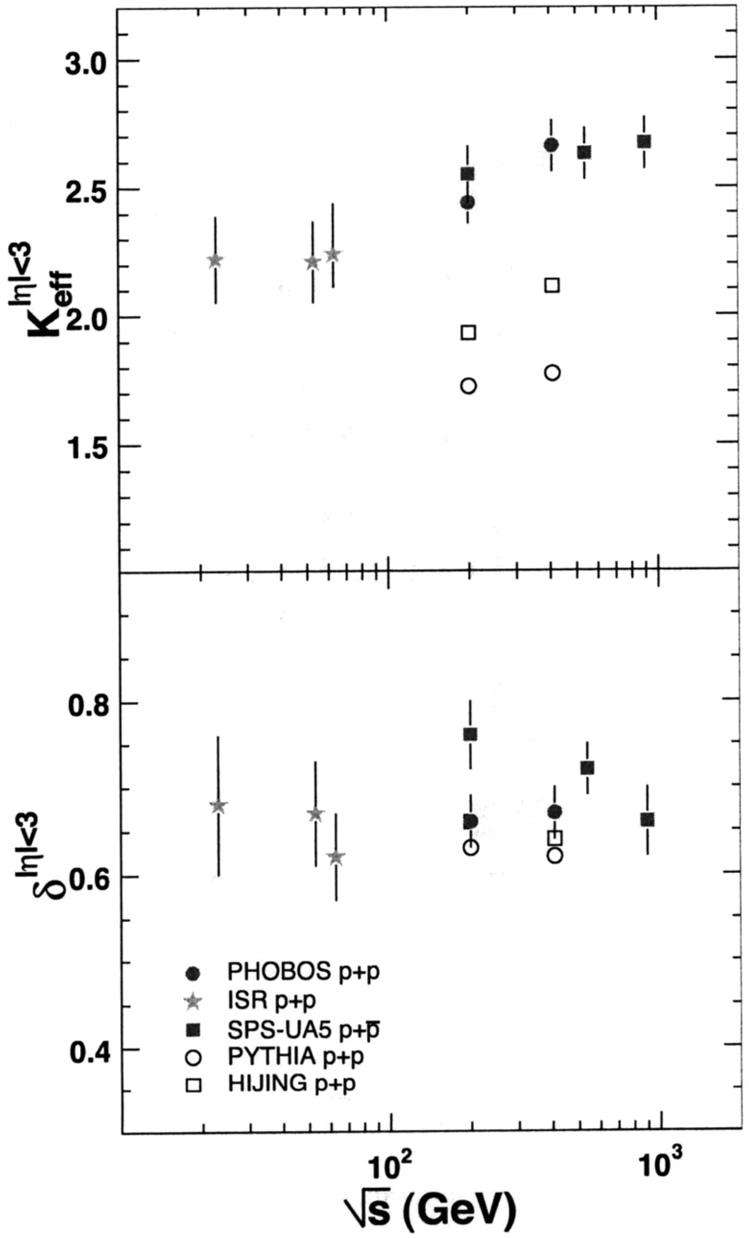

Figure 8.7: K_{eff} (top) and δ (bottom) as a function of $\sqrt{s}$ measured for $|\eta| < 3$ by PHOBOS in solid circles, as well as UA5 [118] (solid squares) and ISR [109, 119] (solid stars) experiments for p+p and p+p̄ collisions [112]. Open circles and squares show the PYTHIA and HIJING results respectively. The error representations are identical to those in Fig. 8.6.

even at very low energies, since the expectation of $\langle K\rangle$ from resonance decays is only about 1.5 (extrapolating to 1.7 for K_{eff} depending on the assumed cluster size distribution [118]). This is significantly lower than the observed values, but is close to what is seen in PYTHIA. The HBT effect, after averaging over $\Delta\phi$, would increase the cluster size by no more than 2% (see Appendix E). Additional sources of short-range correlations are needed to describe the data. As the energy increases, the onset of jets should play a more important role in the particle production giving bigger clusters, which could be the underlying cause for the observed energy dependence of K_{eff}. At the LHC, with p+p collision at $\sqrt{s} = 14$ TeV, jet-like particle production is expected to be dominant and should manifest itself in a further increase in the effective cluster size.

To gain further detailed information, the normalized cluster parameters, $K_{\mathrm{eff}}/\langle K_{\mathrm{eff}}\rangle$ and $\delta/\langle\delta\rangle$, are calculated as a function of the normalized charged multiplicity $n/\langle n\rangle$ at $\sqrt{s} = 200$ and 410 GeV (Fig. 8.8(a)). Scaled by the average charged multiplicity $\langle n\rangle$, the distribution of $n/\langle n\rangle$ turns out to be essentially identical for data and charged primary tracks from MC (PYTHIA and HIJING), despite the holes in the PHOBOS Octagon detector, a property known as Koba-Nielsen-Olesen (KNO) scaling [126]. By dividing the cluster parameters at different multiplicity by the averaged values, a scaling behavior is observed between two different energies in both data and MC. $K_{\mathrm{eff}}/\langle K_{\mathrm{eff}}\rangle$ increases with event multiplicity while $\delta/\langle\delta\rangle$ is found to be largely independent of it. PYTHIA and HIJING give a similar multiplicity dependence, but the increase in $K_{\mathrm{eff}}/\langle K_{\mathrm{eff}}\rangle$ is not as strong as in the data. Measurements from the ISR and UA5 experiments [109, 118, 119] are qualitatively consistent with PHOBOS, but significantly limited by statistics, and are thus not shown here.

To explicitly show the $\Delta\phi$ dependence of the short-range pseudorapidity correlation seen in Fig. 8.1, the $\Delta\phi$ range from 0° to 180° is divided into four regions and projected separately onto the $\Delta\eta$ axis. Fig. 8.8(b) shows $K_{\mathrm{eff}}/\langle K_{\mathrm{eff}}\rangle$ and $\delta/\langle\delta\rangle$ for different $\Delta\phi$ regions. $K_{\mathrm{eff}}/\langle K_{\mathrm{eff}}\rangle$ gradually decreases while δ increases as one goes from small to large $\Delta\phi$ region. This might reflect some information about the transverse momentum distribution of the clusters [109]. High p_{T} clusters should generally contribute to a narrow hump in the near-side (near $\Delta\phi = 0°$) of the correlation function in Fig. 8.1, whereas the broader away-side (near $\Delta\phi = 180°$) comes from clusters with lower transverse momentum. Again, PYTHIA and HIJING are qualitatively similar to data but show a smaller decay width at intermediate $\Delta\phi$ and a larger decay width near $\Delta\phi = 180°$.

The two-particle azimuthal correlation functions $R(\Delta\phi)$, averaged over a broad range of $\Delta\eta$ from 0 to 6, in p+p collisions at $\sqrt{s} = 200$ and 410 GeV are presented in Fig. 8.9.

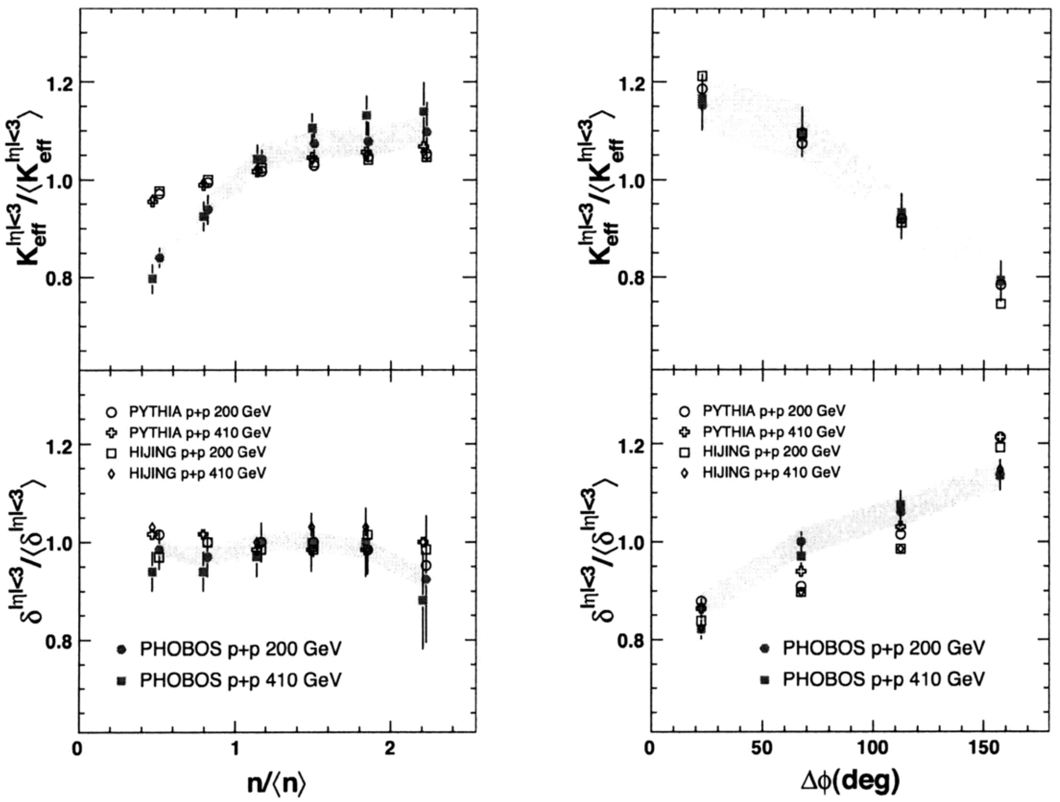

(a) (b)

Figure 8.8: Normalized effective cluster size $K_{\text{eff}}/\langle K_{\text{eff}}\rangle$ (top) and decay width $\delta/\langle\delta\rangle$ (bottom) as a function of normalized multiplicity (a) $n/\langle n\rangle$ and (b) $\Delta\phi$ in p+p collisions at $\sqrt{s} = 200$ and 410 GeV measured for $|\eta| < 3$ by PHOBOS (solid symbols), as well as MC studies (open symbols) [112]. The error representations are identical to those in Fig. 8.6.

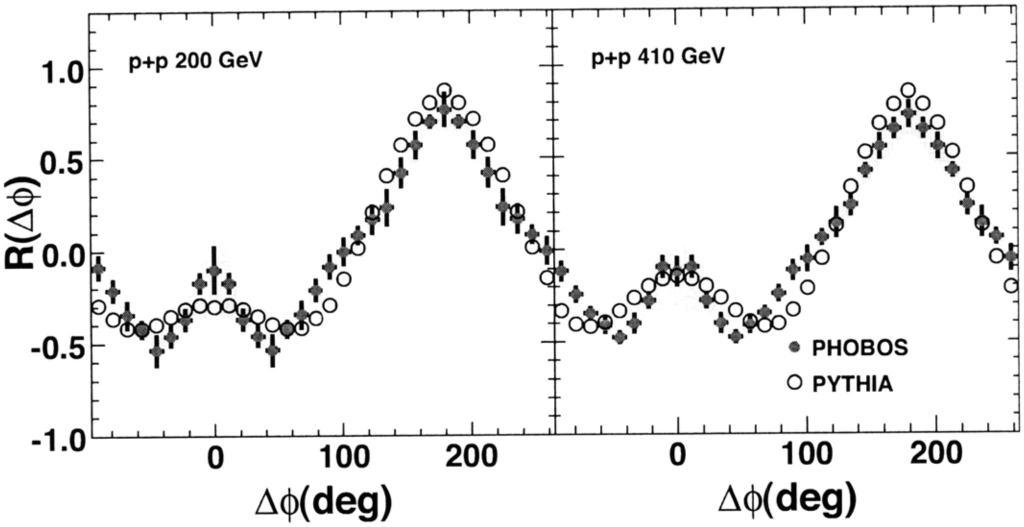

Figure 8.9: Two-particle azimuthal correlation function, averaged over the $\Delta\eta$ range from 0 to 6, in p+p collisions at $\sqrt{s} = 200$ GeV (left) and 410 GeV (right) from PHOBOS (solid circles), as well as MC studies (open circles) [112]. The error representations are identical to those in Fig. 8.6.

$R(\Delta\phi)$ (defined in Eq. 6.8) is obtained using a procedure similar to that shown for $R(\Delta\eta)$. The observed asymmetric structure in $\Delta\phi$ (with the $\Delta\eta$-averaged away-side peak larger than the near-side peak) could also provide some information about the momentum and size distribution of clusters. The $\Delta\eta$ integrated correlation function is similar in magnitude both for data and PYTHIA, despite the significant difference in the extracted K_{eff}. More detailed modeling of the cluster properties is needed to fully explain many aspects of the complex two-particle correlation function.

8.3.3 Cluster Properties in Heavy Ion Collisions

Just as for p+p, the 2-D correlation function is integrated over $\Delta\phi$ to give the 1-D $\Delta\eta$ correlation function $R(\Delta\eta)$ in Cu+Cu and Au+Au collisions, shown in Fig. 8.10. This allows a quantitative study of cluster properties in pseudorapidity space, with the elliptic flow contribution averaging to zero. $R(\Delta\eta)$ is again fitted to a functional form derived in Eq. 8.4 in the cluster model. Again, the three most central points (a region of $|\Delta\eta| < 0.45$) in $R(\Delta\eta)$ are excluded from the fits because of the big uncertainties. As one can see from Fig. 8.10, even without any fit, there already shows some centrality evolution of $R(\Delta\eta)$ in heavy ion systems.

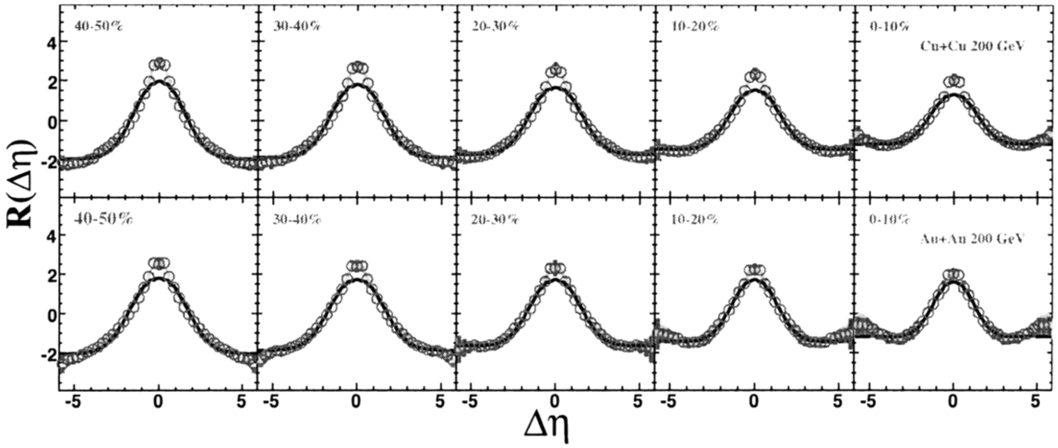

Figure 8.10: Two-particle $\Delta\eta$ correlation function, averaged over the $\Delta\phi$ range from 0° to 180°, in Cu+Cu (upper row) and Au+Au (lower row) collisions for five different centrality classes at $\sqrt{s_{\rm NN}} = 200$ GeV [113]. The solid curves correspond to the cluster model fits using Eq. 8.4 over the measured $\Delta\eta$ range, excluding the three points around $\Delta\eta$=0. The error representations are identical to those in Fig. 8.6.

Results on effective cluster size ($K_{\rm eff}$) and decay width (δ) for $|\eta| < 3$ as a function of the fractional cross section, $1 - \sigma/\sigma_0$ (defined in Sect. 4.4), are shown in Fig. 8.11 for Cu+Cu and Au+Au collisions at $\sqrt{s_{\rm NN}} = 200$ GeV. Moving from left to right in Fig. 8.11, the collision becomes more central. The systematic uncertainties are estimated using a similar procedure to p+p collisions [112] with an additional contribution from the occupancy corrections. The overall scale error, common to both Cu+Cu and Au+Au, is 5% for both $K_{\rm eff}$ and δ in inclusive and away-side data. The near-side data has a slightly smaller overall scale error of 3% for both $K_{\rm eff}$ and δ. The shaded band indicates the value found in $\sqrt{s} = 200$ GeV p+p collisions, which suggests that the cluster properties are similar in p+p and A+A systems. This implies that the phenomenological properties of hadronization appear to be similar in p+p and A+A. However, an increase of both the effective cluster size and decay width is observed going from p+p to peripheral A+A systems. Toward more central collisions, it is also observed that the effective cluster size systematically decreases with increasing collision centrality in both Cu+Cu and Au+Au collisions, whereas the cluster decay width is approximately constant over the whole centrality range within the systematic uncertainties. Furthermore, by comparing the two systems at the same fraction of the inelastic cross section (which is related to the ratio of impact parameter to the nuclear radius, $b/2R$), a "geometric scaling" feature is revealed, which shows a similar effective cluster size at the same collision geometry of

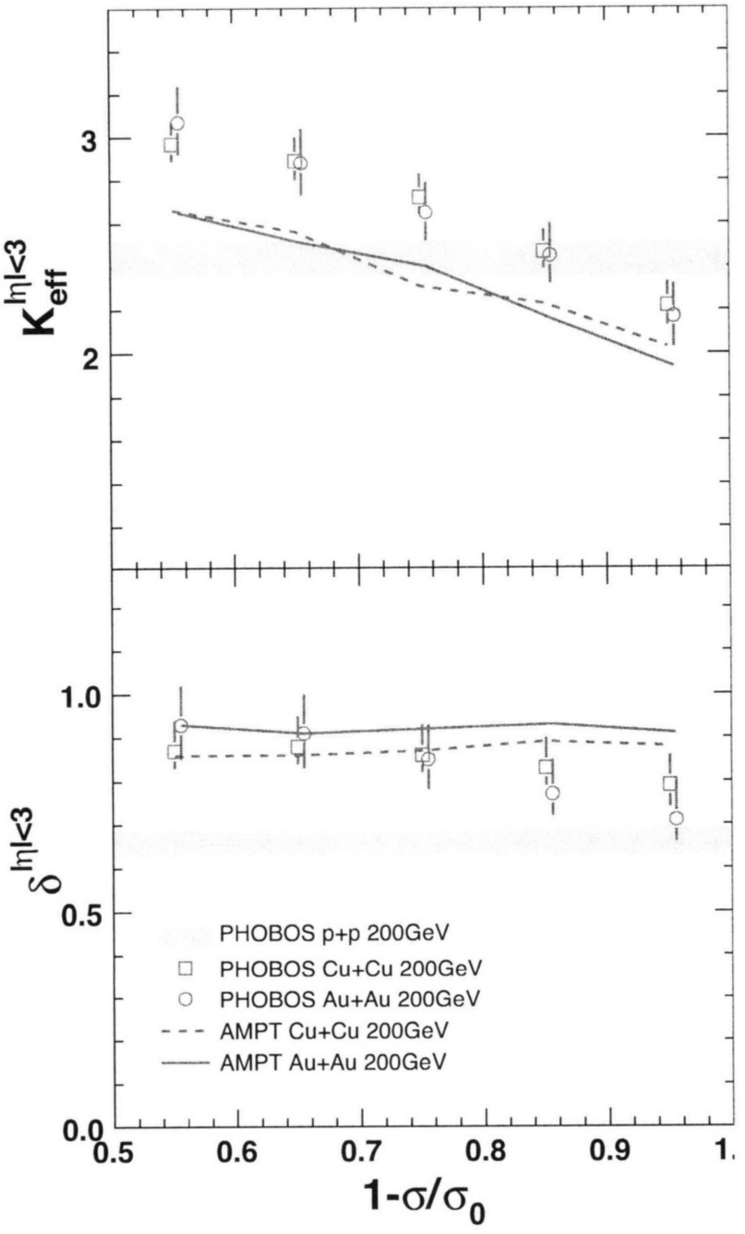

Figure 8.11: K_{eff} (upper panel) and δ (lower panel) as a function of fractional cross section for PHOBOS data (open symbols) and from the AMPT model (lines) in Cu+Cu (squares) and Au+Au (circles) collisions for $|\eta| < 3$ at $\sqrt{s_{\text{NN}}} = 200$ GeV [113]. The error bars for data points represent systematic errors with 90% C.L. Results from p+p collisions at $\sqrt{s} = 200$ GeV [112] are shown by the shaded band.

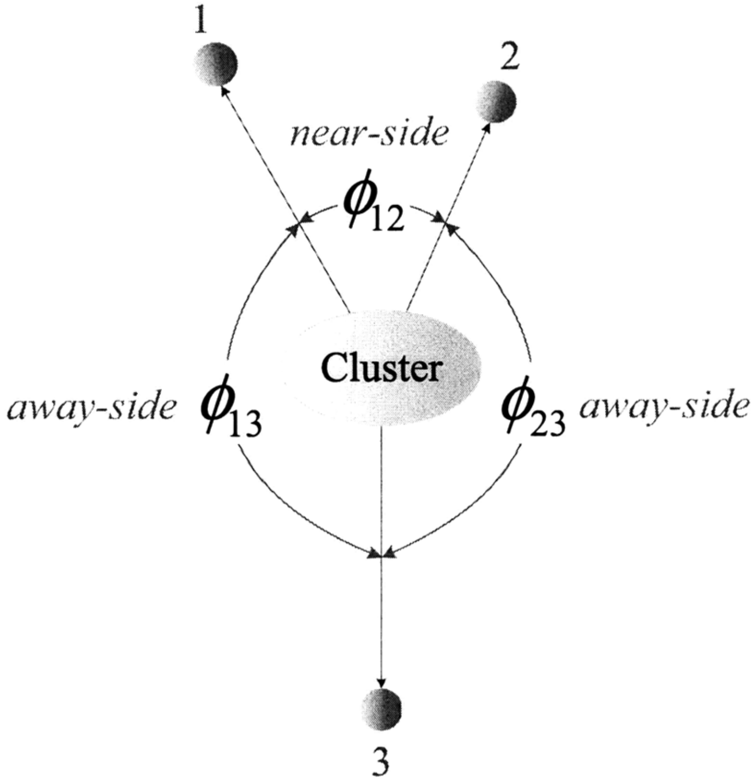

Figure 8.12: An illustration of near-side and away-side clusters. Within the same cluster, correlated pairs having 0° $< \Delta\phi <$ 90° are counted as near-side clusters, while away-side clusters are made up of correlated pairs with 90° $< \Delta\phi <$ 180°.

the system, i.e. the shape of the overlap region. This feature is not obviously expected as the cluster parameters are constructed to reflect short-range correlations in rapidity and thus are not directly connected with the overall geometry of the initial state of the collision. Comparison of the data with AMPT [127] shows that the model gives the same qualitative trend as the data in the same η acceptance, but with K_{eff} values systematically lower by about 0.4. Note that the values of K_{eff} and δ are extracted in a limited acceptance of $|\eta| < 3$, and therefore are normally smaller than for a full acceptance measurement. The acceptance effect will be discussed quantitatively in the next section. In AMPT, the decrease in effective cluster size with increasing event centrality appears to be related to the hadronic rescattering stage. Turning off hadronic rescattering processes in AMPT leads to a larger effective cluster size in both Au+Au and Cu+Cu that is approximately invariant for all centralities (see discussions in Sect. 9.1.1).

Further detailed studies on cluster properties have also been performed. Instead of

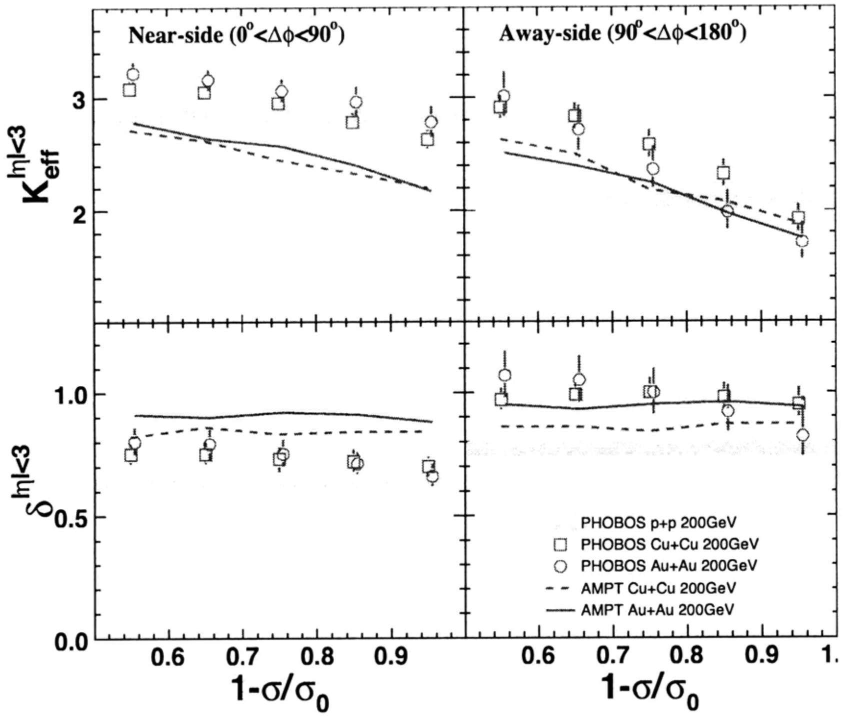

Figure 8.13: Near-side (left column) and away-side (right column) K_{eff} (upper row) and δ (lower row) as a function of fractional cross section for PHOBOS data (open symbols) and from the AMPT model (lines) in Cu+Cu (squares) and Au+Au (circles) collisions for $|\eta| < 3$ at $\sqrt{s_{\mathrm{NN}}} = 200$ GeV [113]. The error bars for data points represent systematic errors with 90% C.L. Results from p+p collisions at $\sqrt{s} = 200$ GeV are shown by the shaded band.

averaging over the whole $\Delta\phi$ region, the cluster parameters can be extracted in the near-side and away-side $\Delta\phi$ ranges ($0° < \Delta\phi < 90°$ and $90° < \Delta\phi < 180°$ respectively), which in general corresponds to higher and lower p_{T} clusters respectively. However, one should note that the actual meaning of near- and away-side clusters is more referred to as correlations contributed by pairs (often from the same cluster) within different $\Delta\phi$ ranges, as illustrated in Fig. 8.12, instead of real distinct clusters. In this restricted averaging, the $\cos(2\Delta\phi)$ elliptic flow component again averages to zero. The results are shown in Fig. 8.13 as a function of fractional cross section for Cu+Cu and Au+Au collisions at $\sqrt{s_{\mathrm{NN}}} = 200$ GeV. Over the studied centrality range, the away-side effective cluster size decreases by about 30-40% with increasing centrality, whereas the decrease for the near-side is somewhat smaller. Such a behavior could be understood in a scenario where the medium is extremely dense at more central collisions and only clusters produced close to the surface can survive. Then, for away-side clusters, it is more likely that part of its decay particles travel into the medium and get absorbed, resulting in a suppression of away-side correlations. As for the observed collision geometry scaling of the effective cluster size, it might be related to the surface to volume ratio of the system. More detailed modeling is still being investigated to understand these phenomena (see Ch. 9). In this case, AMPT shows a smaller difference between near and away-side cluster properties than that in the data.

8.4 Extrapolate to the full phase space

As mentioned in the previous section, some particles from cluster decay fall outside of the PHOBOS detector acceptance in pseudorapidity ($|\eta| < 3$). This both reduces the correlation strength ($K_{\rm eff}$) and narrows the correlation width (δ). In order to quantitatively study this effect, an ICM (implemented in Sect. 8.2.2) as well as several dynamical models are used. In the ICM approach, Fig. 8.14 shows a comparison between 1-D $\Delta\eta$ correlation functions measured in the limited acceptance of $|\eta| < 3$ and the full acceptance. From this comparison, one can see that the shape is significantly modified by the limited acceptance, resulting in reductions in both $K_{\rm eff}$ and δ. By comparing the cluster parameters extracted for the acceptance of $|\eta| < 3$, $K_{\rm eff}^{|\eta|<3}$ and $\delta^{|\eta|<3}$, with the full acceptance, $K_{\rm eff}^{|\eta|<\infty}$ and $\delta^{|\eta|<\infty}$ an acceptance correction can be obtained in the context of the ICM.

Note that in the ICM, δ is not an independent variable, but rather depends on the cluster $p_{\rm T}$ for given cluster mass. The higher $p_{\rm T}$ is, the narrower the cluster width will be. In a scenario of isotropic decay of the clusters, the maximum possible width turns out to be $\delta^{|\eta|<3} \sim 0.75$ for $K = 2$ and $p_{\rm T}$ of all clusters fixed at 0, which is lower than the cluster width observed in A+A collisions ($\sim$ 0.9 in the most peripheral collisions). Therefore, to generate wider range of possible δ parameters in the ICM, another parameter, γ, is introduced to manually modify the width of the clusters by rescaling the relative pseudorapidity of each decay product:

$$\eta'_i - \eta_0 = \gamma \times (\eta_i - \eta_0), i = 1, 2, 3... \tag{8.7}$$

where η_0 represents the pseudorapidity of the original clusters, and η_i and η'_i correspond to the pseudorapidity of decaying particles from clusters before and after modification. In this way, any value of the cluster width can be obtained while keeping original η of the cluster unchanged. For each set of K and γ, the $dN/d\eta$ and $dN/dp_{\rm T}$ distribu-

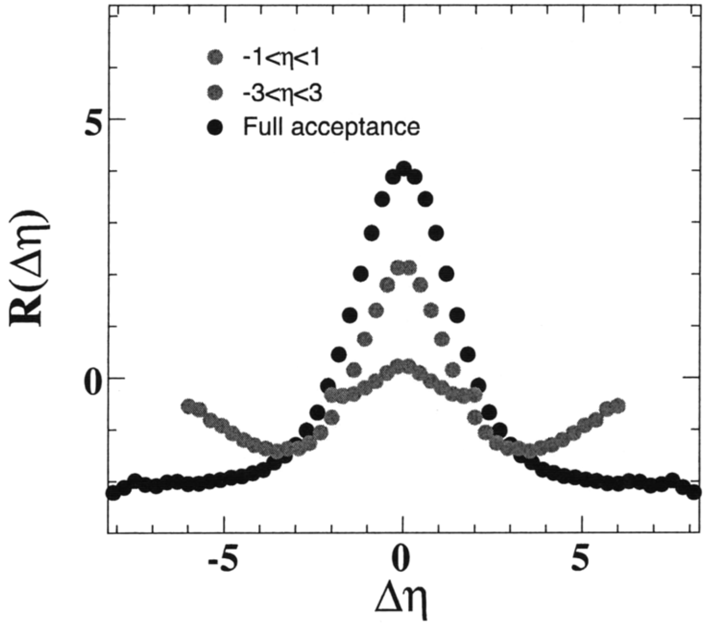

Figure 8.14: Comparison of 1-D $\Delta\eta$ correlation function from ICM with $K = 3$ and $\gamma = 0$ for $|\eta| < 1$, $|\eta| < 3$ and the full acceptance.

tions of the clusters are tuned to match those of final state inclusive charged particles measured in the data.

The ICM, with a range of values of K and γ, has been used to generate a set of two-particle correlation functions, both for $|\eta| < 3$ and full acceptance. In Fig. 8.15, the ratios $(K_{\rm eff}^{|\eta|<3}\text{-}1)/(K_{\rm eff}^{|\eta|<\infty}\text{-}1)$ and $\delta^{|\eta|<3}/\delta^{|\eta|<\infty}$ from the ICM are shown as a function of $\delta^{|\eta|<3}$, as extracted directly from fits to the correlation function. It is clearly seen that the suppression of these ratios are primarily a function of $\delta^{|\eta|<3}$ only, and both $K_{\rm eff}$ and δ are suppressed more as $\delta^{|\eta|<3}$ increases. This is because correlated particles are more likely to fall outside the measured region as the cluster width increases. The suppression factors in the dynamical models like PYTHIA p+p, HIJING, AMPT Cu+Cu and Au+Au at various centralities are also calculated. All models are consistent within about 5%-10%. A second order polynomial function is fitted to the values of all models in order to generate a smooth correction function. This function is applied to the measured $K_{\rm eff}^{|\eta|<3}$ and $\delta^{|\eta|<3}$ using Eq. 8.8 in order to estimate $K_{\rm eff}^{|\eta|<\infty}$ and $\delta^{|\eta|<\infty}$ for the experimental data:

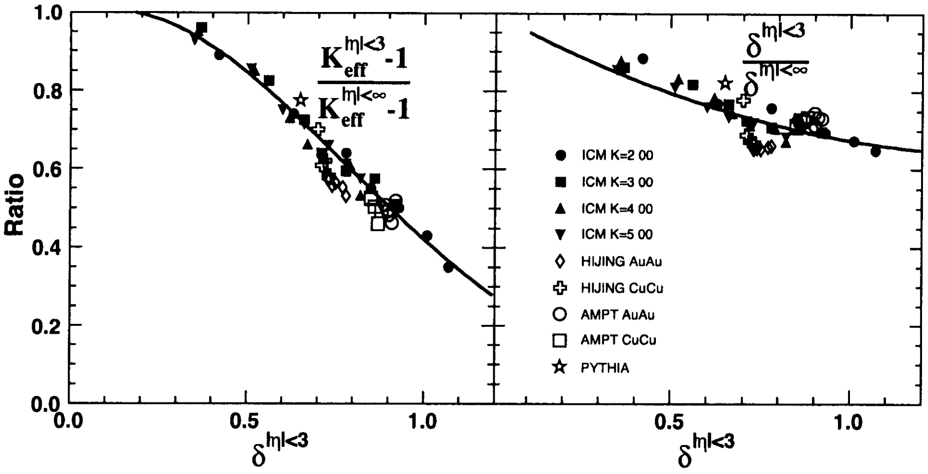

Figure 8.15: Ratio of $K_{\rm eff}^{|\eta|<3}$-1 to $K_{\rm eff}^{|\eta|<\infty}$-1 (left panel) and $\delta^{|\eta|<3}$ to $\delta^{|\eta|<\infty}$ (right panel) as a function of $\delta^{|\eta|<3}$ obtained in ICM (solid symbols) as well as PYTHIA, HIJING and AMPT models (open symbols). The solid line is a smooth function fit to all the models [113].

$$
\begin{aligned}
(K_{\rm eff}^{|\eta|<\infty}-1)_{\rm data} &= \frac{(K_{\rm eff}^{|\eta|<\infty}-1)_{\rm MC}}{(K_{\rm eff}^{|\eta|<3}-1)_{\rm MC}} \times (K_{\rm eff}^{|\eta|<3}-1)_{\rm data} \\
&= (K_{\rm eff}^{|\eta|<3}-1)_{\rm data}/\epsilon_{K_{\rm eff}} \\
\delta_{\rm data}^{|\eta|<\infty} &= \frac{\delta_{\rm MC}^{|\eta|<\infty}}{\delta_{\rm MC}^{|\eta|<3}} \times \delta_{\rm data}^{|\eta|<3} \\
&= \delta_{\rm data}^{|\eta|<3}/\epsilon_{\delta}
\end{aligned}
\tag{8.8}
$$

The scattering of the points around the fitted correction curved in Fig. 8.15 is taken into account as one source of the systematic uncertainties on the acceptance correction procedure. As a cross check, the cluster parameters in the data have also been measured in $|\eta| < 2$. The ratios, $(K_{\rm eff}^{|\eta|<2}-1)/(K_{\rm eff}^{|\eta|<3}-1)$ and $\delta^{|\eta|<2}/\delta^{|\eta|<3}$, are found to be consistent with the ICM and dynamical models. The residual discrepancies between the results extrapolated to full phase space from $|\eta| < 2$ and $|\eta| < 3$ are used to estimate a separate contribution to the systematic uncertainty on the acceptance correction. The total uncertainty on the correction is thus found to be 12% for $K_{\rm eff}$ and 9% for δ.

After applying the acceptance correction, the cluster parameters at full phase space, $K_{\rm eff}^{|\eta|<\infty}$ and $\delta^{|\eta|<\infty}$, in p+p, Cu+Cu and Au+Au collisions at $\sqrt{s_{\rm NN}} = 200$ GeV are shown

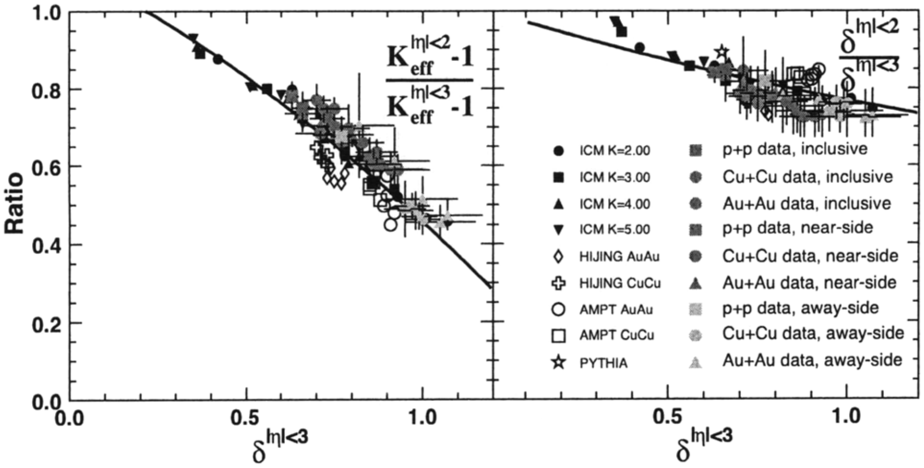

Figure 8.16: Ratio of $K_{\text{eff}}^{|\eta|<2}$-1 to $K_{\text{eff}}^{|\eta|<3}$-1 (left panel) and $\delta^{|\eta|<2}$ to $\delta^{|\eta|<3}$ (right panel) as a function of $\delta^{|\eta|<3}$ obtained in the data as well as ICM, PYTHIA, HIJING and AMPT models.

in Fig. 8.17 for inclusive (left), near-side (middle) and away-side (right) as well as the results from AMPT. The correction factors applied, $\epsilon_{K_{\text{eff}}}$ and ϵ_{δ}, are summarized in Table 8.4. The systematic errors come from not only the measurement itself but also the acceptance correction procedure (addition in quadrature). The values of K_{eff} and δ in p+p collisions extrapolated to full phase space are larger than those presented in Sect. 8.3.2 [112] measured in a limited acceptance of $|\eta| < 3$, and better reflect the properties of the clusters produced in these reactions. Since δ measured in both Cu+Cu and Au+Au collisions at PHOBOS only weakly depends on centrality, the geometric scaling feature of K_{eff} between the two systems still holds after the acceptance correction as shown in Fig. 8.17. That said, the large values of $K_{\text{eff}}^{|\eta|<\infty}$ and $\delta^{|\eta|<\infty}$ clearly pose a challenging question as to the origin of such strong correlations with such a long range. In calculations from the Therminator model that include all known resonances [128], K_{eff} is approximately 2 and δ is no larger than 0.75, while in peripheral A+A collisions, there appear to be clusters that decay into 5-6 charged particles (up to about 9 if including neutral particles) with much larger δ. This was not something expected from previous data in p+p collisions, although there are data on $\langle p_{\text{T}} \rangle$ fluctuations from STAR [129, 130] and PHENIX [131, 132] that have been interpreted as evidence for similarly large clusters in Au+Au collisions [133]. The production of jets is a natural mechanism to induce clustering phenomena, although one would expect jets to lead to a smaller δ than isotropic decay. It is also possible that additional correlation sources, such as dynami-

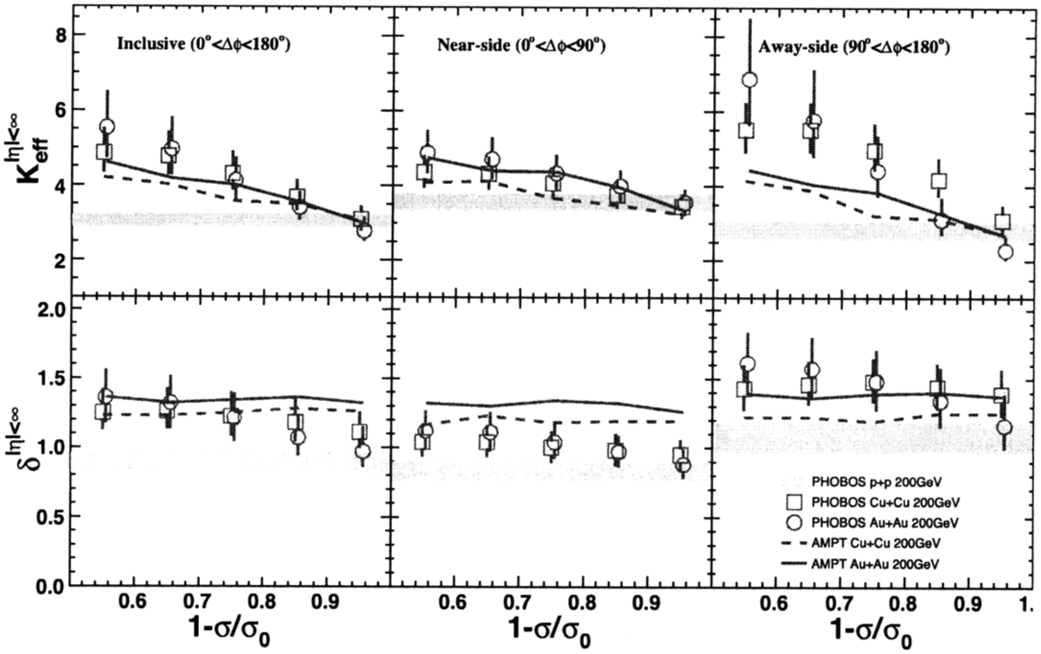

Figure 8.17: Inclusive (left column), near-side (middle column) and away-side (right column) K_{eff} (upper row) and δ (lower row) as a function of fractional cross section measured by PHOBOS (open symbols) and from the AMPT model (lines) after corrected to the full acceptance in Cu+Cu (squares) and Au+Au (circles) collisions at $\sqrt{s_{\text{NN}}} = 200$ GeV [113]. The error bars for data points represent systematic errors with 90% C.L. Results in p+p collisions at $\sqrt{s} = 200$ GeV after corrected to the full acceptance are shown in the shaded band, which are larger than those in Sect. 8.3.2, measured in an acceptance of $|\eta| < 3$.

cal fluctuation of the $dN/d\eta$ distribution event-by-event, may modify the two-particle correlations in a way that leads to an increase of the observed effective cluster size. The fact that $\delta^{|\eta|<\infty}$ in peripheral A+A collisions is larger than p+p, and far exceeds the value expected for isotropic decay, also begs the question as to how the cluster decays are "elongated" in phase space. Finally, it is observed that cluster parameters in central events approach values measured in p+p collisions, while those in peripheral events are substantially higher — almost a factor of two in terms of K_{eff}-1 (which is equivalent to the so-called "conditional yield" in analyses involving high p_{T} triggered hadrons). Overall, more theoretical insights are needed to understand these surprising features of two-particle correlations in heavy ion collisions. See next chapter for more modeling studies and developments.

p+p, 200 GeV							**p+p, 410 GeV**						
	Inclusive		**Near-Side**		**Away-Side**			**Inclusive**		**Near-Side**		**Away-Side**	
Centrality	$\epsilon_{K_{\text{eff}}}$	ϵ_{δ}	$\epsilon_{K_{\text{eff}}}$	ϵ_{δ}	$\epsilon_{K_{\text{eff}}}$	ϵ_{δ}	Centrality	$\epsilon_{K_{\text{eff}}}$	ϵ_{δ}	$\epsilon_{K_{\text{eff}}}$	ϵ_{δ}	$\epsilon_{K_{\text{eff}}}$	ϵ_{δ}
N/A	0.70	0.75	0.73	0.76	0.60	0.72	N/A	0.69	0.74	0.75	0.76	0.59	0.72

Cu+Cu, 200 GeV							**Au+Au, 200 GeV**						
	Inclusive		**Near-Side**		**Away-Side**			**Inclusive**		**Near-Side**		**Away-Side**	
Centrality	$\epsilon_{K_{\text{eff}}}$	ϵ_{δ}	$\epsilon_{K_{\text{eff}}}$	ϵ_{δ}	$\epsilon_{K_{\text{eff}}}$	ϵ_{δ}	Centrality	$\epsilon_{K_{\text{eff}}}$	ϵ_{δ}	$\epsilon_{K_{\text{eff}}}$	ϵ_{δ}	$\epsilon_{K_{\text{eff}}}$	ϵ_{δ}
40%-50%	0.51	0.70	0.62	0.72	0.42	0.68	40%-50%	0.46	0.69	0.57	0.71	0.34	0.66
30%-40%	0.50	0.70	0.62	0.72	0.41	0.68	30%-40%	0.47	0.69	0.58	0.71	0.36	0.67
20%-30%	0.52	0.70	0.64	0.73	0.40	0.67	20%-30%	0.53	0.70	0.62	0.72	0.40	0.67
10%-20%	0.55	0.71	0.64	0.73	0.42	0.68	10%-20%	0.60	0.72	0.66	0.73	0.47	0.69
0%-10%	0.58	0.71	0.66	0.74	0.44	0.68	0%-10%	0.58	0.71	0.70	0.74	0.56	0.71

Table 8.1: A summary of acceptance correction factors applied that extrapolate the cluster parameters measured for $|\eta| < 3$ to the full η coverage.

9 Model Studies

To gain more insights on the physical implication of observed correlations presented in previous chapters, in particular the origin of centrality dependence of cluster parameters and the large cluster size with such a long range, studies on modeling are performed in this chapter. Models that are investigated include the AMPT model and a cluster absorption model built based on ICM developed in Sect. 8.2. These studies should shed more lights on the property of hot and dense matter created in the heavy ion collisions.

9.1 Centrality dependence of Cluster Parameters

Dependence on collision centrality of cluster parameters in A+A collisions, as well as the geometric scaling between different colliding ion species, is a main feature of two-particle correlations measured in this thesis. In this section, The AMPT model and a modified ICM with the mechanism of absorbing particles inside the medium are used to understand these features.

9.1.1 AMPT Model

The A Multiphase Transport Model (AMPT) model [127] is a model that explicitly deals with nonequilibrium dynamics during the evolution of a relativistic heavy ion collision system. It includes the descriptions of both initial partonic and final-state hadronic interactions as well as the transition from partonic to hadronic degree of freedom of the matter.

The schematic structure of default AMPT model can be found in Fig. 9.1 [127]. The initial conditions are obtained from HIJING model, which includes the spacial and momentum distribution of minijet partons and soft string excitations. It is followed by a partonic cascade model (ZPC) where two-body scatterings between partons are included. After interactions stop, partons and strings turn into hadrons according to the Lund string fragmentation model [31, 35, 134]. At the final step, since the hadronic mat-

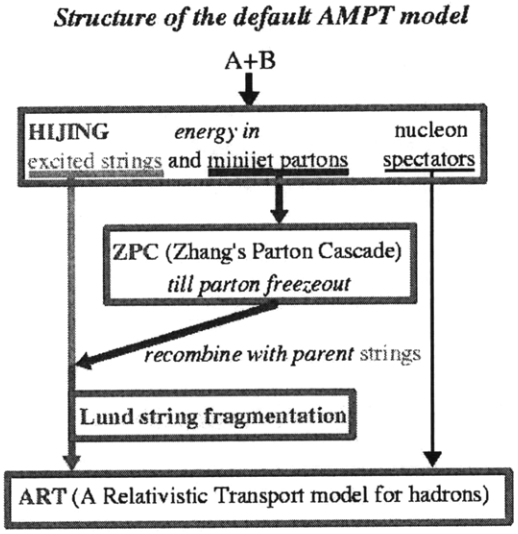

Figure 9.1: Schematic structure of the default AMPT model [127].

ter is still hot and dense, it evolves via a hadronic cascade phase until a cutoff time t_{cut} when all observables are stable and final.

As shown in Sect. 8.3.3, the observed centrality dependence of K_{eff} and δ in the data is qualitatively consistent with that in the AMPT model, although a little off in terms of the absolute scale. More surprisingly, it also gives the same geometric scaling of cluster parameters between Cu+Cu and Au+Au collisions as in the data. By switching on and off various processes in AMPT, one can potentially track back the origin of these observables in the model. Note that in HIJING model, no obvious centrality dependence of cluster parameters is present, so the effect should be a consequence of the partonic or hadronic cascade process in AMPT.

The duration of hadronic interactions in AMPT is controlled via a cutoff time t_{cut} which is determined by:

$$t_{cut} = \text{NTMAX} \times \text{DT} \tag{9.1}$$

where DT represents the time-step (in fm/c) for each hadronic interaction in the lab frame, default to be 0.2, and NTMAX defines the number of time-steps with a default value of 150. Therefore, by setting NTMAX to a very small value, all hadronic cascade effects will be effectively turned off. For partonic cascade, its cross section is inversely proportional to the parton screening mass ($m_{screen} = 3.2264$ in fm^{-1} by default). A large m_{screen} will essentially remove all partonic rescatterings.

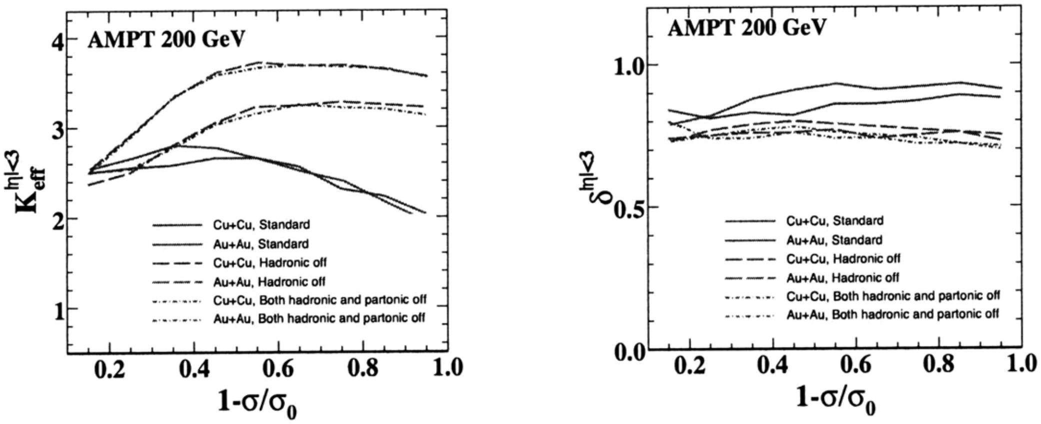

(a)

(b)

Figure 9.2: (a) K_{eff} and (b) δ for $|\eta| < 3$ as a function of fractional cross section in 200 GeV Cu+Cu and Au+Au AMPT events with default version, hadronic effects off, and both hadronic and partonic effects off.

In studies of this thesis, AMPT events with different sets of parameters are generated for Cu+Cu and Au+Au collisions at $\sqrt{s_{\mathrm{NN}}} = 200$ GeV:

- All hadronic effects off (NTMAX=3)
- Both hadronic and partonic effects off (NTMAX=3, $m_{screen} = 10000$)
- Less hadronic effects (NTMAX=45)
- More hadronic effects (NTMAX=600)

Two-particle correlation functions are then calculated for each set of events as a function of collision centrality. The extracted K_{eff} and δ at $|\eta| < 3$ are presented in Fig. 9.2 and Fig. 9.3 along with the standard AMPT results, as a function of fractional cross section (down to very peripheral collisions). As shown in Fig. 9.2, after switching off the hadronic processes, K_{eff} increase significantly for both Cu+Cu and Au+Au collisions, while δ become smaller, getting closer to the limit of isotropic decay of clusters. If clusters decay at the hadronization stage, their decay products would undergo further rescatterings with the presence of other hadrons, resulting in the loss of original correlations, and hence smaller cluster size. Since hadronic rescattering effect is expected to be related to the system size (as larger the system is, longer it will last), the geometric scaling feature of cluster parameters in AMPT does not hold anymore with this effect off (larger values in Au+Au). Imagine that there exists some physical mechanism which

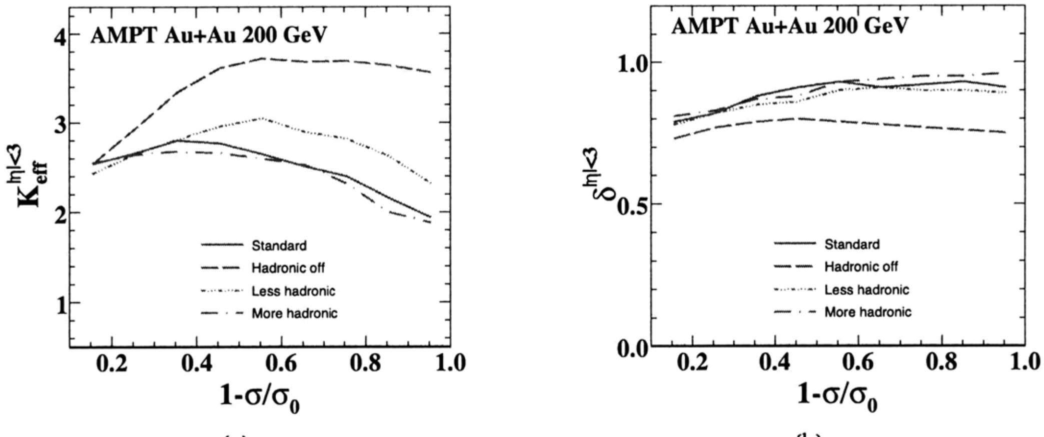

(a)

(b)

Figure 9.3: (a) K_{eff} and (b) δ for $|\eta| < 3$ as a function of fractional cross section in 200 GeV Au+Au AMPT events with default version, all hadronic effects off, part of hadronic effects off and more hadronic effects.

has the function of enhancing the cluster size with system size dependence like observed in the region of very peripheral AMPT events, it could cancel out the hadronic rescattering effect which diminishes the cluster size with exactly an opposite system size dependence. This might be a possible explanation of the geometric scaling phenomena observed in both data and AMPT model. Partonic cascade process is found to have very little impact on either K_{eff} or δ.

Moreover, by varying the duration (NTMAX) of the rescattering process, K_{eff} and δ are also found to be strongly correlated with the intensity of this effect (see Fig. 9.3). Extending the duration of default hadronic processes does not seem to have a significant impact on the cluster parameters. This is likely because the system is already very dilute beyond that point, and hadronic effect hence becomes less important.

9.1.2 Cluster Absorption Model

To have better control on destructing the correlations, a cluster absorption model is invented based on ICM developed in Sect. 8.2.2.

Clusters are generated with a spacial coördinates uniformly inside a overlap region of two colliding nuclei at a given impact parameter b (e.g. $b = 0$ in Fig. 9.4(a)). Later on, each cluster decays into final-state hadrons, some of which would travel through part of the medium formed. To simulate the influence of hadronic rescatterings on two-

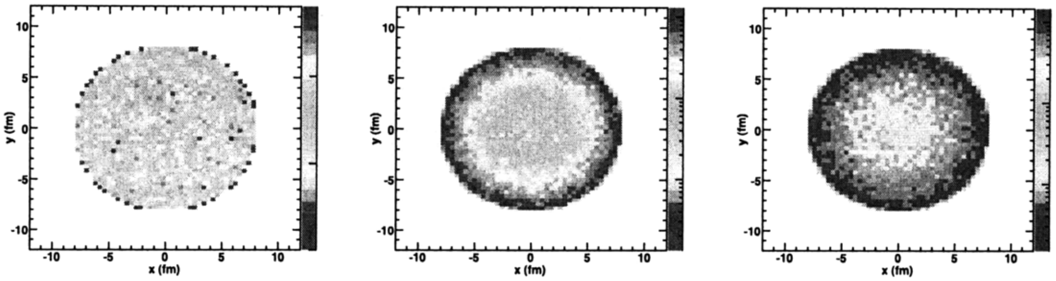

(a) Clusters, $b=0$

(b) Particles, $b = 0$ and $\lambda_{abs} =$ 2 fm

(c) Particles, $b = 0$ and $\lambda_{abs} =$ 4 fm

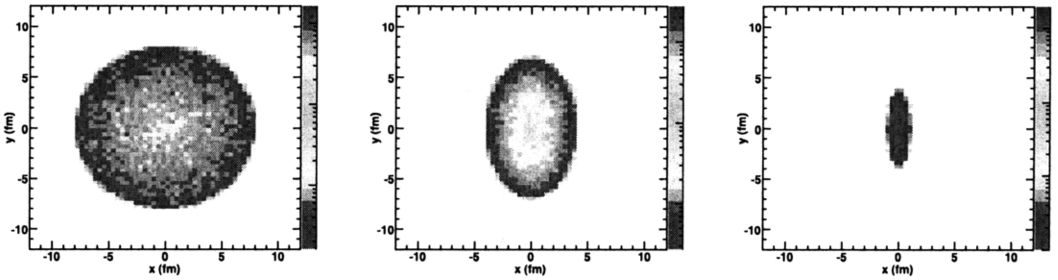

(d) Particles, $b = 0$ and $\lambda_{abs} =$ 6 fm

(e) Particles, $b = 8$ and $\lambda_{abs} =$ 2 fm

(f) Particles, $b = 14$ and $\lambda_{abs} =$ 2 fm

Figure 9.4: Spacial distribution in $x-y$ plane of (a) clusters and (b)-(f) final-state particles in the cluster absorption model with different parameters b and λ_{abs}. The radius of the nucleus is fixed at 8 fm.

particle correlations, it is assumed in this model that a decay particle from a cluster would only survive the medium with a probability:

$$P_{survive} = \exp(-l/\lambda_{abs}), \tag{9.2}$$

where l is the path length of particle moving inside the matter (overlap region) and parameter λ_{abs} denotes the characteristic absorption length. Systems with various absorption length λ_{abs} and impact parameters b are simulated. The radius of the nucleus is chosen to be 8 fm. Corresponding spacial distribution of final-state particles from clusters are displayed in Fig. 9.4(b) -Fig. 9.4(f) in the $x-y$ plane. Additionally, the velocity vector of each cluster is always required to point outward the medium from the origin. This condition somewhat takes into account the radial flow effect of an expanding system. Note that this cluster absorption model oversimplifies many facts of a colliding nucleus-nucleus system. For example, the Woods-Saxon potential of the nucleus density distribution function (see Eq. C.1) should be used, instead of a uniform distribution. Also, calculations of the path length and survival probability is only considered in two dimensional space ($x - y$ plane) without a full 3-D implementation. So the main purpose of this simple model is an attempt to provide a qualitative description.

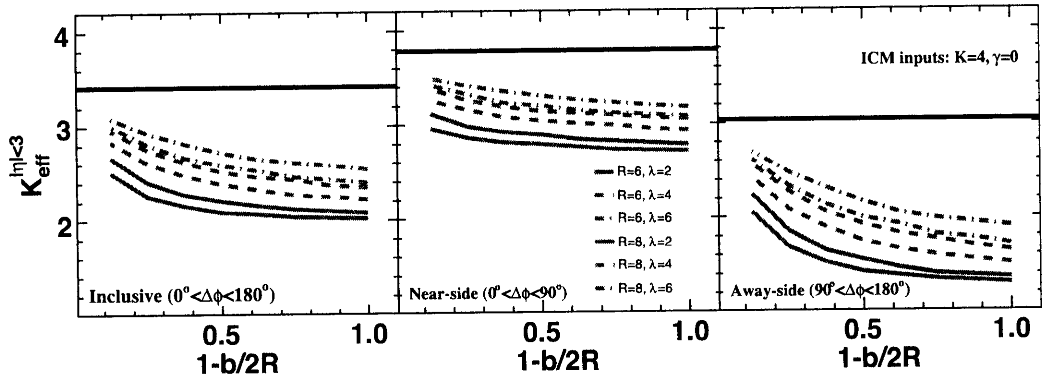

Figure 9.5: Inclusive (left column), near-side (middle column) and away-side (right column) K_{eff} for $|\eta| < 3$ as a function of $1 - b/2R$ in the cluster absorption model with various b and λ_{abs} values, as well as different radius R of the nucleus.

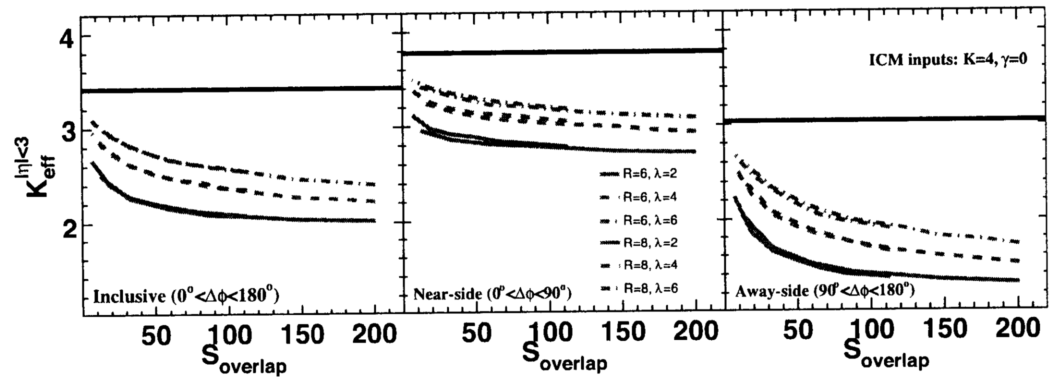

Figure 9.6: Inclusive (left column), near-side (middle column) and away-side (right column) K_{eff} for $|\eta| < 3$ as a function of the overlap area of two nuclei, $S_{overlap}$, in the cluster absorption model with various b and λ_{abs} values, as well as different radius R of the nucleus.

For different b and λ_{abs} parameters, two-particle correlation functions are built in the cluster absorption model, in order to study the system size dependence of the absorption effect. Different radius (R=6 fm and 8 fm) of the nucleus are also compared to check if the observed geometric scaling could naturally originate from the surface to volume ratio of the system. The effective cluster size K_{eff} and decay width δ are extracted for inclusive, near-side and away-side clusters, as a function of $1-b/2R$ (geometric shape) in Fig. 9.5 and $S_{overlap}$ (area of overlap region, πab) in Fig. 9.6 for different R and λ_{abs}. As one can see, the effective cluster size decreases with increasing collision centrality for all three cases of inclusive, near-side and away-side clusters. However, the size at away-side drops much more rapidly than that at near-side. This is qualitatively consistent with what is observed in the data. Meanwhile, comparing the results at different radius R of the nucleus (like between Cu+Cu and Au+Au), this naive absorption effect is found to scale with the overall system size, instead of the shape of the overlap region.

9.2 Implication of Large and Wide-range Clusters

To investigate the source of large observed cluster size and width, AMPT is again used but from a different aspect. All partonic and hadronic cascade processes are switched off in this study. Moreover, the possible effect from dynamical fluctuation of $dN/d\eta$ distribution is also discussed.

9.2.1 AMPT Model

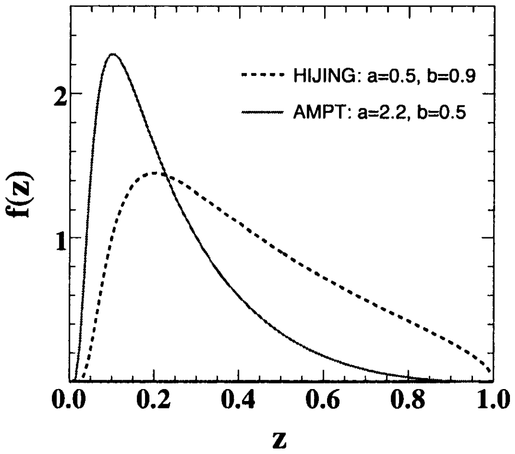

Figure 9.7: Lund string fragmentation function with different parameters a and b (see Eq. 9.3) for default HIJING and AMPT models.

In Lund string fragmentation scenario, minijets are combined with their parent strings to form excited strings at the end of partonic interaction stage. Strings then fragment into quark-antiquark pairs to be converted into hadrons. In particular, the transverse momentum of a hadron is determined by that of its constituent quarks from a Gaussian distribution. Its longitudinal momentum is given by the Lund symmetric fragmentation function:

$$f(z) \propto z^{-1}(1-z)^a \exp(-b m_\perp^2/z), \tag{9.3}$$

where z corresponds to the light-cone momentum fraction of the produced hadron with respect to the fragmenting string. In default HIJING model, parameters a and b are set to be 0.5 and 0.9 GeV^{-2} in order to reproduce the charged multiplicity in p+p and p+$\bar{\text{p}}$ collisions, while the experimental data in heavy ion collisions are found to be reasonably described with $a = 2.2$ and $b = 0.5$ GeV^{-2}. The fragmentation functions with these two different settings in HIJING and AMPT are displayed in Fig. 9.7 at fixed $m_\perp = 0.5$ GeV/c^2.

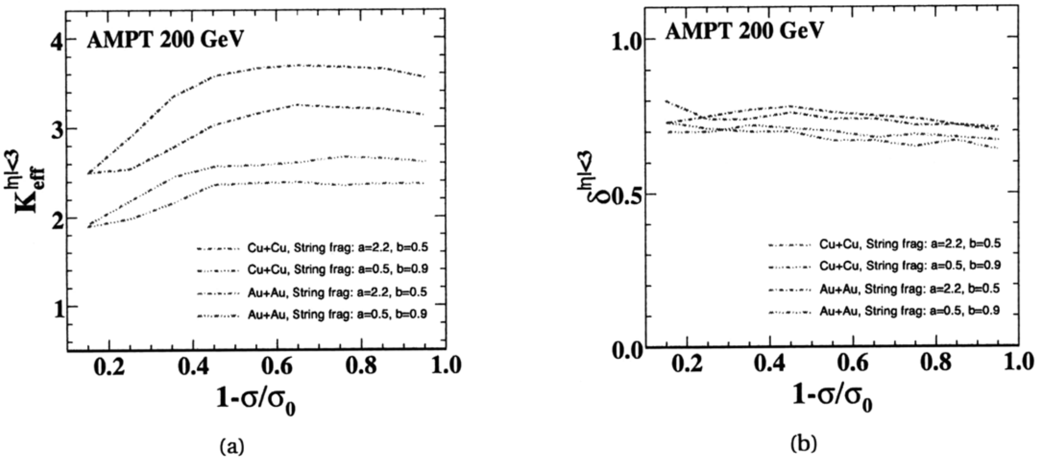

(a)

(b)

Figure 9.8: (a) K_{eff} and (b) δ for $|\eta| < 3$ as a function of fractional cross section in 200 GeV Cu+Cu and Au+Au AMPT events with different parameters of Lund string fragmentation function. All partonic and hadronic effects are switched off.

Cluster parameters are compared between two different fragmentation functions in AMPT (see Fig. 9.8). For both Cu+Cu and Au+Au collisions, larger values of K_{eff} and δ are found with $a = 2.2$ and $b = 0.5$ GeV^2 in standard AMPT model. Especially for K_{eff}, there is almost a 50% difference. According to the fragmentation function defined in Eq. 9.3 and illustrated in Fig. 9.7, with a larger value of a parameter, the distribution becomes softer, shifted to smaller z region. Hadrons fragmented from a string will thus carry a smaller fraction of its momentum. As a consequence, more hadrons from a string are created, which increases the cluster size. This study shows that the existence of string and its fragmentation is a possible contribution to the observed strong cluster-like correlations, although not a direct evidence.

9.2.2 Dynamical Fluctuations of $dN/d\eta$ Distribution

While the average shape of $dN/d\eta$ does not affect the two-particle correlation measurement, the dynamical fluctuations of $dN/d\eta$ distribution event-by-event could modify the two-particle correlations, and thus contribute to cluster parameters. This possibility is investigated below.

Recall that $dN/d\eta$ distribution of clusters is determined by their p_{T} and $p_{\parallel}$ distributions (see Eq. 8.1). In this study, b_1 and b_2 parameters in $p_{\parallel}$ distribution of Eq. 8.1 are randomly varied according to a Gaussian distribution with certain width of σ_{b_1} and σ_{b_2}. The ICM with $K = 3$ is used with $b_1 = 1.5$ and $b_2 = 4.3$. σ_{b_1} and σ_{b_2} are chosen to be 0.8 and 1.5 respectively, which produces a quite large fluctuation on the resulting cluster $dN/d\eta$ distribution. After decay of clusters, the $dN/d\eta$ distributions of single particles are illustrated in Fig. 9.9(a) for original b_1, b_2 values as well as ones with one Gaussian σ deviating from them.

Implementing the fluctuating $dN/d\eta$ in ICM, the two-particle pseudorapidity correlation functions are studied for different event multiplicities, and compared with the standard ICM (see Fig. 9.9(b)). With a small event multiplicity (N=60), this effect is found to be negligible. However, as multiplicity grows up, the correlation function is significantly modified. The multiplicity scaling of this effect is somewhat similar to the v_2 modulation of the correlation function in $\Delta\phi$ discussed in Sect. 8.1.2, which is also a global correlation among all the particles. With fine tuning of the amount of fluctuation for each centrality (or multiplicity), it is possible to reproduce the values of cluster parameters found in data. The current experimental technique in this thesis is not able to directly exclude the possibility of this scenario. However, considering the observed structure of correlation function in 2-D, the picture of cluster-like emission is still more preferable.

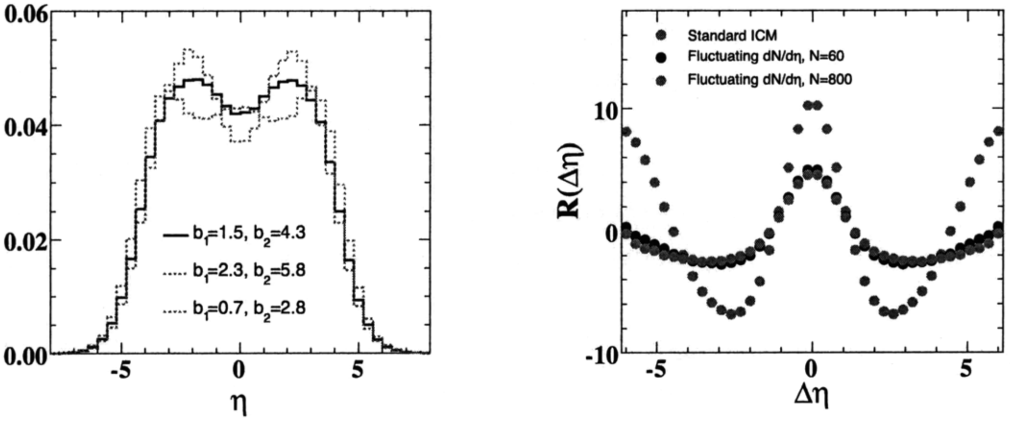

(a)

(b)

Figure 9.9: (a) $dN/d\eta$ distributions of final-state particles in ICM with different parameters of cluster $p_{\parallel}$ distribution. (b) Two-particle $\Delta\eta$ correlation functions in ICM with fixed and varying (also two different multiplicities) $dN/d\eta$ distributions.

10 Summary

The phenomenological properties of hadronization process via massive objects, "clusters", have been systematically studied in this thesis from the measurements of inclusive charged two-particle angular correlations over a wide range in $\Delta\eta$ and $\Delta\phi$, for high energy proton-proton and nucleus-nucleus collisions. The data were collected using the PHOBOS detector at the Relativistic Heavy Ion Collider (RHIC) during 2004 and 2005 runs.

Two-particle angular correlation functions for all charged particles in p+p collisions at $\sqrt{s} = 200$ and 410 GeV have been measured using the PHOBOS Octagon detector, which covers a pseudorapidity range of $-3 < \eta < 3$ and almost full azimuthal space. Complex structures emerged from two-dimensional (2-D) correlation functions in $\Delta\eta$ and $\Delta\phi$. Short-range correlations in $\Delta\eta$ were observed over the full range in $\Delta\phi$, with a maximum at $\Delta\eta = 0$ which becomes wider at larger $\Delta\phi$. Moving onto nucleus-nucleus systems of Cu+Cu and Au+Au collisions at $\sqrt{s_{_{NN}}} = 200$ GeV, the two-particle correlation functions have been constructed for different collision centralities. Short-range feature of correlations in $\Delta\eta$ space has also been observed. Besides, a $\cos(2\Delta\phi)$ modulation was also present due to the elliptic flow effects in non-central A+A collisions.

A cluster model of hadronization phenomena has been used to describe the observed two-particle correlations. The cluster model is a generic description of the transition phase from partonic to hadronic degree of freedom of the system. It assumes that the intermediate-state clusters are first formed independently, then decay isotropically into final-state observed hadrons according to the available phase space. A Monte Carlo approach of an Independent Cluster Model (ICM) was developed in this thesis, which simulated the decay of clusters into certain number of particles. The 2-D structure of two-particle correlation function derived from ICM were found to be qualitatively in good agreement with what's observed in the data.

In the context of the cluster model, the effective cluster size (K_{eff}) and decay width (δ) in η have been extracted from the two-particle pseudorapidity correlation function. A typical effective cluster size of 2.5-3.5 charged particles was found in p+p collisions. Dependence of the effective cluster size on both beam energy and scaled multiplicity was observed, while the cluster width was essentially constant. The short-range correlation strength (or equivalently the effective cluster size, K_{eff}) exceeded the expectation from the decays of resonance particles, suggesting the need for other sources of short-range correlations. The results were compared with previous experiments at ISR and SPS, as well as HIJING and PYTHIA event generators. In PYTHIA and HIJING, the effective cluster size was underestimated.

Measurements of cluster properties in A+A showed a non-trivial decrease in cluster size with increasing centrality, and a surprising geometric scaling between Cu+Cu and Au+Au collisions which was qualitatively described by the AMPT model. Analysis of near- and away-side clusters provided additional information on the details of the cluster properties. Extrapolating the measured cluster parameters to the full phase space using an independent cluster model as well as other dynamic models such as PYTHIA, HIJING and AMPT, the cluster size and width have increased in magnitude to a level which seemed to challenge most conventional understandings of the hadronization process, and also imposed strong constrains on phenomenological models of heavy ion collisions.

Finally, studies on modelings have been performed in order to address two key issues in this analysis: the observed centrality dependence of cluster parameters and the implication of large and wide-range clusters. The hadronic cascade process in AMPT was found to provide a reasonable account for the decrease in effective cluster size with increasing system size. A cluster absorption model was also introduced based on the basic assumptions of ICM. It somehow gave similar effects as hadronic cascade in AMPT and also reproduced the feature observed in the near- and away-side clusters. For the origin of such large clusters, string fragmentation seemed to play an important role in AMPT. In addition, the dynamical fluctuation of $dN/d\eta$ distribution was also a possible source to induce two-particle correlations in pseudorapidity.

Look into the future, the onset of LHC at CERN will bring particle and nuclear physics into a new era of high energy frontier. With p+p collisions at $\sqrt{s} = 14$ TeV, collision energy and event multiplicity dependence of cluster properties will be investigated over a much wider dynamical range in more details. Especially, in the very high multiplicity p+p events where exotic phenomena might manifest itself as gigantic clusters (e.g. a black hole vaporized into a big bunch of final-state hadrons), studies of cluster properties from two-particle correlations will be a powerful tool in unveiling these new physics. Moreover, Pb+Pb collisions at $\sqrt{s_{\text{NN}}}$=5.5 TeV (almost a factor of 30 jump in collision energy compared to RHIC) will provide us the opportunity of exploring further the system size (as well as collision energy) dependence of cluster properties, i.e. the geometric scaling features observed at RHIC. All these future measurements will definitely improve our understandings of the matter created in the relativistic heavy ion collisions.

A PHOBOS Collaboration List

B. Alver[4], B. B. Back[1], M. D. Baker[2], M. Ballintijn[4], D. S. Barton[2], R. R. Betts[6], R. Bindel[7], W. Busza[4], Z. Chai[2], V. Chetluru[6], E. García[6], T. Gburek[3], K. Gulbrandsen[4], J. Hamblen[8], I. Harnarine[6], C. Henderson[4], D. J. Hofman[6], R. S. Hollis[6], R. Hołyński[3], B. Holzman[2], A. Iordanova[6], J. L. Kane[4], P. Kulinich[4], C. M. Kuo[5], W. Li[4], W. T. Lin[5], C. Loizides[4], S. Manly[8], A. C. Mignerey[7], R. Nouicer[2], A. Olszewski[3], R. Pak[2], C. Reed[4], E. Richardson[7], C. Roland[4], G. Roland[4], J. Sagerer[6], I. Sedykh[2], C. E. Smith[6], M. A. Stankiewicz[2], P. Steinberg[2], G. S. F. Stephans[4], A. Sukhanov[2], A. Szostak[2], M. B. Tonjes[7], A. Trzupek[3], G. J. van Nieuwenhuizen[4], S. S. Vaurynovich[4], R. Verdier[4], G. I. Veres[4], P. Walters[8], E. Wenger[4], D. Willhelm[7], F. L. H. Wolfs[8], B. Wosiek[3], K. Woźniak[3], S. Wyngaardt[2], B. Wysłouch[4]

[1] Argonne National Laboratory, Argonne, IL 60439-4843, USA
[2] Brookhaven National Laboratory, Upton, NY 11973-5000, USA
[3] Institute of Nuclear Physics PAN, Kraków, Poland
[4] Massachusetts Institute of Technology, Cambridge, MA 02139-4307, USA
[5] National Central University, Chung-Li, Taiwan
[6] University of Illinois at Chicago, Chicago, IL 60607-7059, USA
[7] University of Maryland, College Park, MD 20742, USA
[8] University of Rochester, Rochester, NY 14627, USA

B Kinematic Variables

In high-energy physics, it is customary to parameterize the longitudinal axis in terms of rapidity variable, y:

$$\begin{aligned} y &= \frac{1}{2}\ln\left(\frac{E+p_z}{E-p_z}\right). \\ &= \frac{1}{2}\ln\left(\frac{1+\beta}{1-\beta}\right). \end{aligned} \tag{B.1}$$

The most useful feature of the rapidity variable is that it is additive under Lorentz transformation. In this sense, rapidity in relativistic mechanics is analogous to velocity in non-relativistic mechanics, where velocity is additive under Galilean transformations. In the limit of small β, rapidity is essentially a measure of velocity. Expanding y in Eq. B.1 with respect to β gives:

$$y = \beta + O(\beta^3). \tag{B.2}$$

In many experimental situations, the identity of a particle is unknown. It is convenient to approximate rapidity with pseudorapidity which can be determined based only on the polar angle θ. This is is a good approximation in the high-energy limit where the particle mass is small compared to its momentum.

$$\begin{aligned} y &= \frac{1}{2}\ln\left(\frac{E+p_z}{E-p_z}\right) \\ &\approx \frac{1}{2}\ln\left(\frac{p+p_z}{p-p_z}\right) \qquad \text{for } m^2 \ll E^2 \\ &= \frac{1}{2}\ln\left(\frac{p+p\cos(\theta)}{p-p\cos(\theta)}\right) \\ &= \frac{1}{2}\ln\left(\frac{1+\cos(\theta)}{\sin(\theta)}\,\frac{\sin(\theta)}{1-\cos(\theta)}\right) \\ &= \frac{1}{2}\ln\left(\frac{1}{\tan(\theta/2)}\,\frac{1}{\tan(\theta/2)}\right) \end{aligned} \tag{B.3}$$

$$y \approx -\ln(\tan(\theta/2)) \equiv \eta \tag{B.4}$$

For a particle of rest mass m_0 and transverse momentum transverse p_T , a transverse mass of the particle can be define: $m_T = \sqrt{m_0^2 + p_\mathrm{T}^2}$. This gives rise to the following useful relations:

$$E = m_T \cosh(y). \tag{B.5}$$

$$p = p_\mathrm{T} \cosh(y). \tag{B.6}$$

$$p_z = m_T \sinh(y). \tag{B.7}$$

C Glauber Model

The *Glauber model* of multiple collision processes provides a useful tool in quantitatively understanding the geometric configuration of a nucleus-nucleus collision. It considers the collisions at the baryon level, assuming that after a collision, the projectile nucleon can be still treated loosely as baryon-like object which make further collisions along the direction of incidence without deflection under the same baryon-baryon cross section (see Fig. C).

The total number of nucleons involved during a collision is defined to be the number of participants, N_{part}. Since each nucleon would normally suffer more than one collision, another useful variable, the number of binary collisions, N_{coll}, is also defined. The relationship between N_{part} and N_{coll} can be estimated in the context of the Glauber model (see Fig. C). In this model, each nucleus consisted of nucleons randomly arranged according to a "Woods-Saxon" probability distribution:

$$\rho(r) = \frac{\rho_0}{1+\exp\left(\frac{r-R}{d}\right)} \tag{C.1}$$

where $\rho(r)$ is the normalized nuclear density, R (6.5 fm for Au) is the nuclear radius, and d (0.54 fm for Au) is the surface thickness. The total inelastic p+p cross section measured from the data is used, which has 42 ± 1 mb at 200 GeV and 36 ± 1 mb at 62.4 GeV.

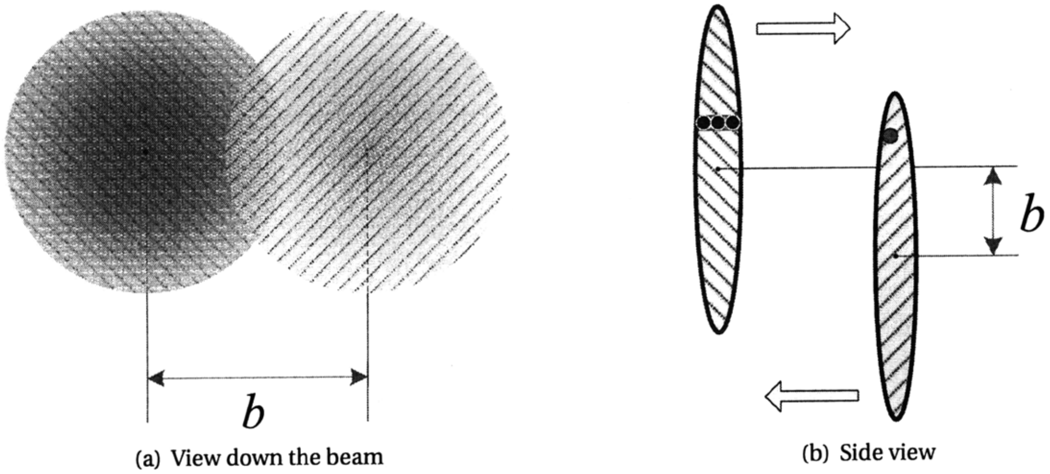

(a) View down the beam

(b) Side view

Figure C.1: Geometric illustration of an collision event with impact parameter b. (a) View along the beam and (b) from the side.

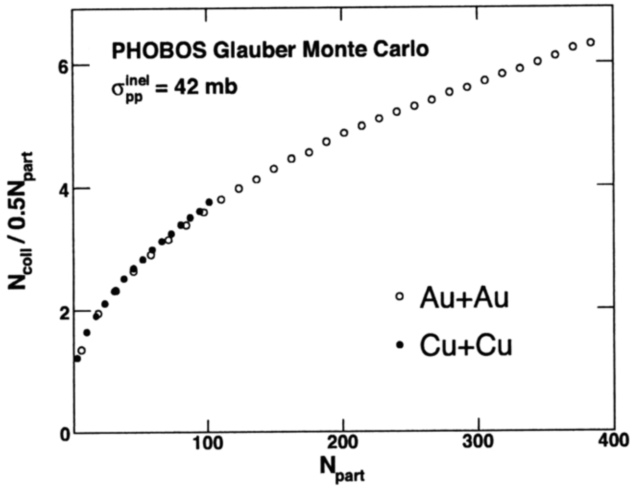

Figure C.2: The total number of binary collisions N_{coll} per participating nucleon pair for Cu+Cu and Au+Au from Glauber Model [90].

D Centrality Tables

Bin	Fraction	EOct Cuts	N_{part}	N_{coll}
17	0% to 3%	723.0 to 99999.0	108 ± 3.1	208 ± 14.9
16	3% to 6%	644.6 to 723.0	99.9 ± 2.9	186 ± 13.4
15	6% to 10%	558.7 to 644.6	91.1 ± 2.7	163 ± 11.8
14	10% to 15%	468.8 to 558.7	79 ± 2.6	132 ± 9.9
13	15% to 20%	392.2 to 468.8	67.5 ± 2.7	106 ± 8.6
12	20% to 25%	326.9 to 392.2	56.9 ± 2.9	83.1 ± 7.7
11	25% to 30%	270.1 to 326.9	47.4 ± 3.1	64.3 ± 7.0
10	30% to 35%	222.1 to 270.1	39.7 ± 3.2	50.4 ± 6.4
9	35% to 40%	181.3 to 222.1	32.7 ± 3.3	38.6 ± 5.7
8	40% to 45%	146.4 to 181.3	26.5 ± 3.2	29.2 ± 5.0
7	45% to 50%	116.8 to 146.4	21.3 ± 2.9	21.9 ± 4.2

Table D.1: Centrality selections used in Cu+Cu collisions at $\sqrt{s_{\text{NN}}} = 200$ GeV. The EOct cuts were `TrgCuts_PR05_200CuCu_BP_DCMEOct` and `TrgCuts_PR05_200CuCu_BM_DCMEOct`.

Bin	Fraction	PdlMean Cuts	N_{part}	N_{coll}
17	0% to 3%	1889.7 to 99999.0	359 ± 10.6	1105 ± 79.2
16	3% to 6%	1722.3 to 1889.7	330 ± 10.7	984 ± 73.0
15	6% to 10%	1519.0 to 1722.3	297 ± 9.8	847 ± 63.2
14	10% to 15%	1290.3 to 1519.0	256 ± 8.2	685 ± 50.5
13	15% to 20%	1085.3 to 1290.3	215 ± 6.8	537 ± 39.5
12	20% to 25%	902.8 to 1085.3	181 ± 6.3	421 ± 32.0
11	25% to 30%	743.4 to 902.8	149 ± 6.2	321 ± 26.4
10	30% to 35%	603.0 to 743.4	123 ± 6.3	245 ± 22.6
9	35% to 40%	483.4 to 603.0	101 ± 6.3	186 ± 19.5
8	40% to 45%	377.8 to 483.4	82.1 ± 6.2	138 ± 16.7
7	45% to 50%	288.5 to 377.8	64.9 ± 5.8	99.1 ± 13.7

Table D.2: Centrality selections used in Au+Au collisions at $\sqrt{s_{\text{NN}}} = 200$ GeV. The PdlMean cuts were `TrgCuts_PR04_200_BP` and `TrgCuts_PR04_200_BM`.

E HBT Effects on Two-particle Angular Correlations

The Bose-Einstein or HBT correlation will certainly contribute to the two-particle angular correlation function and thus might impact the estimation of cluster parameters [114]. It is known to cause a strong correlation between two identical particles having small relative invariant four-momentum $\mathbf{q}_{inv}^2$ (=$(\mathbf{q}_1 - \mathbf{q}_2)^2$). For identical bosons, the overall shape of the HBT effect can be approximated by a 1-D Gaussian correlation function:

$$C(\mathbf{q}_{inv}) = 1 + \lambda e^{-\mathbf{q}_{inv}^2 R_{inv}^2}. \tag{E.1}$$

To estimate the effect of the HBT correlation, in PYTHIA, which does not include this effect, the $\mathbf{q}_{inv}$ for each pair is calculated in $\rho_n^{\text{II}}(\Delta\eta, \Delta\phi)$ (ignoring the particle species), and the pair is weighted by C($\mathbf{q}_{inv}$) to artificially introduce the HBT correlation. In this study, $\lambda = 0.8$ and $R_{inv} = 1.0$ fm are used. Considering the fact that most of the pairs measured in this analysis are not identical-particle pairs, which should reduce the magnitude of λ, this choice of parameters exaggerates the expected effect of the HBT correlation. Thus, it gives a conservative estimate of its potential effect on the data.

In Fig. E.1(a), the difference between the correlation function with and without C($\mathbf{q}_{inv}$) weighting is shown as a function of $\Delta\eta$ and $\Delta\phi$ for PYTHIA. Finally, Fig. E.1(b) shows a comparison of pseudorapidity correlation functions with and without HBT weighting, with extracted cluster sizes of 1.76 and 1.72 respectively. From these studies, it appears that the HBT effect does enhance the short-range correlations with a range of around one unit in $\Delta\eta$ and 45° in $\Delta\phi$. However, after averaging over $\Delta\phi$, it only slightly influences the rapidity correlation function, resulting in an increase in cluster size of at most 2%. Even in the region $0° < \Delta\phi < 45°$, the increase is less than 3.5%.

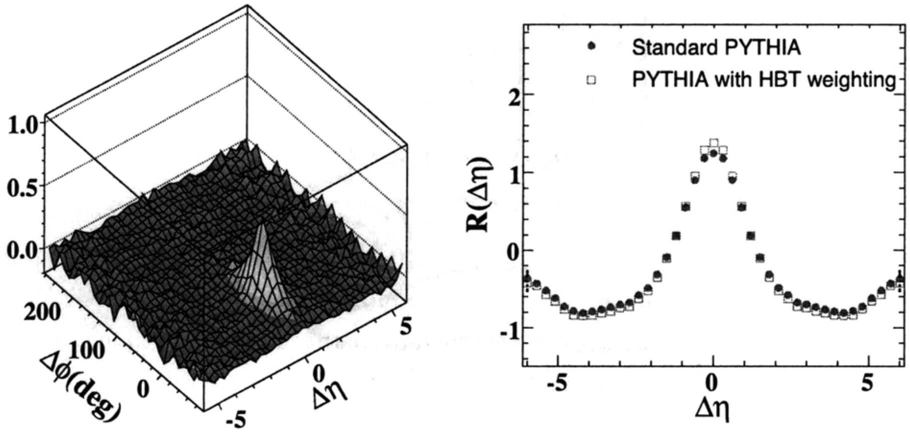

(a) (b)

Figure E.1: (a) Difference of the correlation function with HBT weighting minus the one without HBT weighting in $\Delta\eta$ and $\Delta\phi$ for PYTHIA at $\sqrt{s} = 200$ GeV. (b) Comparison of the pseudorapidity correlation function with (open circles) and without (solid circles) HBT weighting for PYTHIA at $\sqrt{s} = 200$ GeV [112].

F List of Acronyms

Facilities:

AGS	Alternating Gradient Synchrotron (http://www.bnl.gov/bnlweb/facilities/AGS.asp)
BNL	Brookhaven National Laboratory (http://www.bnl.gov/)
CERN	European Organization for Nuclear Research – *Conseil Européen pour la Recherche Nucléaire* (http://public.web.cern.ch/public/)
FAIR	Facility for Antiproton and Ion Research (http://www.gsi.de/fair/index_e.html)
ISR	Intersecting Storage Rings
LHC	Large Hadron Collider (http://lhc.web.cern.ch/lhc/)
RHIC	Relativistic Heavy Ion Collider (http://www.bnl.gov/RHIC/)
SLAC	Stanford Linear Accelerator Center (http://www.slac.stanford.edu/)
SPS	Super Proton Synchrotron (http://ab-dep-op-sps.web.cern.ch/ab-dep-op-sps/)

Physics Terminology:

AMPT	A Multiphase Transport Model
DIS	Deep-Inelastic Scattering
HBT	Hanbury-Brown and Twiss Effect
HIJING	Heavy Ion Jet Interaction Generator (http://www-nsdth.lbl.gov/ xnwang/hijing/)
ICM	Independent Cluster Model
KNO	Koba-Nielsen-Olesen
NLO	Next-to-leading Order

NNLO	Next-to-next-to-leading Order
QCD	Quantum Chromodynamics
QED	Quantum Electrodynamics
QGP	Quark Gluon Plasma

PHOBOS and RHIC Hardware:

ADC	Analog-to-Digital Converter
AnT	Analysis Trees
DAC	Digital-to-Analog Converter
DAQ	Data Acquisition
DMU	Data Multiplexing Unit
FEC	Front-End Controller
FPDP	Front Panel Data Port
HPSS	High Performance Storage System (http://www.hpss-collaboration.org/hpss/index.jsp)
I/O	Input/Output
ONO	Oxide-Nitrous-Oxide
PCAL	Proton Calorimeter
PhAT	PHOBOS Analysis Toolkit
PMC	PHOBOS Monte Carlo
PMT	Photomultiplier Tube
RCF	RHIC Computing Facility
SpecTrig	Spectrometer Trigger
TAC	Time-to-Analog Converter
TAM	Tree-Analysis Modules
TDC	Time-to-Digital Converter

TOF	Time-of-Flight
T0	Time-Zero Counter
VME	VERSAmodule Eurocard
ZDC	Zero-Degree Calorimeter

Experimental Terminology:

CMN	Common-Mode Noise
DCA	Distance of Closest Approach
IsCol	Is Collision
MC	Monte Carlo
MinBias	Minimum Bias
MIP	Minimum Ionizing Particle
NSD	Non-Sigle-Diffractive
OctProbMult	Octagon Probability Multiplicity
PdlMean	Paddle Mean
PdlTDiff	Paddle Time Difference
PID	Particle Identification
RMSSel	RMS-Selected

Bibliography

[1] C. Amsler et al. Review of particle physics. *Phys. Lett.*, B667:1, 2008. doi: 10.1016/j.physletb.2008.07.018.

[2] W. M. Yao *et al.* Review of particle physics. *J. Phys.*, G33:1–1232, 2006.

[3] K. Hagiwara et al. Review of Particle Physics. *Physical Review D*, 66:010001+, 2002. URL `http://pdg.lbl.gov`.

[4] D. H. Perkins. *Introduction to High Energy Physics.* Addison-Wesley Pub. Co., Reading, Massachusetts, USA, 1987. ISBN 0-201-12105-0.

[5] Murray Gell-Mann. A Schematic Model of Baryons and Mesons. *Phys. Lett.*, 8: 214–215, 1964. doi: 10.1016/S0031-9163(64)92001-3.

[6] G. Zweig. An SU(3) model for strong interaction symmetry and its breaking. 2. CERN-TH-412, 1964.

[7] M. Gell-Mann. The eightfold way: A theory of strong interaction symmetry. California Institute of Technology Synchrotron Laboratory Report CTSL-20, 1961.

[8] Y. Ne'eman. Derivations of strong interactions from a gauge invariance. *Nucl. Phys.*, 26:222–229, 1961.

[9] V. E. Barnes et al. Observation of a hyperon with strangeness -3. *Phys. Rev. Lett.*, 12:204–206, 1964. doi: 10.1103/PhysRevLett.12.204.

[10] Jerome I. Friedman and Henry W. Kendall. Deep inelastic electron scattering. *Ann. Rev. Nucl. Part. Sci.*, 22:203–254, 1972. doi: 10.1146/annurev.ns.22.120172.001223.

[11] J. D. Bjorken. Asymptotic Sum Rules at Infinite Momentum. *Phys. Rev.*, 179:1547–1553, 1969. doi: 10.1103/PhysRev.179.1547.

[12] S. L. Glashow, J. Iliopoulos, and L. Maiani. Weak Interactions with Lepton-Hadron Symmetry. *Phys. Rev.*, D2:1285–1292, 1970. doi: 10.1103/PhysRevD.2.1285.

[13] J. J. Aubert et al. Experimental Observation of a Heavy Particle J. *Phys. Rev. Lett.*, 33:1404–1406, 1974. doi: 10.1103/PhysRevLett.33.1404.

[14] J. E. Augustin et al. Discovery of a Narrow Resonance in e+ e- Annihilation. *Phys. Rev. Lett.*, 33:1406–1408, 1974. doi: 10.1103/PhysRevLett.33.1406.

[15] S. W. Herb et al. Observation of a dimuon resonance at 9.5-GeV in 400-GeV proton - nucleus collisions. *Phys. Rev. Lett.*, 39:252–255, 1977. doi: 10.1103/PhysRevLett.39.252.

[16] F. Abe et al. Observation of top quark production in $\bar{p}p$ collisions. *Phys. Rev. Lett.*, 74:2626–2631, 1995. doi: 10.1103/PhysRevLett.74.2626.

[17] S. Abachi et al. Search for high mass top quark production in $p\bar{p}$ collisions at $\sqrt{s} =$ 1.8 TeV. *Phys. Rev. Lett.*, 74:2422–2426, 1995. doi: 10.1103/PhysRevLett.74.2422.

[18] Francis Halzen and Alan Douglas Martin. *Quarks and leptons: an introductory course in modern particle physics.* Wiley, New York, NY, 1984.

[19] Particle Data Group. Plots of cross sections and related quantities, 2007. URL `http://pdg.lbl.gov/2007/hadronic-xsections/hadronicrpp_page6.pdf`. Fig. 6.

[20] C. Reed. *Studies of Nucleon-Gold Collisions at 200 GeV per Nucleon Pair Using Tagged d+Au Interactions.* PhD thesis, Massachusetts Institute of Technology, 2006.

[21] R. Brandelik et al. Evidence for Planar Events in e+ e- Annihilation at High- Energies. *Phys. Lett.*, B86:243, 1979. doi: 10.1016/0370-2693(79)90830-X.

[22] Herbert Goldstein, Charles P. Poole, and John Safko. *Classical Mechanics.* Addison Wesley, 2002. ISBN 0-201-65702-3.

[23] M. E. Peskin and D. V. Schroeder. *An Introduction to Quantum Field Theory.* Addison-Wesley Pub. Co., Reading, Massachusetts, USA, 1995. ISBN 0-201-50397-2.

[24] Siegfried Bethke. Experimental tests of asymptotic freedom. *Prog. Part. Nucl. Phys.*, 58:351–386, 2007. doi: 10.1016/j.ppnp.2006.06.001. Shown in Fig. 17. [arXiv:hep-ex/0606035].

[25] Frank Wilczek. Asymptotic freedom: From paradox to paradigm. *Proc. Nat. Acad. Sci.*, 102:8403–8413, 2005. doi: 10.1103/RevModPhys.77.857.

[26] N. K. Nielsen. Asymptotic freedom as a spin effect. *Am. J. Phys.*, 49:1171, 1981. doi: 10.1119/1.12565.

[27] G. Schierholz and M. Teper. Baryon production in QCD jets. *Zeit. Phys.*, C13:53, 1982.

[28] D. J. Gross and Frank Wilczek. Ultraviolet behavior of non-Abelian gauge theories. *Phys. Rev. Lett.*, 30:1343–1346, 1973. doi: 10.1103/PhysRevLett.30.1343.

[29] H. David Politzer. Reliable perturbative results for strong interactions? *Phys. Rev. Lett.*, 30:1346–1349, 1973. doi: 10.1103/PhysRevLett.30.1346.

[30] W. J. Stirling R. K. Ellis and B. R. Webber. *QCD and Collider Physics.* Cambridge University Press, Cambridge, UK, 2003. ISBN 0-521-54589-7.

[31] Bo Andersson, G. Gustafson, G. Ingelman, and T. Sjostrand. Parton Fragmentation and String Dynamics. *Phys. Rept.*, 97:31–145, 1983. doi: 10.1016/0370-1573(83)90080-7.

[32] R. D. Field and R. P. Feynman. Quark Elastic Scattering as a Source of High Transverse Momentum Mesons. *Phys. Rev.*, D15:2590–2616, 1977. doi: 10.1103/PhysRevD.15.2590.

[33] X. Artru and G. Mennessier. String model and multiproduction. *Nucl. Phys.*, B70: 93–115, 1974. doi: 10.1016/0550-3213(74)90360-5.

[34] M. G. Bowler. e+ e- Production of Heavy Quarks in the String Model. *Zeit. Phys.*, C11:169, 1981. doi: 10.1007/BF01574001.

[35] Bo Andersson, G. Gustafson, and B. Soderberg. A General Model for Jet Fragmentation. *Z. Phys.*, C20:317, 1983. doi: 10.1007/BF01407824.

[36] Bo Andersson, G. Gustafson, and B. Soderberg. A PROBABILITY MEASURE ON PARTON AND STRING STATES. *Nucl. Phys.*, B264:29, 1986. doi: 10.1016/0550-3213(86)90471-2.

[37] Richard D. Field and Stephen Wolfram. A QCD Model for e+ e- Annihilation. *Nucl. Phys.*, B213:65, 1983. doi: 10.1016/0550-3213(83)90175-X.

[38] B. R. Webber. A QCD Model for Jet Fragmentation Including Soft Gluon Interference. *Nucl. Phys.*, B238:492, 1984. doi: 10.1016/0550-3213(84)90333-X.

[39] I. M. Dremin and C. Quigg. Clusters in hadron multiple production processes. *Soviet Physics Uspekhi*, 21(3):265–271, 1978. doi: 10.1070/PU1978v021n03ABEH005534. URL `http://stacks.iop.org/0038-5670/21/265`.

[40] Kenneth G. Wilson. Confinement of quarks. *Phys. Rev.*, D10:2445–2459, 1974. doi: 10.1103/PhysRevD.10.2445.

[41] Rajan Gupta. Introduction to lattice QCD. 1997. [arXiv:hep-lat/9807028].

[42] T. Hatsuda K. Yagi and Y. Miake. *Quark-Gluon Plasma.* Cambridge University Press, Cambridge, UK, 2005. ISBN 0-521-56108-2.

[43] S Chakrabarty. On the possibility of nuclear liquid-gas phase transition. *Journal of Physics G: Nuclear and Particle Physics*, 20(3):469–475, 1994. URL `http://stacks.iop.org/0954-3899/20/469`.

[44] Mark G. Alford, Krishna Rajagopal, and Frank Wilczek. QCD at finite baryon density: Nucleon droplets and color superconductivity. *Phys. Lett.*, B422:247–256, 1998. doi: 10.1016/S0370-2693(98)00051-3.

[45] R. Rapp, Thomas Schafer, Edward V. Shuryak, and M. Velkovsky. Diquark Bose condensates in high density matter and instantons. *Phys. Rev. Lett.*, 81:53–56, 1998. doi: 10.1103/PhysRevLett.81.53.

[46] John Bardeen, L. N. Cooper, and J. R. Schrieffer. Theory of superconductivity. *Phys. Rev.*, 108:1175–1204, 1957. doi: 10.1103/PhysRev.108.1175.

[47] Philip W. Anderson. PLASMONS, GAUGE INVARIANCE, AND MASS. *Phys. Rev.*, 130:439–442, 1963. doi: 10.1103/PhysRev.130.439.

[48] Peter W. Higgs. BROKEN SYMMETRIES AND THE MASSES OF GAUGE BOSONS. *Phys. Rev. Lett.*, 13:508–509, 1964. doi: 10.1103/PhysRevLett.13.508.

[49] Mark G. Alford, Krishna Rajagopal, and Frank Wilczek. Color-flavor locking and chiral symmetry breaking in high density QCD. *Nucl. Phys.*, B537:443–458, 1999. doi: 10.1016/S0550-3213(98)00668-3.

[50] Mark G. Alford, Andreas Schmitt, Krishna Rajagopal, and Thomas Schafer. Color superconductivity in dense quark matter. 2007. [arXiv:0709.4635].

[51] Dany Page and Sanjay Reddy. Dense Matter in Compact Stars: Theoretical Developments and Observational Constraints. *Ann. Rev. Nucl. Part. Sci.*, 56:327–374, 2006. doi: 10.1146/annurev.nucl.56.080805.140600. [arXiv:astro-ph/0608360].

[52] J. C. Collins and M. J. Perry. Superdense matter: Neutrons or asymptotically free quarks? *Phys. Rev. Lett.*, 34(21):1353–1356, May 1975. doi: 10.1103/PhysRevLett.34.1353.

[53] Edward Shuryak. Quantum chromodynamics and the theory of superdense matter. *Physics Reports*, 61(2):71–158, 1980.

[54] Frithjof Karsch. Lattice results on QCD thermodynamics. *Nucl.Phys.*, A698:199–208, 2002.

[55] K. Splittorff. The sign problem in the epsilon-regime of QCD. *PoS*, LAT2006:023, 2006. [arXiv:hep-lat/0610072].

[56] Philippe de Forcrand and Owe Philipsen. The chiral critical line of N(f) = 2+1 QCD at zero and non-zero baryon density. *JHEP*, 01:077, 2007. [arXiv:hep-lat/0607017].

[57] Christof Roland. Particle ratio fluctuations in NA49. *PoS*, CFRNC2006:012, 2006.

[58] T. D. Lee. Abnormal Nuclear States and Vacuum Excitations. *Rev. Mod. Phys.*, 47: 267, 1975. doi: 10.1103/RevModPhys.47.267.

[59] B. B. Back et al. The PHOBOS perspective on discoveries at RHIC. *Nucl. Phys.*, A757:28–101, 2005. doi: 10.1016/j.nuclphysa.2005.03.084. [arXiv:nucl-ex/0410022].

[60] John Adams et al. Experimental and theoretical challenges in the search for the quark gluon plasma: The STAR collaboration's critical assessment of the evidence from RHIC collisions. *Nucl. Phys.*, A757:102–183, 2005. doi: 10.1016/j.nuclphysa.2005.03.085. [arXiv:nucl-ex/0501009].

[61] K. Adcox et al. Formation of dense partonic matter in relativistic nucleus nucleus collisions at RHIC: Experimental evaluation by the PHENIX collaboration. *Nucl. Phys.*, A757:184–283, 2005. doi: 10.1016/j.nuclphysa.2005.03.086. [arXiv:nucl-ex/0410003].

[62] I. Arsene et al. Quark gluon plasma and color glass condensate at RHIC? The perspective from the BRAHMS experiment. *Nucl. Phys.*, A757:1–27, 2005. doi: 10.1016/j.nuclphysa.2005.02.130. [arXiv:nucl-ex/0410020].

[63] (ed.) Alam, J., (ed.) Chattopadhyay, S., (ed.) Nayak, T., (ed.) Sinha, B., and (ed.) Bristol, Y. Ultra-relativistic nucleus-nucleus collisions. Proceedings, 20th International Conference, Quark Matter 2008, Japur, India, February 4-10, 2008. Prepared for 20th International Conference on Ultra- Relativistic Nucleus-Nucleus Collisions: Quark Matter 2008 (QM2008), Japur, India, 4-10 Feb 2008.

[64] (ed.) Ma, Yu-Gang et al. Ultra-relativistic nucleus-nucleus collisions. Proceedings, 19th International Conference, Quark Matter 2006, Shanghai, P.R. China, November 14-20, 2006. Prepared for 19th International Conference on Ultra-Relativistic Nucleus-Nucleus Collisions: Quark Matter 2006 (QM2006), Shanghai, China, 14-20 Nov 2006.

[65] (ed.) Csörgő, T., (ed.) Lévai, P., (ed.) David, G., and (ed.) Papp, G. Quark matter. Proceedings, 18th International Conference on Ultra-Relativistic Nucleus-Nucleus Collisions, QM'05, Budapest, Hungary, August 4-9, 2005. Prepared for 18th International Conference on Ultrarelativistic Nucleus-Nucleus Collisions: Quark Matter 2005 (QM 2005), Budapest, Hungary, 4-9 Aug 2005.

[66] (ed.) Ritter, H. G. and (ed.) Wang, X. N. Ultra-relativistic nucleus-nucleus collisions. Proceedings, 17th International Conference, Quark Matter 2004, Oakland, USA, January 11-17, 2004. Prepared for 17th International Conference on Ultra Relativistic Nucleus-Nucleus Collisions (Quark Matter 2004), Oakland, California, 11-17 Jan 2004.

[67] J. D. Bjorken. Highly Relativistic Nucleus-Nucleus Collisions: The Central Rapidity Region. *Phys. Rev.*, D27:140–151, 1983. doi: 10.1103/PhysRevD.27.140.

[68] B. B. Back et al. Centrality dependence of the charged particle multiplicity near mid-rapidity in Au + Au collisions at s(NN)**(1/2) = 130-GeV and

200-GeV. *Phys. Rev.*, C65:061901, 2002. doi: 10.1103/PhysRevC.65.061901. [arXiv:nucl-ex/0201005].

[69] P. Huovinen, P. F. Kolb, Ulrich W. Heinz, P. V. Ruuskanen, and S. A. Voloshin. Radial and elliptic flow at RHIC: Further predictions. *Phys. Lett.*, B503:58–64, 2001. doi: 10.1016/S0370-2693(01)00219-2. [arXiv:hep-ph/0101136].

[70] Stephen Scott Adler et al. Identified charged particle spectra and yields in Au + Au collisions at s(NN)**(1/2) = 200-GeV. *Phys. Rev.*, C69:034909, 2004. doi: 10.1103/PhysRevC.69.034909.

[71] B. B. Back et al. Centrality dependence of charged hadron transverse momentum spectra in d + Au collisions at s(NN)**(1/2) = 200-GeV. *Phys. Rev. Lett.*, 91:072302, 2003. doi: 10.1103/PhysRevLett.91.072302. [arXiv:nucl-ex/0306025].

[72] B. B. Back et al. Charged hadron transverse momentum distributions in Au + Au collisions at s(NN)**(1/2) = 200-GeV. *Phys. Lett.*, B578:297–303, 2004. doi: 10.1016/j.physletb.2003.10.101. [arXiv:nucl-ex/0302015].

[73] C. Adler et al. Disappearance of back-to-back high p(T) hadron correlations in central Au + Au collisions at s(NN)**(1/2) = 200-GeV. *Phys. Rev. Lett.*, 90:082302, 2003. doi: 10.1103/PhysRevLett.90.082302. [arXiv:nucl-ex/0210033].

[74] B. Alver et al. Importance of Correlations and Fluctuations on the Initial Source Eccentricity in High-Energy Nucleus-Nucleus Collisions. *Phys. Rev.*, C77:014906, 2008. doi: 10.1103/PhysRevC.77.014906. [arXiv:0711.3724].

[75] P. F. Kolb, P. Huovinen, Ulrich W. Heinz, and H. Heiselberg. Elliptic flow at SPS and RHIC: From kinetic transport to hydrodynamics. *Phys. Lett.*, B500:232–240, 2001. doi: 10.1016/S0370-2693(01)00079-X. [arXiv:hep-ph/0012137].

[76] Jean-Yves Ollitrault. Anisotropy as a signature of transverse collective flow. *Phys. Rev.*, D46:229–245, 1992. doi: 10.1103/PhysRevD.46.229.

[77] Jean-Yves Ollitrault. Determination of the reaction plane in ultrarelativistic nuclear collisions. *Phys. Rev.*, D48:1132–1139, 1993. doi: 10.1103/PhysRevD.48.1132.

[78] B. B. Back et al. Centrality and pseudorapidity dependence of elliptic flow for charged hadrons in Au + Au collisions at s(NN)**(1/2) = 200-GeV. *Phys. Rev.*, C72: 051901, 2005. doi: 10.1103/PhysRevC.72.051901. [arXiv:nucl-ex/0407012].

[79] Derek Teaney. Effect of shear viscosity on spectra, elliptic flow, and Hanbury Brown-Twiss radii. *Phys. Rev.*, C68:034913, 2003. doi: 10.1103/PhysRevC.68.034913.

[80] John Adams et al. Multi-strange baryon elliptic flow in Au + Au collisions at s(NN)**(1/2) = 200-GeV. *Phys. Rev. Lett.*, 95:122301, 2005. doi: 10.1103/PhysRevLett.95.122301. [arXiv:nucl-ex/0504022].

[81] M. Harrison, T. Ludlam, and S. Ozaki. RHIC project overview. *Nucl. Instrum. Meth.*, A499:235–244, 2003. doi: 10.1016/S0168-9002(02)01937-X.

[82] M. Harrison, Stephen G. Peggs, and T. Roser. The RHIC accelerator. *Ann. Rev. Nucl. Part. Sci.*, 52:425–469, 2002. doi: 10.1146/annurev.nucl.52.050102.090650.

[83] K. H. Ackermann et al. STAR detector overview. *Nucl. Instrum. Meth.*, A499:624–632, 2003. doi: 10.1016/S0168-9002(02)01960-5.

[84] K. Adcox et al. PHENIX detector overview. *Nucl. Instrum. Meth.*, A499:469–479, 2003. doi: 10.1016/S0168-9002(02)01950-2.

[85] M. Adamczyk et al. The BRAHMS experiment at RHIC. *Nucl. Instrum. Meth.*, A499:437–468, 2003. doi: 10.1016/S0168-9002(02)01949-6.

[86] B. B. Back et al. The PHOBOS detector at RHIC. *Nucl. Instrum. Meth.*, A499:603–623, 2003. doi: 10.1016/S0168-9002(02)01959-9.

[87] K. Gulbrandsen. *Relative Yields of Antiparticles to Particles in Au+Au Collisions at 130 and 200 GeV per Nucleon Pair.* PhD thesis, Massachusetts Institute of Technology, 2004.

[88] A. Bickley. *Charged Antiparticle to Particle Ratios Near Midrapidity in d+Au and p+p Collisions at sqrt(sNN) = 200 GeV.* PhD thesis, University of Maryland, 2004. UMI-31-52308.

[89] C. Henderson. *Identified Particle Transverse Momentum Distributions from Au+Au Collisions at 62.4 GeV per Nucleon Pair.* PhD thesis, Massachusetts Institute of Technology, 2005.

[90] E. Wenger. *Studies of High Transverse Momentum Phenomena in Heavy Ion Collisions Using the PHOBOS Detector.* PhD thesis, Massachusetts Institute of Technology, 2008.

[91] Clemens Adler et al. The RHIC zero degree calorimeters. *Nucl. Instrum. Meth.*, A470:488–499, 2001. doi: 10.1016/S0168-9002(01)00627-1. [arXiv:nucl-ex/0008005].

[92] C. A. Pruneau. The E864 lead/scintillating fiber hadronic calorimeter. Prepared for 6th International Conference on Calorimetry in High-energy Physics (ICCHEP 96), Rome, Italy, 8-14 Jun 1996.

[93] R. Bindel, E. García, A. C. Mignerey, and L. P. Remsberg. Array of scintillator counters for PHOBOS at RHIC. *Nucl. Instrum. Meth.*, A474:38–45, 2001. doi: 10.1016/S0168-9002(01)00866-X.

[94] A. Sukhanov, P. Kulinich, and P. Sarin. A gigabit/s data acquisition system. *rtc*, 0: 123, 2005. doi: http://doi.ieeecomputersociety.org/10.1109/RTC.2005.1547512.

[95] B.G. Gibbard and T.G. Throwe. The RHIC computing facility. *Nucl. Instr. Meth.*, A499:814–818, 2003.

[96] R. Brun and F. Rademakers. ROOT. *Nucl. Instr. Meth.*, A389:81, 1997.

[97] Rene Brun et al. GEANT version 3.21. Detector description and simulation tool. The GEANT webpage is http://wwwasd.web.cern.ch/wwwasd/geant/.

[98] W. R. Leo. *Techniques for Nuclear and Particle Physics Experiments: A How-To Approach*, chapter 10: Semiconductor Detectors. Springer-Verlag, second edition, 1994. ISBN 0-387-57280-5.

[99] R. Nouicer et al. Silicon pad detectors for the PHOBOS experiment at RHIC. *Nucl. Instrum. Meth.*, A461:143–149, 2001. doi: 10.1016/S0168-9002(00)01191-8. [arXiv:nucl-ex/0208006].

[100] M. Plesko, J. Fitch, D. Ross, C. Gomes, P. Kulinich, H. Pernegger, P. Sarin, and B. Wadsowrth. Front-end electronics for the silicon partition of the phobos detector at rhic. *Nuclear Science Symposium Conference Record, 2001 IEEE*, 1:76–80 vol.1, Nov. 2001. ISSN 1082-3654.

[101] R. Hollis. *Centrality Evolution of Charged Particles Produced in Ultra-relativistic Au+Au and d+Au Collisions.* PhD thesis, University of Illinois at Chicago, 2005.

[102] W. Fischer et al. Electron cloud observations and cures in the Relativistic Heavy Ion Collider. *Phys. Rev. ST Accel. Beams*, 11:041002, 2008. doi: 10.1103/PhysRevSTAB.11.041002.

[103] P. Decowski. *Energy and Centrality Dependence of Mid-Rapidity Charged Particle Multiplicity in Relativistic Heavy-Ion Collisions.* PhD thesis, Massachusetts Institute of Technology, 2002.

[104] Michael L. Miller, Klaus Reygers, Stephen J. Sanders, and Peter Steinberg. Glauber modeling in high energy nuclear collisions. *Ann. Rev. Nucl. Part. Sci.*, 57:205–243, 2007. doi: 10.1146/annurev.nucl.57.090506.123020.

[105] P. Sarin. *Measurement of Charged Particle Multiplicity Distributions in Au+Au Collisions up to 200 GeV.* PhD thesis, Massachusetts Institute of Technology, 2003.

[106] B. B. Back et al. Forward-backward multiplicity correlations in s(NN)**(1/2) = 200-GeV Au + Au collisions. *Phys. Rev.*, C74:011901, 2006. doi: 10.1103/PhysRevC.74.011901.

[107] J. Hamblen. *Pseudorapidity Dependence of Directed and Elliptic Flow in Au+Au Collisions at 19.6, 62.4, 130, and 200 GeV per Nucleon Pair.* PhD thesis, University of Rochester, 2006.

[108] B. Alver et al. High pT Triggered Delta-eta,Delta-phi Correlations over a Broad Range in Delta-eta. *J. Phys.*, G35:104080, 2008. doi: 10.1088/0954-3899/35/10/104080.

[109] K. Eggert et al. Angular Correlations Between the Charged Particles Produced in p p Collisions at ISR Energies. *Nucl. Phys.*, B86:201, 1975. doi: 10.1016/0550-3213(75)90440-X.

[110] B. Alver et al. Two-particle angular correlations in p + p and Cu + Cu collisions at PHOBOS. *J. Phys.*, G34:S1005–1010, 2007. doi: 10.1088/0954-3899/34/8/S144.

[111] B. Alver et al. System size dependence of two-particle angular correlations in p+p, Cu+Cu and Au+Au collisions. *J. Phys.*, G35:104142, 2008. doi: 10.1088/0954-3899/35/10/104142.

[112] B. Alver et al. Cluster properties from two-particle angular correlations in p + p collisions at s**(1/2) = 200-GeV and 410-GeV. *Phys. Rev.*, C75:054913, 2007. doi: 10.1103/PhysRevC.75.054913.

[113] B. Alver and for the PHOBOS Collaboration. System size dependence of cluster properties from two- particle angular correlations in Cu+Cu and Au+Au collisions at $\sqrt{s_{NN}} = 200$ GeV. 2008.

[114] C. Albajar et al. BOSE-EINSTEIN CORRELATIONS IN anti-p p INTERACTIONS AT S**(1/2) = 0.2-TeV TO 0.9-TeV. *Phys. Lett.*, B226:410, 1989. doi: 10.1016/0370-2693(89)91221-5.

[115] Nicolas Borghini, Phuong Mai Dinh, and Jean-Yves Ollitrault. A new method for measuring azimuthal distributions in nucleus nucleus collisions. *Phys. Rev.*, C63: 054906, 2001. doi: 10.1103/PhysRevC.63.054906.

[116] Michael Daugherity. Anomalous centrality variation of minijet angular correlations in Au-Au collisions at 62 and 200 GeV from STAR. *J. Phys.*, G35:104090, 2008. doi: 10.1088/0954-3899/35/10/104090.

[117] B. Alver et al. Non-flow correlations and elliptic flow fluctuations in Au+Au collisions at s(NN)**(1/2)=200GeV. *J. Phys.*, G35:104101, 2008. doi: 10.1088/0954-3899/35/10/104101.

[118] R. E. Ansorge et al. CHARGED PARTICLE CORRELATIONS IN ANTI-P P COLLISIONS AT C.M. ENERGIES OF 200-GEV, 546-GEV AND 900-GEV. *Z. Phys.*, C37: 191–213, 1988. doi: 10.1007/BF01579906.

[119] D. Drijard et al. DENSITY, CHARGE AND TRANSVERSE MOMENTUM CORRELATIONS OF PARTICLES IN NONDIFFRACTIVE PROTON PROTON COLLISIONS AT s**(1/2) = 52.5-GeV. *Nucl. Phys.*, B155:269, 1979. doi: 10.1016/0550-3213(79)90269-4.

[120] F. S. Henyey. Elastic scattering from the multiperipheral model. *Phys. Lett.*, B45: 469–474, 1973. doi: 10.1016/0370-2693(73)90646-1.

[121] Edmond L. Berger. Rapidity Correlations at Fixed Multiplicity in Cluster Emission Models. *Nucl. Phys.*, B85:61, 1975. doi: 10.1016/0550-3213(75)90557-X.

[122] A. Morel and G. Plaut. How Do Clusters Look in Semiinclusive Cross-Sections? *Nucl. Phys.*, B78:541, 1974. doi: 10.1016/0550-3213(74)90597-5.

[123] Li-jun Shi and Sangyong Jeon. Charge transfer fluctuations as a signal for QGP. *Phys. Rev.*, C72:034904, 2005. doi: 10.1103/PhysRevC.72.034904.

[124] B. B. Back et al. The significance of the fragmentation region in ultrarelativistic heavy ion collisions. *Phys. Rev. Lett.*, 91:052303, 2003. doi: 10.1103/PhysRevLett.91.052303.

[125] B. Alver et al. System Size, Energy and Centrality Dependence of Pseudorapidity Distributions of Charged Particles in Relativistic Heavy Ion Collisions. 2007.

[126] Z. Koba, Holger Bech Nielsen, and P. Olesen. Scaling of multiplicity distributions in high-energy hadron collisions. *Nucl. Phys.*, B40:317–334, 1972. doi: 10.1016/0550-3213(72)90551-2.

[127] Zi-Wei Lin, Che Ming Ko, Bao-An Li, Bin Zhang, and Subrata Pal. A multi-phase transport model for relativistic heavy ion collisions. *Phys. Rev.*, C72:064901, 2005. doi: 10.1103/PhysRevC.72.064901.

[128] Adam Kisiel, Tomasz Taluc, Wojciech Broniowski, and Wojciech Florkowski. THERMINATOR: Thermal heavy-ion generator. *Comput. Phys. Commun.*, 174:669–687, 2006. doi: 10.1016/j.cpc.2005.11.010.

[129] John Adams et al. Event-by-event fluctuations in Au Au collisions at s(NN)**(1/2) = 130-GeV. *Phys. Rev.*, C71:064906, 2005. doi: 10.1103/PhysRevC.71.064906.

[130] John Adams et al. Incident energy dependence of p(t) correlations at RHIC. *Phys. Rev.*, C72:044902, 2005. doi: 10.1103/PhysRevC.72.044902.

[131] K. Adcox et al. Event-by-event fluctuations in mean p(T) and mean e(T) in s(NN)**(1/2) = 130-GeV Au + Au collisions. *Phys. Rev.*, C66:024901, 2002. doi: 10.1103/PhysRevC.66.024901.

[132] Stephen Scott Adler et al. Measurement of non-random event-by-event fluctuations of average transverse momentum in s**(1/2) = 200-GeV Au + Au and p + p collisions. *Phys. Rev. Lett.*, 93:092301, 2004. doi: 10.1103/PhysRevLett.93.092301.

[133] Wojciech Broniowski, Piotr Bozek, Wojciech Florkowski, and Brigitte Hiller. p(T)-fluctuations and multiparticle clusters in heavy-ion collisions. *PoS*, CFRNC2006:020, 2006.

[134] Torbjorn Sjostrand. High-energy physics event generation with PYTHIA 5.7 and JETSET 7.4. *Comput. Phys. Commun.*, 82:74–90, 1994. doi: 10.1016/0010-4655(94)90132-5.

List of Figures

List of Tables

Acknowledgments

This thesis would not have been possible without generous assistances and supports of many people.

First and foremost, I would like to express my deep and sincere gratitude to my advisor, Professor Gunther Roland, who directed me through the entire journey of my graduate studies. Gunther provided me the enthusiasm and inspiration to physics that I always needed. Not only did he teach me the knowledge of heavy ion physics but most importantly establish my ability of conducting independent research work — solving the puzzles and exploring the unknowns. He is an indispensable figure in the success of my thesis, MIT heavy ion group and the PHOBOS experiment.

I am honored to have two great physicists, Professor Wit Busza and Professor John Negele, as the other members of my PhD thesis committee. As the leader of MIT heavy ion group and the PHOBOS collaboration, Wit always encouraged us to at least take a couple of hours every week to think about the physics meanings of the work we are doing. I have been enjoying the discussions with him, and amazed at his ability of tackling very complicated problems using simple basic rules and languages. As a Chinese student, I would particularly like to thank Wit for the improvement of my oral English by reminding me all the time to speak louder, slowly and clearly in front of people. As a nuclear theorist, professor John Negele provided me invaluable theoretical inputs and implications of my work.

It is my pleasure to have the opportunity of being educated at MIT and working with talented people in the heavy ion group. Bolek Wyslouch always played an important leadership and brought the group toward the future experiment at LHC. Christof Roland, Maarten Ballintijn, Gábor Veres, Constantin Loizides are the guys with tremendous expertise and have always been ready to help others out. My senior fellow students, Kris Gulbrandsen, Jay Kane, Conor Henderson, Corey Reed, taught me most of the experimental skills as well as heavy ion physics that I have been armed with in facing all kinds of challenges in my studies these years. The humorous American culture they brought into the office made our daily life much less boring. My colleagues and friends, Burak Alver, Edward Wenger, Siarhei Vaurynovich, have been working closely with me since the very beginning. The discussions among us were always very fruitful and I was deeply impressed by their broad outreach of knowledge and creative ideas that inspired me all the time. The younger fellows, Yen-jie Lee, Frank Ma, Yetkin Yilmaz, Andre Yoon, Yongsun Kim, Young Soo Park, although most of them have already moved to CERN now, made our office a place full of fun. In the end, I would like to thank to Anna Maria Convertino, our secretary, for elegantly arranging all our administrative affairs. It is hard to imagine how we could survive without you.

I had the great privilege of working in the PHOBOS collaboration, a small but strong group of brilliant nuclear physicists. Many thanks to Peter Steinberg, George Stephans and Aneta Iordanova for working with me closely as the correlation analysis committee over the last three years. The enormous time they spent on reviewing my analyses led to a number of high quality publications and talks at Quark Matter. I am going to miss the countless fights I had with Peter, although once frustrating but indeed helped my in many aspects, an experience that I might not be able to find again elsewhere. Andrzej Olszewski and Krzysztof Woźniak generously provided all the MC simulations as well as vital suggestions that I relied on in my analyses. Without the work of Andrei Sukhanov on data acquisition and Marguerite Tonjes on data production, it would be impossible to have any data to analyze. The efforts from UIC crews, Dave Hofman, Richard Hollis, Aneta Iordanova, on event selections and centrality cuts are absolutely essential to all the analyses of the collaboration. Finally, since I am a young guy to the PHOBOS collaboration, there were many important characters that I am not familiar with and couldn't recognize, especially the heroes who built the PHOBOS detector. To those who I have neglected to mention here, please accept my apologies. Thank you very much for all your endeavors and PHOBOS could not have succeeded without you.

I would like to thank Dr. Nu Xu for bringing me to the area of heavy ion physics. Although we never worked together, he has been supporting and encouraging me since we first met in the University of Science and Technology of China (USTC) many years ago. I am also indebted to my mentors, Professor Hongfang Chen and Professor Chen Li, during my undergraduate studies at USTC, who enlightened my interests in the research of high energy experimental physics.

My life in Boston would have been intolerable without so many great friends I met here, Feng Zhou, Jianhong Zhang, Changgang Lou, Jingxia Wen, Zao Xu, Jinbo Wang, Jingqiang Wei, Zebo Tang, who provided me enormous helps and made living here great fun. I will always remember the good times we had together.

Finally, I owe everything to my family. I would like to appreciate all the sacrifices made by my wife, Jie Meng. Although being apart thousands of miles away for more than four years, she has given me the most important supports and understandings (not to mention the beautiful pictures she made for me in this thesis) all along. My parents, Jian Li and Ruyan Sun, have been constantly providing me selfless love, support and guidance that could not be expected more by any other child. None of this would have been possible without them.